



***Magneto-thermopower and  
Magnetoresistance of  
Co-Ni Alloy and Co-Ni/Cu  
Multilayered Nanowires.***

---

**Dissertation**

**zur Erlangung des Doktorgrades**

**Department Physik**

**Universität Hamburg**

vorgelegt von

**Tim Böhnert**

geb. in Hamburg

Hamburg

2014

---

Gutachterin/Gutachter der Dissertation: Prof. Dr. Kornelius Nielsch  
Prof. Dr. Andy Thomas

Gutachterin/Gutachter der Disputation: Prof. Dr. Kornelius Nielsch  
Prof. Dr. Hans Peter Oepen

Datum der Disputation: 28.5.2014

Vorsitzende/Vorsitzender des Prüfungsausschusses: Prof. Dr. Daniela Pfannkuche

Vorsitzende/Vorsitzender des Promotionsausschusses: Prof. Dr. Daniela Pfannkuche

Dekan der MIN-Fakultät: Prof. Dr. Heinrich Graener

---

## Abstract

The relationship of the magneto-thermopower and the anisotropic magnetoresistance/giant magnetoresistance (AMR/GMR) is investigated on individual Co-Ni alloy and Co-Ni/Cu multilayered nanowires. A simple model is developed to distinguish the absolute thermopower contributions without relying on literature values.

A versatile measurement setup is developed for the thermoelectric characterization of electrochemically deposited nanowires. The measured thermopowers and electrical resistivities match reasonably well to those reported in the literature for bulk Co-Ni alloys and GMR thin films. The Co-Ni alloy composition is varied and AMR values as high as -6 % are measured at room temperature (RT). The multilayered nanowires with varying thickness of the Cu layers show typical current-perpendicular-to-plane GMR effects of up to -15 % at RT. A linear dependence between thermopower and electrical conductivity—with the magnetic field as an implicit variable—is found over a wide temperature range (50 K to 325 K). This observation is in agreement with the Mott formula under the assumption of a magnetic field independent thermopower offset, which is related to the absolute Seebeck coefficient of the contact materials. Utilizing this relation, the absolute thermopower and the magneto-thermopower of the nanowires are determined and equal absolute values of magnetoresistance and magneto-thermopower follow. This simple model is tested with different contact materials and compared to the absolute thermopower reported in the literature. Accordingly, the magnetic field independent energy derivative of the resistivity from the Mott formula is calculated.

By changing the composition of the Co-Ni alloy, the thermoelectric power factor is increased by a factor of two as compared to the Ni nanowire. This can be further enhanced by 24 % in perpendicular magnetic fields. The multilayered nanowires show smaller power factors, but are still competitive with high performance thermoelectric nanowires, which might pave the way for energy harvesting applications in the future.

## Inhaltsangabe

Die Beziehung zwischen Magneto-Seebeck Effekt und Anisotropen- bzw. Riesenmagnetowiderstand (AMR bzw. GMR) wird an einzelnen Co-Ni legierten und Co-Ni/Cu Multischicht Nanodrähte untersucht. Ein einfaches Modell wurde entwickelt, um die absoluten Thermospannungsbeiträge ohne Verwendung von Literaturwerten zu unterscheiden.

Ein vielseitiger Messaufbau für die thermoelektrische Charakterisierung von elektrochemisch abgeschiedenen Nanodrähten wurde entwickelt. Die gemessenen Seebeck-Koeffizienten und elektrischen Widerstände passen gut zu den Literaturwerten für Bulk Co-Ni-Legierungen und GMR dünnen Filmen. Die Co-Ni Zusammensetzung wurde variiert und AMR Werte bis zu -6 % bei Raumtemperaturen (RT) gemessen. Die mehrschichtigen Nanodrähte mit unterschiedlicher Cu Schichtdicke zeigen typische GMR Effekte von bis zu -15 % bei RT mit dem Stromfluss senkrecht zur Schichtebene. Eine lineare Abhängigkeit zwischen Seebeck-Koeffizient und spezifischer Leitfähigkeit mit dem Magnetfeld als implizite Variable wurde über einen weiten Temperaturbereich (50 K bis 325 K) gefunden. Diese Beobachtung steht in Übereinstimmung mit der Mott Formel unter der Annahme eines vom Magnetfeld unabhängigen Thermospannungs-Offsets, der mit den absoluten Seebeck-Koeffizienten der Kontaktmaterialien verknüpft ist. Mit Hilfe dieser Beziehung können die absoluten Seebeck-Koeffizienten und der Magneto-Seebeck Effekt der Nanodrähte bestimmt werden und es folgen gleich große Beträge von Magneto-Seebeck Effekt und Magnetowiderstand. Dieses einfache Modell wird an unterschiedlichen Kontaktmaterialien getestet und mit absoluten Seebeck-Koeffizienten aus der Literatur verglichen. Die Magnetfeld unabhängige Ableitung des spezifischen Widerstands nach der Energie wird dementsprechend aus der Mott Formel berechnet.

Durch Verändern der Co-Ni Zusammensetzung verdoppelt sich der thermoelektrische Powerfaktor verglichen mit dem Wert des Ni Nanodrahtes. Eine Erhöhung um weitere 24 % ist in senkrechten Magnetfeldern möglich. Obwohl die multischichtigen Nanodrähte kleinere Powerfaktoren zeigen, sind diese dennoch mit Nanodrähten aus thermoelektrischen Hochleistungsmaterialien Vergleichbar, diese Erkenntnis könnte zukünftig zur Anwendung in der Energiegewinnung führen.

# Table of Contents

<b>Table of Contents</b> .....	<b>5</b>
<b>1 Introduction</b> .....	<b>7</b>
<b>2 Theoretical Background</b> .....	<b>9</b>
2.1 Magnetoresistance.....	9
2.2 Thermopower.....	16
2.3 Magnetism.....	27
<b>3 Nanowire Synthesis</b> .....	<b>33</b>
3.1 Anodization .....	33
3.2 Hard Anodized Aluminum Oxide Membranes .....	35
3.3 Atomic Layer Deposition .....	36
3.4 Preparation Steps.....	37
3.5 Electrodeposition .....	38
3.6 Electrodeposition of Multilayers.....	40
3.7 Release of the Nanowires .....	43
<b>4 Measurement Platform</b> .....	<b>45</b>
4.1 Microscopic Contact Design.....	45
4.2 Macroscopic Circuit.....	48
4.3 Measurement Equipment .....	49
4.4 Measurement Routine .....	51
4.5 Applications of the Seebeck Setup.....	53
4.6 Secondary Effects.....	56
<b>5 Thermoelectric Transport in Anisotropic Magnetoresistance Nanowires</b> .....	<b>61</b>
5.1 Magnetoresistance.....	62
5.2 Magneto-Thermopower.....	71
5.3 The Mott Formula— $S$ vs. $R^{-1}$ .....	75

5.4	Permalloy Nanowires .....	77
5.5	Conclusion AMR and MTEP of Co-Ni alloy Nanowires .....	79
<b>6</b>	<b>Thermoelectric Transport in Giant Magnetoresistance Nanowires.....</b>	<b>81</b>
6.1	Magnetoresistance.....	83
6.2	Magneto-Thermopower.....	88
6.3	The Mott Formula— $S$ vs. $R^{-1}$ .....	93
6.4	Conclusion Co-Ni/Cu Multilayered Nanowires .....	100
<b>7</b>	<b>Conclusion.....</b>	<b>101</b>
	<b>Appendix: Seebeck Measurement Software.....</b>	<b>105</b>
	<b>Appendix: TEM analysis .....</b>	<b>106</b>
	<b>Appendix: Hall and Nernst effect .....</b>	<b>109</b>
	<b>Appendix: Overview of Measurement Results at RT .....</b>	<b>110</b>
	<b>Appendix: Publication List .....</b>	<b>111</b>
<b>8</b>	<b>Bibliography .....</b>	<b>114</b>

# 1 Introduction

The discovery of the *giant magnetoresistance* (GMR) is not only a story of a magnificent breakthrough,<sup>1,2</sup> but also of an application with a significant impact on several aspects of society. Storage devices, which were based previously on the *anisotropic magnetoresistance* (AMR) sensors, were improved in cost, size, and power efficiency. This development accelerated the trend of hard disk miniaturization beyond the initial GMR technology to a point that today a third of the world's population has access to personal computers and the internet. The GMR is known to be an early application in the promising field of nanotechnology and has provided the foundation of the research field of spin transport electronics—called *spintronics*.<sup>3</sup> In addition to the charge of an electron, a second fundamental property—the spin—is utilized in spintronics for advanced magnetic memories and sensors.<sup>4-7</sup> A second topic of current technological interest is the *thermoelectricity*, which describes the interaction of heat and charge transport. The major material property of thermoelectricity—the Seebeck coefficient  $S$ —describes the diffusion of charge carriers due to an applied temperature gradient and was found by Thomas Johann Seebeck in 1821. The behavior of  $S$  in the free-electron model can be described by the Mott formula.<sup>8</sup> Only the relative Seebeck coefficient is experimentally accessible. Therefore,  $S$  is ultimately calculated from observations of the Thomson heat.<sup>9,10</sup> By combining spintronics and thermoelectricity the so called *spin-caloritronics* evolved, which investigates spin caloric effects of spin polarized currents in magnetic nanostructures. The influence on magnetoresistance, thermal transport, and magnetic states is of particular interest of this topic.<sup>11</sup> Due to the observation of the novel spin-Seebeck effect by Uchida *et al.*<sup>12</sup> in 2008 this research field has grown at high pace in spite of critical publications toward the initial finding.<sup>13</sup> A recent systematic study published by Schmidt *et al.*<sup>14</sup> indicates the existence of the spin-Seebeck effect at a much smaller magnitude. Nevertheless, research motivated the development of necessary measurement techniques to investigate conventional transport properties of nanostructures. Measurements of the thermopower (Seebeck coefficient) and magneto-thermopower (spin-dependent Seebeck effect) on single nanowires<sup>15,16</sup> as well as nanostructures like magnetic tunnel junctions<sup>17,18</sup> or spin valves<sup>19,20</sup> show the interest in the thermoelectric properties of nanostructures in particular. Recently, Heikkilä *et al.*<sup>21,22</sup> introduced the concept of spin heat accumulation in perpendicular-to-plane transport in spin valve or multilayered structures, which describes the spin dependent effective electron temperature that might lead to a violation of the Wiedemann-Franz law. This effect increases in low dimensional structures. Therefore, multilayered nanowires are one of the few systems that can be employed to experimentally verify this effect.

Motivated by these fruitful developments in the scientific community, the aim of this work is to contribute to the spin-caloritronics by investigating the thermopower of individual magnetic nanowires. The Co-Ni alloy and Co-Ni/Cu multilayered nanowires are electrochemically deposited into nanoporous alumina templates. Electrical contacts are lithographically defined on top of a single nanowire on a glass substrate. In contrast to measurement approaches performed on platforms,<sup>23-26</sup> in which the particular nanowire has to be assembled on top of a pre-defined structure. The alloy nanowires exhibit the AMR effect, while the magnetic behavior of the multilayered nanowires is dominated by the GMR effect. The high aspect ratio of the nanowires results in a defined magnetization behavior of the alloy nanowires due to pronounced shape anisotropy. Therefore, the composition dependent AMR and magneto-thermopower can be studied under defined magnetization conditions. These effects show magnitudes up to 6.5 % in bulk literature<sup>27,28</sup> as well as in the presented nanowire experiments. In multilayered systems GMR values of 80 % can be achieved by physical deposition,<sup>29,30</sup> while electrochemically deposited nanowires show current-perpendicular-to-plane GMR values of up to 35 %. The magnetic field dependency of  $S$  in materials—showing AMR or GMR effects—can be explained by the Mott formula,<sup>8</sup> which describes the diffusive part of the thermopower.<sup>31-39</sup> A direct relation between  $S$  and  $\sigma$  is predicted, while experimental results do not obey these clear predictions and a more complicated relationship is often presumed. The major experimental difficulty is that only relative Seebeck coefficients are accessible and to obtain the absolute sample value the contact material contributions have to be corrected. Since the thermopower is very sensitive to impurities<sup>40</sup> and shows size effects,<sup>41,42</sup> deviations between literature values and experimental materials have to be considered. This work tries to determine absolute thermopowers utilizing a simple model based on the Mott formula, without relying on literature values. The magnetoresistance, the thermopower, the magnetism, the nanowire synthesis, and the measurement setup are explained in the following. Subsequently, measurement results on AMR, GMR and magneto-thermopower of Co-Ni alloy nanowires and Co-Ni/Cu multilayered nanowires are presented. Finally, the resistance and the thermopower are correlated through the Mott formula with the aim to distinguish the different thermopower contributions.

## 2 Theoretical Background

Currently, the interest in the magneto-thermopower (MTP) of ferromagnetic nanostructures is high, as measurements on single nanowires,<sup>15,16</sup> tunnel junctions,<sup>17,18</sup> and spin valves<sup>19,20</sup> show. Especially, multilayered nanowires are the perfect model system for the experimental investigation of spin dependent perpendicular-to-plane (CPP) transport. The CPP transport is of particular interest in the concept of spin heat accumulation, which is proposed to cause a violation of the Wiedemann-Franz law—ratio of thermal conductivity and electrical conductivity.<sup>21</sup> Crucial to understand the magnetotransport in the nanowire are the resistivity and the magnetoresistance (MR),<sup>43-45</sup> which describes the change of the electrical resistance in external magnetic fields. The resistivity is related to the thermopower by the Boltzmann transport equations or in first approximation by the Mott formula.<sup>8</sup> The theoretical background on magnetoresistance, thermopower, and magnetism is provided in this chapter.

### 2.1 Magnetoresistance

*Magnetoresistance* (MR) effects are a well-known research topic that has been intensively investigated during the last few decades.<sup>43-45</sup> The magnetoresistance describes the change of the electrical resistance in external magnetic fields and is usually given as the relative change:

$$MR = \rho_H / \rho_0 - 1, \quad (2.1-1)$$

with the zero magnetic field resistivity  $\rho_0$  and the resistivity in the magnetic field  $\rho_H$ . A slightly different definition is occasionally used, called *inflated* or “*optimistic*” MR due to possible values above 100 %:<sup>\*</sup>

$$MR_{\text{inf}} = \rho_0 / \rho_H - 1. \quad (2.1-2)$$

The most common MR effect is the “*ordinary*” or the positive magnetoresistance, which shows an increase of the resistivity with the square of the applied magnetic field in metallic materials ( $MR(H) \sim H^2$ ). This effect can be explained in the simple picture of circular motions of the conduction electrons due to the Lorentz force in the applied magnetic field. Therefore, the mean free path between scattering events is effectively reduced and thus the resistivity increases.<sup>46</sup> The positive MR is commonly dominated in ferromagnetic materials by negative

---

\* The negative MR value can be converted into a negative  $MR_{\text{inf}}$  value via:  $MR = (1 - MR_{\text{inf}})^{-1} - 1$  and  $MR_{\text{inf}} = 1 - (MR + 1)^{-1}$ .

magnetoresistance effects. Scattering of the conduction electrons due to spin-disorder, so-called “*magnons*”, causes a negative magnetoresistance. This *magnon magnetoresistance* (MMR) depends linearly on the applied magnetic field ( $MR(H) \sim H$ ).<sup>47</sup> In transition metals like nickel, iron and cobalt an additional *anisotropic magnetoresistance* (AMR) effect appears.<sup>43-45</sup> The effects is distinguished between the transversal and the longitudinal magnetoresistance depending on the alignment (perpendicular or parallel) between magnetic field and current direction. In multilayers of ferromagnetic and non-magnetic layers the so-called *giant magnetoresistance* (GMR)<sup>1,2</sup> can be observed. The terms current-in-plane (CIP) and current-perpendicular-to-plane (CPP) are used to describe the alignment of the current with respect to the multilayers. The AMR and the GMR effects depend on the magnetization, the direction of the magnetic dipole moments, rather than on the applied magnetic field. Therefore, both are generally negative quadratic effects with the magnetic field ( $MR(H) \sim -H^2$ ) and saturate at the characteristic saturation field, when all magnetic dipole moments are aligned with the magnetic field. In the following, the different effects of the measured samples are discussed.

### 2.1.1 Anisotropic Magnetoresistance (AMR)

The anisotropic magnetoresistance (AMR) occurs in ferromagnetic materials like the 3d transition metals nickel, cobalt and iron. The effect was found by Thomson (also known as Lord Kelvin)<sup>48</sup> in 1857 and describes the change of the resistivity dependent on the angle between electrical current and magnetization. The origin of this mechanism in ferromagnetic 3d metals is explained in detail in the textbook by O'Handley.<sup>49</sup> To give a simple explanation it is important to understand the different scattering channels in the transition metals. The 4s and the 3d bands are contributing to the electrical conductivity in these metals. Due to much lower effective mass, the 4s electrons carry most of the current.<sup>50</sup> Due to exchange coupling, the 3d-band splits spin dependent and results in the electron distribution sketched in Figure 2-1. Mott's two-current model describes each of the two spins as a separated conduction path with distinct resistivity.<sup>51-53</sup> The scattering from  $s^\uparrow$  in  $d^\uparrow$  states is at first negligible since the  $d^\uparrow$  band is completely filled. It is reasonable that the resistivity of the  $s^\uparrow$  electrons is small compared to  $s^\downarrow$  electrons and the spin-up channel carries the majority of the current. Small changes in the scattering behavior of the majority channel will have a strong influence on the overall resistivity. Due to the spin-orbit coupling, spin flip scattering is possible and  $s^\uparrow$  electrons can scatter in the  $d^\downarrow$  band as well as  $d^\uparrow$  electrons can scatter in  $s^\downarrow$  states. These two mechanisms open the possibility for s-d scattering of the majority channel, which increases the resistivity significantly. The s-d scattering probability depends on the angle  $\alpha$  between the magnetic moments and the

direction of the electrical current. Therefore, the resistivity is angle dependent and can be written as:

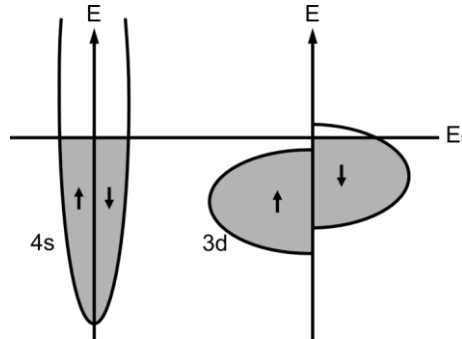


**Figure 2-1** Shown are the 4s and the 3d conduction bands of a ferromagnetic 3d metal, such as nickel. The  $d^{\uparrow}$  electron band is completely filled, while  $d^{\downarrow}$  electron band is partially filled.

$$\rho(\alpha) = \rho_0 \left( 1 + \rho_{sd} / \rho_0 \cdot \cos^2(\alpha) \right), \quad (2.1-3)$$

with resistivity of  $\rho_0$  under zero magnetic field and the additional resistivity due to s-d scattering  $\rho_{sd}$ .

In ferromagnetic bulk samples, the magnetization of the individual magnetic domains is often aligned randomly in zero magnetic fields, as described in section 2.3. In this case a ratio of one to two is expected between the transversal ( $\perp$ ) to the longitudinal ( $\parallel$ ) magnetoresistance, due to two axis perpendicular and one axis along the current direction and the zero magnetic field resistivity can be estimated by  $\rho_0 = 1/3 \cdot \rho_{\parallel} + 2/3 \cdot \rho_{\perp}$ . Any deviations indicate an easy magnetization axis of the sample as described in chapter 2.3.2.

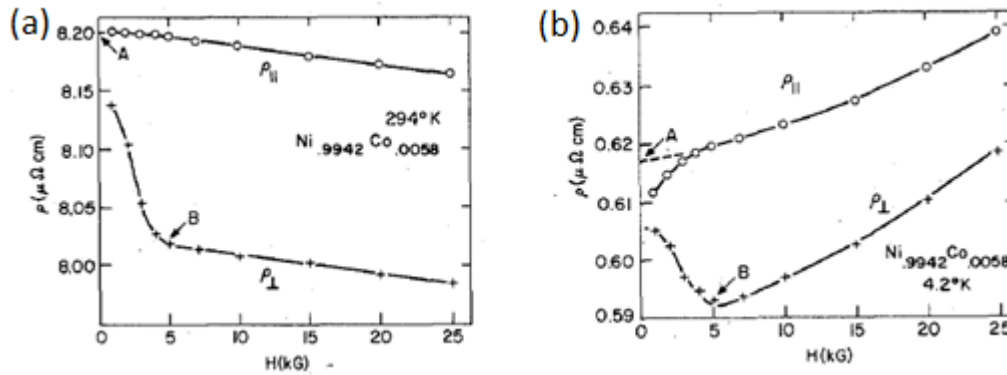


**Figure 2-2 Resistivity of bulk sample as a function of applied magnetic field at (a) room temperature and (b) 4.2 K. The influence above the saturation (point B) of the MMR in (a) and the positive MR in (b) can be clearly distinguished. This figure is taken from McGuire and Potter.<sup>44</sup>**

Figure 2-2(a) shows a decrease of resistivity with the external magnetic field above the saturation, due to MMR, explained in detail in section 2.1.4. In the contrary, Figure 2-2(b) shows an increase of the resistivity above the saturation field indicates that magnons are frozen out at this temperature and the “ordinary” magnetoresistance is dominating. These effects are also present below the saturation field and can lead to deviation in the measured AMR value. To compensate this resistance behavior above the saturation field is often interpolated to zero magnetic field, as shown in Figure 2-2(b) for point A. To compare samples with different magnetizations at zero magnetic field it is common to define the anisotropic magnetoresistance as:

$$\text{AMR} = (\rho_{\parallel} - \rho_{\perp}) / \rho_{av}, \quad (2.1-4)$$

$$\text{with } \rho_{av} = \frac{1}{3}\rho_{\parallel} + \frac{2}{3}\rho_{\perp}.$$

### 2.1.2 Anisotropic Magnetoresistance in Nanowires

Ferromagnetic nanowires show a defined AMR behavior in comparison to bulk materials. Due to the strong shape anisotropy, the magnetic moments aligned with the nanowire axis in zero magnetic field in a single domain state. In Figure 2-3 typical MR curves are shown with different angles between magnetic field direction and the nanowire axis. The resistance decrease in parallel direction is a result of domain wall formation and negligible MR after the resistance jump is a clear indication for uniaxial ferromagnetic behavior of the nanowire. The perpendicular magnetic field will turn the magnetization and lead to a change from maximized to minimized resistivity (not shown in Figure 2-3). Therefore, equation (2.1-4) can be simplified to:

$$\text{AMR}_{\text{NW}} = (\rho_0 - \rho_{\perp}) / \rho_0 \quad (2.1-5)$$

This equation is identical to the original definition of the magnetoresistance in equation (2.1-1) and will be used in the following discussions in order to distinguish the nanowire MR measurements from the AMR literature values on bulk materials. Assuming the nanowires show the same anisotropic magnetoresistance behavior as bulk materials, the difference between literature AMR and measured perpendicular MR is a measure of the magnetization alignment in zero magnetic field. If the difference is small, the magnetization aligns along the nanowire axis in remanence, but if the difference increases this alignment is reduced. At random magnetization distribution in remanence, the perpendicular MR is decreased to one third of the bulk AMR value. The irreversible jumps, called Barkhausen jumps, in the resistance in Figure 2-3 are due to the abrupt magnetization reversal of the nanowire. This reversal process is related to domain wall propagation and theoretical and experimental well known for the nanowire geometry.<sup>54,55</sup> However, this thesis is focused on the general transport behavior of the nanowires under equilibrium magnetization conditions.

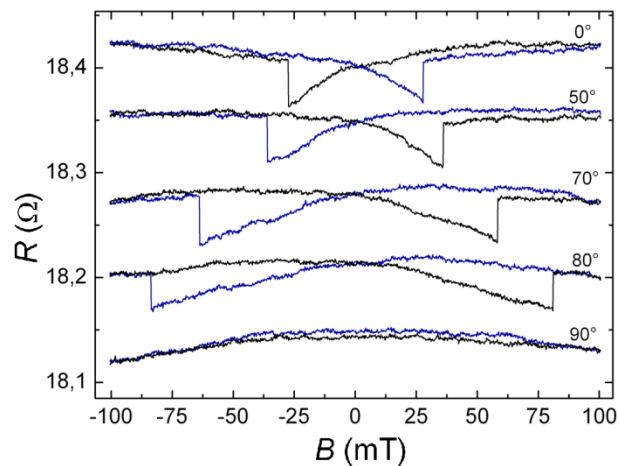


**Figure 2-3 Characteristic MR curves at room temperature of an individual Ni nanowire. The nanowire (270 nm in diameter) is measured at different angles between magnetic field and nanowire axis in the preceding diploma thesis.<sup>56</sup>**

### 2.1.3 Giant Magnetoresistance (GMR)

The giant magnetoresistance (GMR) has its origin in the spin-dependent scattering in ferromagnetic materials. The effect was found in Fe/Cr multilayers by Fert<sup>1</sup> and by Grünberg<sup>2</sup> in Fe/Cr/Fe triple layers at the same time. The magnetoresistance in these samples is much larger than typical anisotropic magnetoresistance values at RT. Today, physical deposition of thin films can achieve GMR values of 80 % at RT.<sup>29,30</sup> To observe the effect a minimum of two ferromagnetic

layers separated by a non-magnetic layer are necessary. Depending on the current direction with respect to the layers, the *current-perpendicular-to-plane* (CPP) and the *current-in-plane* (CIP) GMR can be distinguished. At the saturation field all magnetic segments are aligned parallel to each other and the scattering is minimized, as described later. At lower magnetic fields the magnetization of a certain amount of segments align antiparallel and the scattering is increased. The reason for the antiparallel arrangement is the dipole interaction and the interlayer exchange coupling (RKKY). Whether this coupling promotes parallel or antiparallel alignment depends on the thickness of the non-magnetic layer, which shows in fact an oscillating manner in sputtered samples.<sup>57</sup> Another way to achieve antiparallel alignment is for example engineering alternating coercive fields of each layer.<sup>20</sup> Obviously, the magnitude of the GMR effect depends on the amount of spin dependent scattering processes and the ratio of antiparallel aligned segments compared to the parallel aligned segments. While a perfect parallel alignment can be achieved by applying magnetic fields above the saturation field, a high ratio of antiparallel alignment is challenging and requires precise control of the deposition process. Therefore, samples with the highest effects are fabricated by sputtering under ultra-high vacuum conditions and atomic precision in the layer thickness, as well as controlling the substrate temperature. In sputtered polycrystalline Co/Cu multilayered thin films effects as large as 80 % at RT are obtained,<sup>29,30</sup> but also other methods, e.g. electrochemical deposition, reach GMR effects of 35 %.<sup>58</sup> The definition of the GMR varies between the authors. In this thesis the following definition is used:

$$\text{GMR} = \rho_H / \rho_0 - 1, \quad (2.1-6)$$

where  $\rho_0$  is the resistance at zero magnetic field,  $\rho_H$  is the resistance at the magnetic fields. The “inflated” or “optimistic” GMR can be defined as  $\text{GMR}_{\text{inf}} = 1 - \rho_0 / \rho_H$ , which can reach values above 100 %.

In a 3d ferromagnetic metal—as described for the AMR effect—the conduction band splits dependent on the spin and results in different scattering depending on the spin. This spin dependent scattering leads to a majority spin and a minority spin configuration.<sup>5,59</sup> This uneven spin distribution is called spin polarization, which is defined as the excess of one spin direction normalized to the overall number of spins. In nickel, the spin polarization reaches values of about 15 % or 37 %, <sup>60,61</sup> and recently a polarization of 44 % was determined for Ni nanowires,<sup>62</sup> while up to 100 % can be reached in half-metallic ferromagnets.<sup>63</sup> Meservey and Tedrow published a comprehensive review on several spin-polarization measurement methods and different results on Ni, Co, Fe, and other materials.<sup>64</sup> A suitable model for the description of the spin

polarized current in the different magnetic segments is the Mott two-current model, which distinguishes two parallel current channels by the spin.<sup>50</sup> Electrons with spin  $S$  aligned parallel to the magnetization  $M$  will be scattered less than the electrons with spin antiparallel to the magnetization, leading to two resistances  $R_{\uparrow\uparrow}$  and  $R_{\downarrow\downarrow}$ . The parallel configuration of spin and magnetic moment has a lower resistance than the antiparallel configuration:  $R_{\uparrow\uparrow} < R_{\downarrow\downarrow}$ . As a result, in a perfectly antiparallel alignment ( $R_{AP}$ )\* of the magnetization, as shown in Figure 2-4(a), both spin currents are equally scattered resulting in equation (2.1-7). While saturation of the entire magnetization, as shown in Figure 2-4(b), the majority carriers of the polarized current are scattered less, which decreases the overall resistance in the parallel alignment ( $R_P$ ) to equation (2.1-8). While this picture is straightforward in the CPP geometry, it is not as suitable for the CIP geometry. The latter was first discovered and easier to measure in thin films, while in the case of nanowires the CPP geometry is easier to realize. Therefore, the following discussions are focused on the CPP GMR. The relevant CPP length scale for the non-magnetic interlayer is the spin diffusion length (about 40 nm), whereas in the case of CIP GMR the shorter mean free path of the electrons (about 2 nm) is relevant.

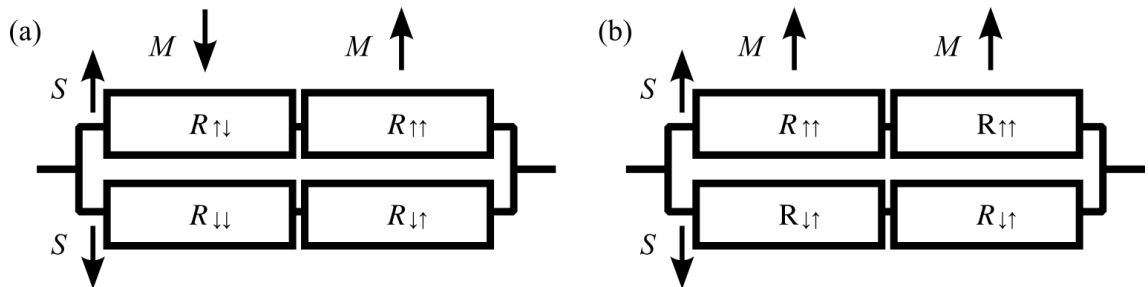


**Figure 2-4 Sketch of the GMR circuit of two ferromagnetic layers, displaying anti-parallel alignment in (a) and parallel alignment in (b). The nomenclature for the resistances is defined as:  $R_{SM}$ .**

$$R_{AP} = \frac{R_{\downarrow\uparrow} + R_{\uparrow\uparrow}}{2} \quad (2.1-7)$$

$$R_P = \frac{2R_{\downarrow\uparrow}R_{\uparrow\uparrow}}{R_{\downarrow\uparrow} + R_{\uparrow\uparrow}} \quad (2.1-8)$$

\* A perfect alignment cannot be expected experimentally, when averaging over hundreds of multilayers. In fact, values down to 61 % antiferromagnetic alignment are reported.<sup>89</sup> Therefore, the experimental zero field value is in between  $R_{\uparrow\uparrow}$  and  $R_{\downarrow\uparrow}$ .

### 2.1.4 Magnon magnetoresistance (MMR)

The conception of a completely ordered ferromagnetic system above the saturation field is technically not correct. Thermal energies introduce collective spin excitations, called *magnons*, into the material system. To suppress this spin-disorder completely, magnetic fields in the order of 2000 T are theoretically necessary for Fe at 450 K.<sup>47</sup> The magnons scatter with the electrons and add an additional magnetoresistance component. Raquet *et al.*<sup>47,65</sup> extended the formalism of Godings to describe the MMR in large applied magnetic fields. Strictly speaking, this formalism is only valid far above the technical saturation ( $B \gg \mu_0 M_S$ ) because it is not considering the anisotropy energy and spin-wave demagnetization, which would modify the internal magnetic field. However, it can be extended to be valid in small magnetic fields, as shown by Mihai *et al.*<sup>66</sup> Using an approximation for magnetic fields below 100 T and temperatures above a fifth of the Curie temperature, the following equation can be derived:

$$\Delta\rho_{\text{MMR}}(H) \propto \frac{BT}{D(T)^2} \ln\left(\frac{\mu_B B}{k_B T}\right), \quad (2.1-9)$$

with the exchange stiffness  $D(T) = D_0 - D_1 T^2 - D_2 T^{5/2}$ , and  $D_0$  denoting the zero-temperature magnon mass.  $D_1/D_0$  and  $D_2/D_0$  are in the order of  $10^{-6} \text{K}^{-2}$  and  $10^{-8} \text{K}^{-5/2}$ . Since most measurement setups are limited to magnetic fields of a few tesla, deviations from the theory due to insufficient magnetic fields are expected. Additionally, the approximations might lead to deviations below 150 K. Equation (2.1-9) shows an approximately linear slope of the resistance with the applied magnetic field above the saturation field, which is given by the following equation:

$$\frac{\partial \Delta\rho_{\text{MMR}}(T, B)}{\partial B} \propto T(1 + 2D_1/D_0 T^2)(\ln T + c), \quad (2.1-10)$$

with  $c$  being a temperature independent offset. According to Raquet *et al.*,<sup>47,65</sup> this slope of the resistivity at high fields is about  $0.01\text{--}0.03 \mu\Omega\text{cmT}^{-1}$  for ferromagnetic 3d transition metals. This corresponds to a MR of about 0.1 % at 1 T. Compared to AMR and GMR effects this value is between one or two orders of magnitude smaller. Nevertheless it is often necessary to correct the individual measurements by the MMR effect.

## 2.2 Thermopower

Thomas Johann Seebeck discovered the thermopower or Seebeck effect in 1821. He observed that a temperature gradient in a metal would deflect a close by ferromagnetic compass needle. He first attributed this to a magnetic effect, but it was later shown that the temperature gradi-

ent created an electrical current with a corresponding Oersted field that influenced the compass needle. A few years later Jean-Charles Peltier discovered the reversed effect. By applying an electric potential to a metal, the electrical current heats one electrical contact while cooling the other. In 1851, William Thompson (Lord Kelvin) predicted and later observed an effect, called Thompson effect, which leads to heat emission or absorption in a metal depending on the alignment of the applied temperature gradient and current. In 1854, Lord Kelvin proposed that the Seebeck effect and the Peltier effect have the same origin and can be described by the Thompson relation  $\Pi = S \cdot T$ , where  $\Pi$  is the Peltier coefficient,  $S$  is the thermopower and  $T$  is the average temperature. This was proven by Onsager almost 80 years later. Until the nineties of the last century, decent efforts were invested to further investigate these effects. Recently, the thermoelectric properties of nanostructured materials in magnetic fields moved into the focus. Conventional Seebeck measurements on ferromagnetic single nanowires<sup>16</sup> and advanced structures like magnetic tunnel junctions<sup>17,18</sup> and spin valves<sup>19</sup> account for the interest in these properties. The origin of the Seebeck effect lies in the temperature dependence of the average thermal energy of the electrons due to the Fermi-Dirac distribution. In highly conductive metals, the heat is mostly carried by electrons.<sup>67</sup> For fermions (e.g. electrons) the Pauli principle has to be applied and the electrons are distributed dependent on their energy between the available states. The Fermi-Dirac distribution is the result of this consideration (see Figure 2-5(b)):

$$f^{\text{FD}}(E, T) = \left( e^{\frac{E - E_F}{k_B T}} + 1 \right)^{-1} \quad (2.2-1)$$

This equation describes the distribution of the electron energy  $E$  by the difference to the Fermi energy  $E_F$ —the energy of the highest occupied state at zero temperature—and the average thermal energy  $k_B T$  of the electrons.

In three dimensions, the density of states is given by  $D(E) \sim \sqrt{E}$  and the electron distribution is defined as follows (see Figure 2-5(a)):

$$n(E) = \int_0^{\infty} f^{\text{FD}}(E, T) \cdot D(E) dE \quad (2.2-2)$$

Only electrons that are close to the Fermi energy participate in the diffusion process and transport thermal energies.<sup>68</sup> Thus, in metals the average energy of the electrons that are capable to diffuse can be calculated by integrating the energy of the electrons close to the edge of the electron density distribution. Due to the Fermi-Dirac distribution (equation (2.2-1)) this average energy increases with temperature, as schematically shown in Figure 2-5(c). As a result, in

order to reduce their average energy, the free charge carriers diffuse generally to the cold contact area. This process is theoretically explained in detail, by Goldsmid.<sup>69</sup> The accumulation of charge carriers at the cold side builds up the so-called thermoelectric voltage. The proportionality factor between thermoelectric voltage  $U_{\text{thermo}}$  and temperature difference  $\Delta T$  across a sample is called the Seebeck coefficient  $S$ .

$$S = - \frac{\phi_{\text{HOT}} - \phi_{\text{COLD}}}{T_{\text{HOT}} - T_{\text{COLD}}} = - \frac{U_{\text{thermo}}}{\Delta T} \quad (2.2-3)$$

with the potential difference between the hot and cold side as the numerator and the temperature difference as the denominator. This coefficient is an intrinsic material property (not an interface effect) and it is always measured with respect to a contact material and defined either absolute (against a superconductor) or relative to platinum contacts. Per definition, the Seebeck coefficient is negative if electrons diffuse towards the cold side of the sample. Thus, electron conductors have in general a negative Seebeck coefficient, but some metals exhibit a positive one. In these cases, a strong reduction of the mean free path with the temperature overcomes the average energy increase and electrons diffuse to the hot part of the sample. In simple words: Although the hot electrons have higher energy, they are even more likely to scatter and diffuse effectively less than the cold electrons. This relation is also evident in the Mott formula, which describes  $S$  in the free-electron model:<sup>8</sup>

$$S(E) = \frac{\pi^2}{3} \frac{k_B^2 T}{q} \left( \frac{d \ln \sigma(E)}{dE} \right)_{E=E_F} \quad (2.2-4)$$

where  $q$  is the carrier charge,  $k_B$  is the Boltzmann constant,  $\sigma$  is the electrical conductivity, which is given according to the Drude model by the product of density  $n$ , charge  $e$  and mobility  $\mu$  of electrons  $\sigma = ne\mu$ ,<sup>70</sup> and  $E$  is the Energy of the charge carrier. The Mott formula is a first order approximation of the Boltzmann transport equation in  $k_B T/E_F$  and deviations can be expected at very high temperatures ( $\sim 1000$  K).<sup>8</sup> The formula describes only the diffusive thermopower and should be carefully treated at temperatures with significant phonon-drag or magnon-drag thermopower contributions. The different Seebeck coefficients at room temperature (RT) of certain metals and the half-metal bismuth, which shows a very high effect, are shown in Table 2-1.

As already mentioned, Seebeck coefficients are always measured with respect to a contact material. More specifically, the measured thermovoltage consists of distributions of every part of the measurement circuit, which involves a temperature gradient. In Figure 2-6 an example of

three materials used in a circuit with temperatures  $T_1$  to  $T_4$  at the connections is shown. The measured thermovoltage would be:

$$U_{\text{thermo}} = S_{\text{red}}(T_1 - T_2) + S_{\text{green}}(T_2 - T_3) + S_{\text{red}}(T_3 - T_4) + S_{\text{black}}(T_4 - T_1), \quad (2.2-5)$$

Transferred to a real measurement structure, the green material represents the sample, the red material the lithographic contacts and the black section any cables, connections, bond wires necessary to close the measurement circuit. From equation (2.2-5) it is clear that in addition to the thermovoltage of the sample at least a second voltage is always present.

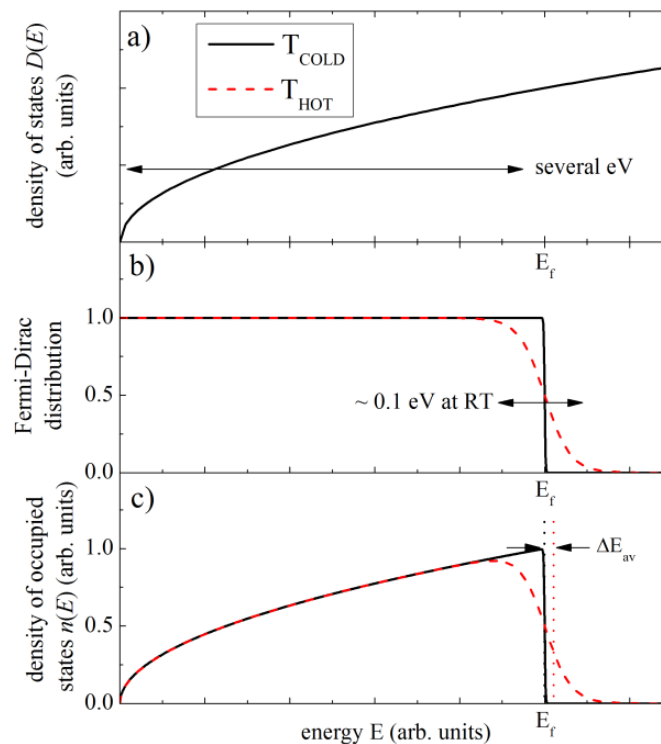


**Figure 2-5 (a) Density of states for a free 3D electron gas  $D(E)$ . (b) Fermi-Dirac distribution functions at two temperatures. (c) Density of occupied states of the two temperatures and the resulting difference in average energy of conduction electrons.\***

\*The relative width of Fermi distributions region is exaggerated in the sketch by calculating with temperatures of roughly RT and 10000 K.

**Table 2-1 Seebeck coefficients of different materials at RT from literature are shown in reference to platinum and absolute values.**

element	$S / \mu\text{VK}^{-1}$	$S^{\text{abs}} / \mu\text{VK}^{-1}$
Bi	-50 <sup>71</sup>	-55
Co	-25.8 <sup>72</sup>	-30.7
Ni	-14.5 <sup>73</sup>	-20.4
Pt	0	-4.92 <sup>9</sup>
Cu	6.14 <sup>74</sup>	1.9 <sup>9</sup>
Au	7	2.08 <sup>9</sup>
Fe	20 <sup>75</sup>	15

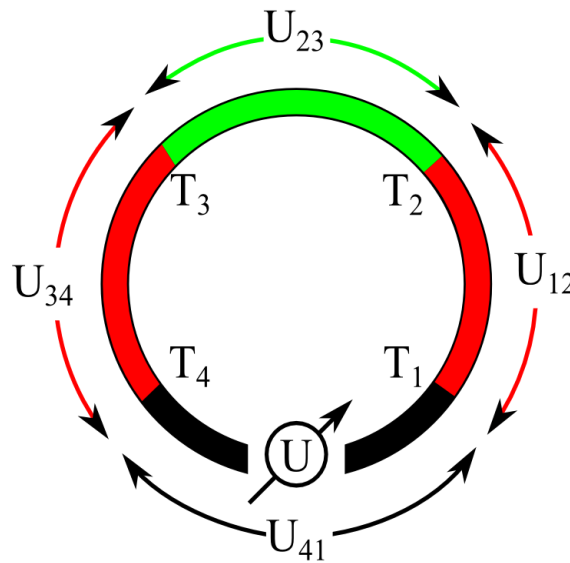


**Figure 2-6 Sketch of a circuit consisting of three materials to illustrate the different thermal voltages, which depend on the temperatures at the interfaces.**

In the case of a constant temperature in the black section ( $T_1=T_4$ ), this section contributes no thermovoltage and equation (2.2-6) follows:

$$U_{\text{thermo}} = (S_{\text{green}} - S_{\text{red}})(T_2 - T_3) \quad (2.2-6)$$

In reality, it is challenging to remove the “black” contribution, because the black section consists of various materials at different temperatures. Therefore, it would be necessary to design the circuit materials and temperatures symmetrical. An asymmetry results in a constant thermovoltage offset in the range of a few  $\mu\text{V}$  in the setup. Since the temperatures outside of the sample area are relatively constant, it is possible to determine the voltage offset  $U_{\text{offset}}$

when no power is applied to the microheater ( $T_2=T_3$ ), which leads to equation (2.2-7). Considering this offset, equation (2.2-6) has to be modified by subtracting the offset from the measured thermovoltage (equation (2.2-8)), which finally leads to (2.2-9).

$$U_{\text{offset}} = S_{\text{red}}(T_1 - T_4) - S_{\text{black}}(T_1 - T_4) \quad (2.2-7)$$

$$U_{\text{thermo}} = U_{\text{measured}} - U_{\text{offset}} \quad (2.2-8)$$

$$S_{\text{green}} - S_{\text{red}} = \frac{U_{\text{measured}} - U_{\text{offset}}}{T_2 - T_3} \quad (2.2-9)$$

The size of the Seebeck coefficient is crucial for the power output and efficiency of the conversion from heat power to electrical power in a thermoelectric device. Additionally, the electrical conductivity  $\sigma$ , the thermal conductivity  $\kappa$  at an average temperature of the device  $\bar{T}$  characterize the performance of a thermoelectric material, but in contrast to  $S$  these parameters are closely coupled through the Wiedemann-Franz law or predetermined by the device application.<sup>76,77</sup> The figure of merit  $Z\bar{T} = S^2\sigma\bar{T}/\kappa$  summarizes the material parameters and is commonly used to compare devices. A high  $Z\bar{T}$  leads to a high power conversion efficiency. Alternatively, the power factor  $\text{PF}=S^2\sigma$ , which is a measure of the power output or throughput of a thermoelectric device, can be used for benchmarking.<sup>78</sup> The PF neglects the thermal conductivity. Nevertheless, depending on the application the PF provides a more appropriate performance index than the  $Z\bar{T}$  value. In particular, in exhaust systems the heat flow and available surface area are typically predefined parameters and high PF materials can convert more heat power than high efficiency (high ZT) materials and are more efficient under specific conditions.<sup>79,80</sup>

### 2.2.1 Phonon-drag Thermopower

The previously mentioned thermopower described by the Mott formula solely arises due to the thermal energy of the electrons and is often called diffusive thermopower. If the charge carriers dominantly scatter with impurities and lattice defects, this is a valid description of the thermopower. However, also collisions with other particles have to be considered. *Electron-phonon* collisions are a typical example that can give rise to additional thermopower called *phonon-drag*, which was first described for semiconductors.<sup>81,82</sup> With a temperature gradient present, the lattice vibrations transfer heat and momentum to the electrons and "drag" them in direction of the cold side. Whether this non-equilibrium effect is detectable, depends strongly on the remaining scattering mechanism of the phonons and electrons. MacDonald argues in his book<sup>68</sup> that the *phonon-phonon* interactions increase linear with the temperature  $T$ , while phonon-electron interactions are roughly temperature independent. Therefore, the probability for

phonon-electron scattering compared to phonon-phonon interaction is expected to decrease with  $1/T$  and is negligible at  $RT^*$ .<sup>68,83</sup> At low temperatures in sufficiently pure metals phonon-electron collisions are dominant as predicted by the Debye model, but as the specific heat of the lattice decrease with decreasing temperature the energy of the phonons decrease very rapidly with  $T^3$  as well. A maximum of the phonon-drag contribution between 5 K and 50 K can be expected for reasonable pure metals. In metals with a significant amount of impurities or defects, the phonon-electron interactions are comparably small and the phonon-drag is not observable. It turns out that in most metals the phonon-drag give rise to a positive thermopower and the simple picture of electrons being dragged to the cold side is wrong. From phonon-phonon scattering a mechanism called “Umklapp” process is known. This is a three particle scattering process without momentum conservation, because one phonon is undergoing a Bragg reflection by the lattice itself. The chance for a similar “Umklapp” process in electron-phonon scattering is expected to increase exponentially with temperature. Due to the Bragg reflection the electron momentum reverses and the sign of the phonon-drag thermopower changes. The “Umklapp” scattering seems to be the dominating process in metals like Au, Ag, Cu or Pt.<sup>10,84,85</sup> The diffusive thermopower is independent of the phonon-drag, as it does not change the heat capacity of the electrons, which is responsible for the diffusion. Therefore, both contributions are independent of each other and simply add up.<sup>40,68</sup> Additionally, there is evidence that in nanostructures the phonon-drag is influenced by size effects, but it seems quite difficult to evaluate these results comprehensively.<sup>41,42,86</sup>

$$S = S_{p-e} + S_{diffusion}. \quad (2.2-10)$$

### 2.2.2 Matthiessen’s Rule and Nordheim-Gorter Rule

The ions in metals are arranged in lattice structures, which ideally have a vanishing residual resistance at zero temperature. Any defects that destroy the symmetry of the lattice will introduce scattering sites and thus a residual resistance. Additionally, at higher temperatures, lattice vibrations called phonons interact with electrons and add a scattering component. Similarly,

---

\* Theoretical estimations of the phonon spectrum according to Debye theory result in significant phonon-drag at  $RT$ .<sup>83,205</sup> MacDonald suggests in his book a precise cancelation of “normal” phonon-drag and “Umklapp” phonon-drag at higher temperatures,<sup>68</sup> but Blatt disagrees strongly and suggests a “quite general failure of the Debye model in predicting the true phonon spectrum” for temperatures higher than the Debye temperature.<sup>83</sup>

electron-electron interactions, spin dependent scattering and magnon interactions are possible. In the simplest model, the overall resistance or the electrical conductivity can be described by the Drude model:<sup>70</sup> by  $\rho = m^*(ne^2\tau)^{-1}$  or  $\sigma = ne^2\tau/m^*$ , where  $n$  is the charge carrier density,  $m^*$  is their effective mass,  $q$  is their charge and  $\tau$  is the mean free time between scattering events. According to Matthiessen's rule with the simple approximation that the individual scattering mechanisms are independent of each other, the respective scattering times add up inversely to the total resistivity:<sup>87</sup>

$$\rho = \frac{m^*}{ne^2} \sum_i \tau_i^{-1} = \sum_i \rho_i. \quad (2.2-11)$$

In order to transfer this relation to the thermopower, it is useful to picture a series of sources of thermopower  $S_i$ , as sketched in Figure 2-7(a). The thermal voltages of the individual effects simply add up, but the applied temperature gradient is divided between the sources and the relation has to be modified. The distribution of the temperature gradient is proportional to their thermal resistances  $W_i$ . According to the Wiedemann-Franz law—which can be considered valid for highly conductive metals—the heat flow is carried entirely by the conduction electrons.<sup>76,77</sup> Therefore, the temperature gradient divides proportional to the respective resistances and following equation can be derived, which is generally referred to as the Nordheim-Gorter rule:<sup>88</sup>

$$S = \frac{\sum_i \rho_i S_i}{\sum_i \rho_i}. \quad (2.2-12)$$

According to the discussion by Gold *et al.*<sup>84</sup> this rule is valid under certain conditions in the microscopic scale for a single conductor with various scattering mechanism present. In the case of a series of materials with different geometries, the resistances replace the resistivities.

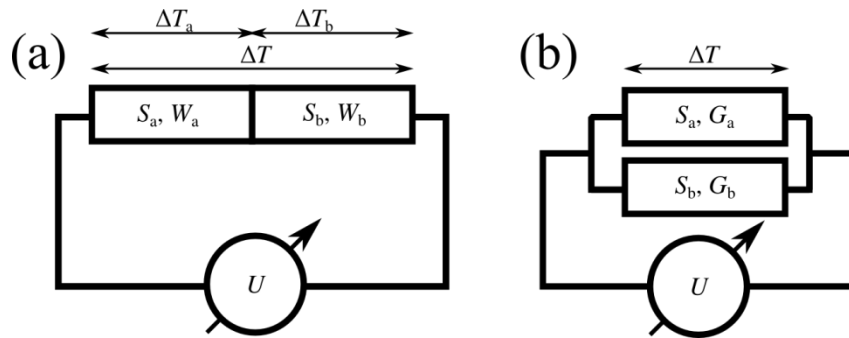


**Figure 2-7 Schematic representation of the thermovoltage circuits considering a (a) serial arrangement/(b) parallel arrangement of two materials with applied temperature gradient  $\Delta T$ , Seebeck coefficient  $S$ , thermal resistance  $W$  and conductance  $G$ .**

### 2.2.3 Two-Band Model

In the previous section, independent scattering mechanisms are discussed in the picture of in series connected sources. This section will treat effects in the macroscopic view of two parallel connected materials, as shown in Figure 2-7(b). This model is used to describe the thermopower analogical to Mott's two-current model for the AMR and GMR effect, but also to estimate the Seebeck coefficient in intrinsic semiconductors with two types of charge carriers. The general description of electrical and thermal voltage according to Ohm's law is given in equations (2.2-13). By considering two parallel sources of thermal voltages and setting the total current to zero, as required for a thermovoltage measurement, equation (2.2-14) is acquired. Similar to the arguments on bipolar effects in the book of Goldsmid<sup>69</sup> and in the last chapter of the book of MacDonald<sup>68</sup> equation (2.2-15) can be derived, which weights each Seebeck coefficient  $S$  by the corresponding conductance  $G$ . In a more general case of  $i$  parallel sources of a thermovoltage with equal temperature differences equation (2.2-16) can be used.\*

---

\* In literature the conductivity is used instead of the conductance, because the equation is commonly applied to the microscopic two-band model for two different types of carriers in which case geometries can be neglected.

$$I = \left( \frac{U}{R} - \frac{S\Delta T}{R} \right) \quad (2.2-13)$$

$$I = I_a + I_b = 0 \quad (2.2-14)$$

$$S = \frac{S_a G_a + S_b G_b}{G_a + G_b} \quad (2.2-15)$$

$$S = \frac{\sum_i G_i S_i}{\sum_i G_i} \quad (2.2-16)$$

### 2.2.4 Magneto-Thermoelectric Power

The relative change of the Seebeck coefficient under the applied magnetic field  $H$  is called *magneto-thermoelectric power*,

$$\text{MTEP} = \frac{U_{\text{thermo}}(H) - U_{\text{thermo}}(0)}{U_{\text{thermo}}(0)}. \quad (2.2-17)$$

$U_{\text{thermo}}$  describes the measured thermovoltage in reference to the contact material. In the case of  $S_{\text{NW}}^{\text{abs}} \approx S_{\text{contact}}^{\text{abs}}$  (explained in detail in the beginning of section 2.2) the MTEP can reach infinite values. Therefore, the MTEP should be treated with caution and is commonly given against platinum contacts. In agreement with Gravier *et al.*<sup>31</sup> the term *magneto-thermopower* (MTP) will be used to describe the magneto effect relative to the absolute Seebeck coefficient of the sample:

$$\text{MTP} = \frac{S_{\text{NW}}^{\text{abs}}(H) - S_{\text{NW}}^{\text{abs}}(0)}{S_{\text{NW}}^{\text{abs}}(0)} = \frac{U_{\text{thermo}}(H) - U_{\text{thermo}}(0)}{U_{\text{thermo}}(0) - S_{\text{contact}}^{\text{abs}}(0) \cdot \Delta T}, \quad (2.2-18)$$

with the absolute material values  $S^{\text{abs}}$ , while  $U_{\text{thermo}}$  is the measured value in reference to the contact material. To be consistent with the inflationary MR, the inflationary MTP is defined as:

$$\text{MTP}_{\text{inf}} = \frac{S_{\text{NW}}^{\text{abs}}(H) - S_{\text{NW}}^{\text{abs}}(0)}{S_{\text{NW}}^{\text{abs}}(H)}. \quad (2.2-19)$$

The difficulty in obtaining MTP is to remove the absolute Seebeck coefficient of the contact materials. Absolute literature values are available for most metals from low temperature to room temperature, but these values are very sensitive to impurities<sup>40</sup> and show size effects.<sup>41,42</sup> Therefore, they depend on the fabrication technique and deviations between literature values and experimental materials should be considered. Consequently, the MTEP is frequently used in literature to describe magnetic effects on the thermovoltage. Unlike the resistance, the See-

beck coefficient is a material property and can be used for comparison of samples. Therefore, not only MTEP and MTP values but also the absolute change of the Seebeck coefficient  $\Delta S$  due to the applied magnetic field is used to characterize samples.

There are two different approaches to explain the magnetic field dependency of the thermopower in ferromagnetic alloys and multilayered samples. The microscopic approach is analogue to Mott's two-current model for the AMR and GMR, as explained in the previous chapter. It assumes different Seebeck coefficients for minority and majority carriers and calculates the total Seebeck coefficient according to equation (2.2-12) and (2.2-16) for the different alignments (sketched in Figure 2-4).<sup>31,32,40,89</sup> With this model the Seebeck coefficients of minority and majority channels of Co and Ni can be calculated. Cadeville *et al.*<sup>40</sup> introduced impurities to the system to determine these parameters at room temperature, which seem to produce reliable results with an experimentally challenging approach. While Shi *et al.*<sup>32</sup> and Gravier *et al.*<sup>31</sup> varied only the magnetic fields. For defined boundary conditions, complete antiparallel alignment has to be assumed in order to calculate the properties of the separated channels. It turns out that dependent on the sample this is a poor estimation.<sup>89</sup> In conclusion, it seems this approach is experimentally difficult or leads to a more complex macroscopic description due to undefined boundary conditions.\* The second approach directly relies on the Mott formula<sup>†</sup> and relates measured properties—resistivity and Seebeck coefficient—in an applied magnetic field. This macroscopic description seems to work well for this work and is discussed in detail in the next chapter.

### 2.2.5 Resistivity and Thermopower in the Magnetic Field

From the Mott formula (2.2-4) two equivalent equations (2.2-20) and (2.2-21) are derived. It becomes evident that the Seebeck coefficient depends on temperature and electrical conductivity or resistivity, respectively, but also on the derivatives of the energy:

$$S = \frac{cT}{\sigma} \left( \frac{d\sigma(E)}{dE} \right)_{E=E_f} \quad (2.2-20)$$

$$S = -\frac{cT}{\rho} \left( \frac{d\rho(E)}{dE} \right)_{E=E_f} \quad (2.2-21)$$

---

\* It seems the author and other scientists come to a similar conclusion, since in following publications this theory is only qualitatively evaluated.<sup>31,89</sup>

† Strictly speaking, the first approach relies indirectly on the Mott formula, due to certain necessary assumptions.

with  $c = \pi^2 k_B^2 / 3q$ ,  $q$  being the charge of the carrier,  $k_B$  the Boltzmann constant,  $\sigma$  the electrical conductivity,  $\rho$  the electrical resistivity, and  $E$  the energy of the charge carrier. The energy derivatives are attainable by first principle calculations, but this is rarely done. Only a few publications consider the band structure.<sup>90-92</sup> The major question is the magnetic field dependency of the energy derivatives. If one of the derivatives is magnetic field independent, a linear relationship between  $S$  and either  $\sigma$  or  $\rho$  follows. One of the first publications, that use the linear relationship between  $S$  and  $R^{-1}$  discovered by Nordheim and Gorter<sup>84,88</sup> to directly relate MTP and MR was Conover *et al.*<sup>36</sup> Although, the displayed relation is actually not expected for their data due to different temperatures, this is one of the few publications that come to these conclusions. Up to now in several magnetic systems, like granular alloys, magnetic/non-magnetic multilayers, spin valve structures and alloyed samples, a linear dependency of the Seebeck coefficient on the electrical conductivity under an applied magnetic field has been found.<sup>31-39,90,93-95</sup> By comparing the linear relationship to equation (2.2-21) it seems reasonable to assume that  $(d\rho(H)/dE)$  at the Fermi energy is independent of the applied magnetic field. This rule seems to be valid for typical ferromagnetic materials, but certain magnetoresistance components might differ from the linear relationship (e.g. magnon effects and domain wall effects) and need deeper investigation.<sup>39,96</sup>

## 2.3 Magnetism

In order to understand the complex interplay between the shape anisotropy of the nanowires, the alloy composition, and the magnetic properties these subjects are discussed in the following chapter. The main focus is not the micromagnetism itself, but the different magnetic anisotropy contributions, which will be important to understand the first experiments in chapter 5.

### 2.3.1 Ferromagnetism

In contrast to paramagnets and diamagnetic materials, ferromagnetic materials show a spontaneous magnetization in the absence of external magnetic fields. This effect originates from a parallel alignment of the individual magnetic moments in ferromagnetic materials like iron, nickel, or cobalt. These metals are ferromagnetic at room temperature and the ferromagnetism only vanishes above a critical temperature  $T_c$  at which they become paramagnetic. The total energy  $E_{\text{total}}$  of a ferromagnetic material, neglecting the surface anisotropy, can be described as following:

$$E_{\text{total}} = E_A + E_{\text{Zee}} + E_D + E_K, \quad (2.3-1)$$

with the exchange energy  $E_A$ , the Zeeman energy  $E_{Zee}$ , the stray field energy  $E_D$  and the magnetocrystalline anisotropy  $E_K$ . In the equilibration state, the total energy of a ferromagnetic structure is minimized and in general magnetic domains are formed, in which the magnetic moments show homogeneously in one direction. The region with inhomogeneous magnetization that connects neighboring magnetic domains with different preferred directions is called domain wall. In the following, the individual energy components and their influence of the domain structure will be discussed.<sup>67</sup>

### Exchange Energy

The Heisenberg model describes the exchange energy as the sum of exchange interaction of atom pairs  $(i,j)$  in a crystal by:

$$E_A = -\sum_{i,j} J_{ij} \vec{S}_i \cdot \vec{S}_j . \quad (2.3-2)$$

The exchange integral  $J_{ij}$  has a quantum mechanical origin and is connected to the overlap of the wave functions of the charge density of the atoms.<sup>97</sup> With a positive  $J_{ij}$  the energy of parallel-aligned magnetic moments is minimized, which is characteristic for ferromagnetic behavior, while for negative  $J_{ij}$  the antiparallel alignment is preferred. A strong parallel alignment of the moments will lead to larger magnetic domains and less domain walls.

### Zeeman Energy

The Zeeman energy originates in the interaction of the external magnetic field and the magnetic moments. The contribution to the total magnetic energy is minimal, if the magnetization of the ferromagnetic material aligns with the external magnetic field  $\vec{H}_{ex}$ . For a homogeneous external magnetic field the Zeeman energy  $E_{Zee}$  only depends on the average magnetization  $\vec{M}$  of the material rather than on the special spin structure or the geometry and can be written as:

$$E_{Zee} = -\vec{M} \cdot \vec{H}_{ex} . \quad (2.3-3)$$

### 2.3.2 Magnetic Anisotropy

As discussed, in the equilibrium the magnetic structure is in a state of minimized total energy. This state will change in dependence of the external magnetic field. Certain orientations are preferred and called easy axes, while directions of higher total energy are called hard axes. The two competing contributions that induce these preferred axes are the shape anisotropy and the magnetocrystalline anisotropy.

### Shape Anisotropy

The shape anisotropy is the result of the stray field energy. This energy component is small if the stray field outside of the material is small. Usually, the dipole interactions are weak and long range compared to the exchange interactions. As the ferromagnetic material is structured in high aspect ratios, the stray field contribution of magnetic moments at the surface becomes dominant and the domain structure tends to align with the shape of the sample. This change of the preferred orientation is usually along the longest axis of the sample. In a nanowire, the magnetization preferably aligns along the nanowire axis and (depending on the diameter of the nanowire) form vortex states at each end of the nanowire.<sup>56</sup> Instead of using the stray field, it is equivalent and often easier to consider the demagnetization field  $\vec{H}_D$  inside of the sample that arises from the interaction of the magnetic dipoles. By approximating the nanowire as a prolate spheroid of infinite length, the demagnetization field perpendicular to the nanowire axis is approximated to be  $H_D = 2\pi M_S$ .<sup>98</sup> The demagnetization energy  $E_D$  is small, if each magnetic dipole aligns with this demagnetization field and can be written as follows:

$$E_D = -\frac{1}{2} \vec{M} \cdot \vec{H}_D \quad (2.3-4)$$

### Magnetocrystalline Anisotropy

The shape anisotropy is usually competing with a second contribution, which is the magnetocrystalline anisotropy. In a single crystal, it is clear that the distance between atoms is different depending on the crystal axes. Through the spin-orbit coupling the charge density is not spherical and turns with the magnetic moment. Therefore, the overlap of the wave functions of the charge density, which are considered in the exchange energy contribution, varies between the crystal axes. The magnetocrystalline energy is usually given dependent on the angle  $\phi$  between magnetization and a specified crystal axis. As an example the anisotropy of hexagonal cobalt with respect to the c-axis with the anisotropy constants  $K_1$  and  $K_2$  is shown:

$$E_k = K_1 \sin^2 \phi + K_2 \sin^4 \phi + O(6) \quad (2.3-5)$$

Depending on the type of crystal structure, material composition, and orientation to the shape of the sample there can be several easy axes. Choosing complimentary materials can reduce the effective magnetocrystalline anisotropy of alloys. Permalloy, an alloy of 20 % iron and 80 % nickel, shows an isotropic behavior. Although the magnetocrystalline anisotropy is the result of the crystal structure, it can have noticeable effects in nanocrystalline or polycrystalline samples. The magnetocrystalline anisotropy in polycrystalline samples often show a random orientation

in the crystals and vanish in average. Nevertheless, the magnetocrystalline anisotropy will compete with the shape anisotropy in each crystal of the sample. To achieve a significant shape anisotropy contribution materials with reduced the magnetocrystalline anisotropy are necessary. The magnetocrystalline anisotropy constants of the materials used in this thesis are  $K_1 = 4.1 \cdot 10^5 \text{ J/m}^3$  for hcp cobalt and  $K_1 = -4.5 \cdot 10^3 \text{ J/m}^3$  for fcc nickel. By alloying cobalt and nickel, the absolute value of the magnetocrystalline anisotropy  $K_1$  can be reduced below  $2 \cdot 10^3 \text{ J/m}^3$  between 75 % and 90 % nickel.<sup>44</sup> Therefore, the influence of the magnetocrystalline anisotropy can be tuned by the Co-Ni composition, which is published for nanowires by Vega *et al.*<sup>99</sup>

### 2.3.3 Magnetic Hysteresis

The key feature of ferromagnetic materials is that the magnetization depends not only on external conditions, but also largely on the magnetic history of the material. Therefore, it is necessary to return to defined magnetization conditions for systematic studies (complete saturation of the magnetic moments—the *saturation magnetization*  $M_S$ , which is achieved above the *saturation field*  $H_S$ ). Typically, ferromagnetic samples are characterized by recording a sweep from one saturation field to the opposite saturation field. Reaching zero field the magnetization in a ferromagnetic sample is usually not zero and is called *remanent magnetization*  $M_R$ . The magnetic field at which the magnetization averages to zero is called *coercive field*  $H_C$ . In the special case of a single irreversible jump-like reversal of the magnetization—called Barkhausen jump—the coercive field is called *switching field* as well. A full sweep from one to the opposite saturation value and back is called hysteresis loop and is used to determine the characteristic quantities mentioned above. A sketch of the magnetic behavior of a single nanowire with dominating shape anisotropy is shown in Figure 2-8. The parallel to the nanowire axis (easy axis) applied magnetic field leads to a jump-like reversal of the magnetization, while perpendicular to the nanowire axis (hard axis) higher magnetic fields ( $H_S = 2\pi M_S$ ) are necessary to turn the magnetization completely.<sup>100</sup>

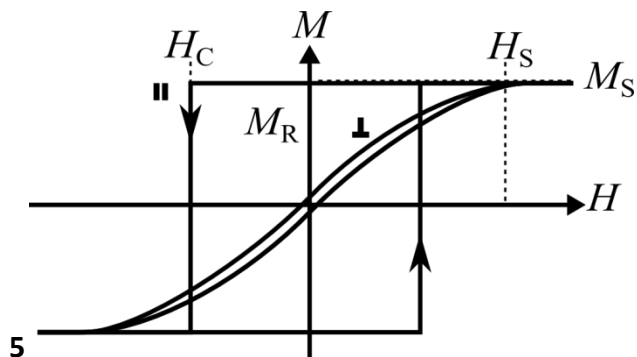
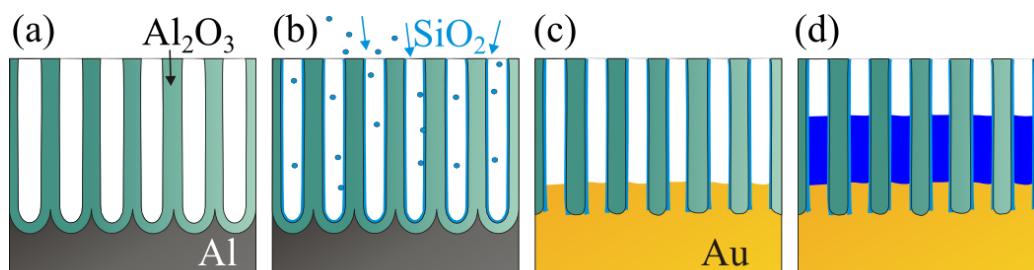


Figure 2-8 Sketch of hysteresis loops in parallel and perpendicular direction to the nanowire axis with dominating shape anisotropy of the ferromagnetic nanowire.



### 3 Nanowire Synthesis

A variety of methods is available to synthesize nanowires (NWs): filling of cracks in thin films,<sup>101</sup> vapor-liquid-solid growth from the gas phase,<sup>102</sup> and electrodeposition in templates like nanoporous aluminum oxide membranes to name a few of them. This work is focused on electrodeposited nanowires in hexagonal self-ordered anodized aluminum oxide (AAO) membranes. The advantages of AAO membranes are the variable geometric parameters and the high aspect ratio—length to width ratio—up to 1000:1.<sup>104</sup> The general procedure of the nanowire synthesis is reported in this chapter, as sketched in Figure 3-1(a-d): *Anodization*, *Atomic Layer Deposition (ALD)*, *Preparation Steps*, and *Electrodeposition*. The *Hard Anodized Aluminum Oxide Membranes* and the *Electrodeposition of Multilayers* are discussed in more detail. At last, the *Release of the Nanowires* from the membrane is explained.

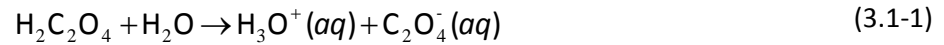


**Figure 3-1** The schematic representation of the nanowire preparation: anodized porous alumina membrane (a), ALD coating (b), opening of the backside of the pores (c), and electrodeposition inside of the pores (d).

#### 3.1 Anodization

In order to synthesize aluminum oxide membranes, a 99.9999 % aluminum sheet is electropolished in a homemade anodization cell and exposed to perchloric acid in ethanol (1:3 vol.).<sup>105</sup> Subsequently, the anodization cell is cooled down to -2 °C and an electric potential is applied between the aluminum and a platinum mesh acting as a counter electrode. The *anodization*—electrochemical oxidation—is based on two competing chemical processes. Due to the applied electric potential the dissociated ions (e.g. for oxalic acid in equation (3.1-1)) migrate through the initial aluminum oxide layer to the aluminum, which acts as the anode. Since the dissociated ions are in hydrated state, water molecules migrate through the aluminum oxide as well. The underlying aluminum is oxidized (see equation (3.1-2)) and the remaining hydrogen ions are reduced at the cathode (3.1-4). This process increases the aluminum oxide—called alumina—thickness (3.1-3), while in the second chemical process the acidic electrolyte

dissolves aluminum oxide at the metal-electrolyte interface and decreases the oxide thickness (3.1-5) constantly.<sup>106</sup>



An equilibrium thickness—proportional to the anodization voltage—is reached, because the ion migration through the oxide layer depends on the thickness of the oxide layer. At areas of thin aluminum oxide—e.g. due to local surface roughness—this process is accelerated and leads to an unordered growth of pores. After a certain anodization time at appropriate conditions, this pore growth will lead to a self-ordered hexagonal pore distribution, due to volume expansion and mechanical stress.<sup>107</sup> The common recipes for self-ordering anodization conditions and the resulting geometrical parameters are given in Table 3-1: The pore diameter  $D_p$ , the distance between two pore centers  $D_{\text{int}}$ , and the porosity  $p$ , which describes the ratio between pore surface to membrane surface and is calculated by:<sup>107</sup>

$$p = \frac{\pi}{2\sqrt{3}} \left( \frac{D_p}{D_{\text{int}}} \right)^2 \quad (3.1-6)$$

In order to synthesize membranes with straight continuous pores from the bottom to the top, a two-step anodization technique is used.<sup>108</sup> During the first anodization, the pore growth approaches the self-ordered regime. Subsequently, porous alumina is selectively dissolved at temperature around 50 °C in a solution of chromic acid ( $\text{H}_2\text{CrO}_4$ , 0.18 M) and phosphoric acid ( $\text{H}_3\text{PO}_4$ , 0.61 M) for about 12 hours. This process leads to a clean aluminum substrate with an ordered pattern of the imprint of the pores. This pattern acts as a nucleation seed for the second anodization step and the growth begins with highly-ordered pores, as shown in a cross section scheme in Figure 3-1(a).

**Table 3-1 Typical synthesis parameters of AAO membranes with self-ordered pore growth in the mild regime.**<sup>109</sup>

	<b>sulphuric acid</b>	<b>oxalic acid</b>	<b>phosphoric acid</b>
<b>concentration</b>	0.3 M	0.3 M	0.1 M
<b>potential</b>	25 V	40 V	195 V
<b>temperature</b>	6 °C – 8 °C	8 °C – 14 °C	-1 °C – 0 °C
<b>growth speed</b>	7.6 $\mu\text{m h}^{-1}$	3.5 $\mu\text{m h}^{-1}$	2 $\mu\text{m h}^{-1}$
<b>pore diameter</b>	25 nm	30 nm	160 nm
<b>interpore distance</b>	65 nm	105 nm	500 nm
<b>porosity</b>	12 %	8 %	9 %

### 3.2 Hard Anodized Aluminum Oxide Membranes

This section focuses on the deviations of the synthesis of hard-anodized nanoporous alumina membranes (HA-NAM) to the mild anodized AAO membranes. A mild anodization process at 80 V is used to form the first oxide layer at controllable current densities of around  $2 \text{ mA}\cdot\text{cm}^{-2}$ .<sup>104</sup> Then the electrolyte is replaced by a 0.3 M oxalic acid with 5 vol. % additive of ethanol—as an anti-freezing agent.<sup>110,111</sup> Due to high current densities around  $200 \text{ mA}\cdot\text{cm}^{-2}$  during the hard anodization,<sup>104</sup> the temperature has to be carefully controlled to prevent burning of the aluminum surface. Typically, the temperature is  $-1 \text{ }^\circ\text{C}$  before the anodization process, which leads to temperatures about  $3 \text{ }^\circ\text{C}$  during the hard anodization. The mild anodization voltage is swept at a rate of  $0.08 \text{ Vs}^{-1}$  to the target hard anodization potential of 140 V. The high current densities result in much faster pore growth. Vega *et al.*<sup>99</sup> and Montero *et al.*<sup>112</sup> published the analysis of the interpore distance and pore diameters. In mild anodized AAO membranes the pores size and the interpore distance increases with the anodization voltage. In hard anodized membranes the interpore distance increases linear with the anodization voltage, while the pore diameter stays almost constant between 50 nm and 60 nm. In general, narrower pores and a lower porosity of 2.2 % are the case. Using the conditions described above and additional pore widening an interpore distance of 305 nm and a pore diameter of 150 nm is achieved. These membranes are used for the synthesis of the Co-Ni nanowires mentioned in chapter 5, while the GMR nanowires described in chapter 6 are deposited in mild anodized phosphoric acid membranes.

### 3.3 Atomic Layer Deposition

Electrical transport measurements of nanostructures suffer from the oxidation of metal interfaces and surfaces. Native oxides often show insulating or semiconducting behavior and make consistent electrical transport measurements challenging. As the ratio of oxidized surface volume to volume ratio drastically increases with decreasing dimensions this can noticeably influence the magnetic behavior, for instance reduce the magnetization or cause exchange bias. The atomic layer deposition (ALD)—or atomic layer epitaxy—is capable to protect nanowires against etching during the release step and aerobic oxidation.<sup>113,114</sup> ALD is a deposition technique for thin films that offers control of the thickness down to the atomic level of the deposited material.<sup>115,116</sup> There are two main advantages of this technique compared to other deposition techniques such as *chemical vapor deposition* (CVD) or *physical vapor deposition* (PVD). The first advantage is the conformality of the coating. Complex structures with high aspect ratios and without line of sight to the source are covered without shadowing effects. Secondly, the experimental conditions are close to atmospheric pressure and down to room temperature. This makes depositions on fragile substrates possible.

The operating principle of ALD is a specially modified CVD process. It is based on the sequential and cyclic exposure of a substrate to two (sometimes three) precursor gases which react selectively and self-limiting with the substrate surface. In a first step, the substrate is exposed to the precursor A so that precursor molecules react with functional groups present on the substrate surface, until reaching a saturated state in which all available functional groups have reacted with precursor molecules. Eventually, further exposure of the substrate causes no reaction—the process is self-limiting. The premise for self-limitation is that the precursor is not reacting with itself or any of the reaction by-products. In a subsequent step, the remaining gas molecules of precursor A are removed from the reaction chamber by a nitrogen purging step. The substrate is then exposed to a second precursor B, which reacts with the molecules from the first step linked to the substrate surface. After the second self-limiting reaction step, the surface states are again equal to the initial state thus ensuring a periodic process. The reaction by-products and excess precursor molecules are removed in a subsequent nitrogen purge. Depending on the deposition material and process parameters one complete cycle deposits a 0.1 Å to 3 Å thick layer. This cycle is repeated as often as necessary to reach the desired thickness. Given that the precursor molecules can diffuse to the entire surface of the sample during the exposure time, the process is not limited by the geometry of complex samples. Therefore, ALD is ideal to coat complex nanostructures such as nanoporous alumina membranes.<sup>115,116</sup>

In this work the ALD technique is used for conformal coating of nanoporous alumina membranes with a thin (<10 nm) silicon dioxide (SiO<sub>2</sub>) layer using 3-aminopropyltriethoxysilane, H<sub>2</sub>O and O<sub>3</sub> as precursors.<sup>117</sup> The process leads to deposition of a compact layer of amorphous SiO<sub>2</sub> with a growth rate of approximately 0.07 nm per cycle. The depositions onto the alumina templates are performed in exposure/stop-mode operated at 150–200 °C on various ALD reactors. A RIE etching step is used to remove interconnections of the SiO<sub>2</sub> at the membrane surface between the pores. In addition to passivating the subsequently grown nanowires, the shell decrease agglomeration of single nanowire in the solution, due to a reduced magnetic interaction since the minimal distance between ferromagnetic nanowires is increased to 20 nm. The dimensions of the magnetic material are more precisely defined because of the absence of native oxides. While materials like nickel are chemically stable, it seems a passivating layer is necessary to synthesize single nanowires containing cobalt, copper, or iron to prevent dissolution.

### 3.4 Preparation Steps

The alumina membranes have to be prepared with a working electrode on the backside for an electrodeposition into the pores. Therefore, the remaining aluminum backside is selectively removed in a HCl and CuCl<sub>2</sub> solution until the membrane is free standing.<sup>118</sup> The aluminum barrier oxide at the pore bottom is removed by a dry etching process or a wet-chemical process in 5 wt. % phosphoric acid. The dry etching process is conducted in a *reactive ion etching* (RIE) reactor (Etchlab 200, *Sentech*), in which it is exposed to a plasma—generated from a mixture of O<sub>2</sub> and CF<sub>4</sub> at a pressure of 12 mTorr with an applied power of 250 W. This process is highly anisotropic, so that the barrier layer of the alumina is removed almost without affecting the remaining membrane. Alternatively, the membrane can be immersed for 2.5 hours in 5 wt. % phosphoric acid at 30 °C, in order to remove the alumina barrier layer at the bottom of the pores. This wet etching process is especially used for hard anodized membranes, since it is also used to widen the pores and to remove the inhomogeneities created by the initial voltage ramp. Afterwards, a sputtering process is conducted to deposit a few nanometers of gold on the backside of the membrane with a commercial metallization setup (sputter coater 108auto, *Cressington*). This sputtered gold layer is the working electrode for electroplating of a few micrometers thick gold layer at 2.4 V from a commercial gold cyanide ion based electrolyte (Auruna, *Umicore*). This process ensures that the nanopores are completely occluded from the backside of the membrane.

### 3.5 Electrodeposition

The electrodeposition is a chemical deposition technique from a liquid, called electrolyte. In this work the electrolytes consist of aqueous solutions of chlorides or sulfates of metals and contain additives as a pH buffer. During electrodeposition at sufficient negative potentials the solved metal ions are reduced by the exchange of electrons from the conductive substrate (cathode) to the ions—leading to metal deposition. At far more positive potentials, the metal atoms are again oxidized—dissolved—and the process is reversed. The equilibrium potential, with no reaction, can be expressed by the Nernst equation:<sup>119</sup>

$$E^{\text{eq}} = E^0 - \frac{RT}{nF} \ln \frac{a_{M^{n+}}}{a_M}, \quad (3.5-1)$$

in which  $E^{\text{eq}}$  denotes the half-cell reduction potential at the temperature of interest,  $E^0$  is the standard half-cell reduction potential,  $R$  is the universal gas constant,  $T$  is the absolute temperature,  $a$  is the chemical activity for the ions in the solution and the deposited atoms on the substrate,  $F$  is the Faraday constant, and  $n$  is the number of mols of electrons transferred in the reaction. Standard potentials of the metal ions of interest are shown in Table 3-2.

**Table 3-2 The standard electrode potential  $E^0$  of some species of interest with respect to a normal hydrogen electrode.**<sup>120</sup>

ion	standard potential
$\text{Fe}^{2+}$	-0.44 V
$\text{Co}^{2+}$	-0.28 V
$\text{Ni}^{2+}$	-0.26 V
$\text{Cu}^{2+}$	0.34 V
$\text{Au}^{3+}$	1.52 V

Measuring the chemical activities is not trivial, but in the case of low ion concentrations ( $<10^{-3}$  M) the chemical activity can be replaced by the ion concentration. Above this limit, which is the case in this work, it is experimentally more practical to determine the potentials from the characteristic C-V—a technique called cyclic-voltammetry. Thereby, the potential for oxidation and the reduction can be clearly distinguished as a current decrease/increase in the C-V curve. A variety of chemical reactions take place at the working electrode (cathode) and the counter electrode (anode) as well. In order to control the electrical potential independent of the reactions at the counter electrode, the deposition potential is measured with respect to a third reference point—the reference electrode. This method is generally called three-electrode setup.

The reference electrode is used at minimal electric current for sensing the applied potential. The used reference electrode is a silver-silver(I) chloride electrode (Ag/AgCl) in a saturated KCl or NaCl solution. It is in contact to the electrolyte through a membrane, which ideally allows charge transfer but prevents the mixing of the solutions. In comparisons with literature an offset of the electric potential due to a different reference electrode has to be considered.<sup>121</sup> While the electrodeposition takes place at the working electrode, the principal reaction at the counter electrode is the evolution of oxygen:



On the other hand the hydrogen ions are reduced—in competition to the metal ions—at the working electrode. At high potentials, this process can cause hydrogen evolution at the working electrode, which drastically influences the deposition conditions. The water splitting and hydrogen reduction can have a significant share of the electrical transport during the deposition and make a quantitative analysis of the deposition impossible. If hydrogen evolution is avoided, Faraday's laws predicts the amount of material  $m$  deposited during the electrodeposition process to be proportional to the total electric charge—integral over the electrical current  $I$ —flowing through the system during the time  $t$ . The proportionality factor in an electrolyte with one type of ions is given by the inverse oxidation number  $z$ .

$$m = z^{-1} \cdot \int I(t) dt \quad (3.5-3)$$

In the more complex case of electrodeposition of metal alloys, the simultaneous co-deposition of two or more metals from a single electrolyte is required. However, to deposit both ions from the solution the deposition potentials should be in close proximity to each other. If this is not the case, the potentials have to be varied by changing the ion concentrations and therefore the chemical activities—see equation (3.5-1)—or by adding suitable complexing agents which can change the deposition potential selectively. The composition of the alloy is determined by several parameters and can be changed in a certain range by varying the deposition potential or by changing the electrolyte composition.

### 3.5.1 Anomalous Co-deposition

Similar to the hydrogen evolution, other effects make a quantitative analysis of the deposition process difficult. The effect, called *anomalous co-deposition*, is often present during the deposition of transition metal alloys.<sup>122,123</sup> It describes the preferred deposition of the less noble metal over the noble metal or in other words the lower standard potential over the higher standard

potential. Although the effect is explained for some materials, no comprehensive and satisfactory theory of this effect exists. Due to the anomalous co-deposition, the deposited Co-Ni alloys show much higher Co concentrations than the electrolyte. Therefore, the deposit is analyzed and the electrolyte composition or the deposition potential is adjusted to match the preferred alloy composition.<sup>99</sup>

### 3.6 Electrodeposition of Multilayers

As described in section 2.1.3 multilayers of ferromagnetic and non-magnetic materials can achieve remarkable MR effects. The discovery of the GMR effect as well as recent record values are obtained on samples prepared by physical vapor deposition methods. During the last 20 years effort has been made in order to achieve similar results with alternative deposition techniques, which require less technological effort. In her review, Ross proposed the electrodeposition process as an affordable alternative synthesis method.<sup>124</sup> This method can indirectly control the chemical composition as well as the crystallographic properties of the multilayer, via the electrochemical deposition parameters: electrolyte composition, pH value, diffusion conditions, and deposition potential. In literature, these parameters are mostly evaluated regarding GMR magnitude in the CIP geometry, while this work is focused on the CPP geometry. The electrochemical processes in both geometries is identical, but the optimization of the GMR leads to different parameters due to a larger critical length scale in the CPP—see section 2.1.3. Therefore, a non-magnetic layer thickness of 3 nm to 5 nm in electrodeposited multilayers are preferred in the CPP geometry.<sup>125-127</sup> The remaining parameters are adopted from the CIP literature, as discussed in the following.

Bakonyi and Peter published a comprehensive review on the progress and difficulties regarding GMR thin film depositions.<sup>128</sup> The authors point out several challenges for improving the effect size in electrochemically prepared samples: control of the compositions, layer thicknesses, and homogeneity of very thin layers. Additionally, the control of the composition and the reproducibility seem challenging, due to the variety of parameters and dependencies on the fluid dynamics. In the case of multilayer deposition from a single electrolyte several composition aspects have to be considered: the amount of magnetic defects in the non-magnetic layer, the amount of non-magnetic defects in the magnetic layer, and the composition of the magnetic layer. Since Cu is nobler than Co and Ni, it can be deposited at a lower negative potential than Co and Ni ions. Therefore, magnetic defects in the Cu layer are of low concern, except at the interfaces. During the Cu pulse, the main challenge is the control of the Cu layer thickness and a homogeneous coverage, which is closely connected to a sharp interface. It is known, that de-

pending on the deposition potential at the beginning of the Cu deposition the already deposited Co-Ni alloy will be either current-less replaced by Cu ions or continuously deposited until the Cu layer is closed.<sup>128</sup> To reduce these irregularities at the interface the deposition potential is chosen carefully. The aim is to achieve the stationary conditions of the deposition as fast as possible and to avoid additional side reactions, which are indicated by higher or lower initial deposition currents. In addition, capacitive charges of the metal-electrolyte interface can create positive currents. The analysis of the Cu deposition potential leads to an optimized deposition potential around -0.61 V.<sup>129\*</sup> The deposition parameters and a micrograph of the resulting nanowires are shown in Figure 3-2(a-b). As mentioned the magnetic layer inevitable contains Cu impurities. However, for simplification it will be called Co or Co-Ni layer in the following. Experiments show that at high pH values (>3) more Cu is incorporated into the magnetic layer than at lower pH values,<sup>130-133</sup> while at lower pH values(<1) intensive hydrogen evolution prohibits compact multilayers. Both effects decrease the GMR ratio and pH values between 2 and 3 are commonly used to maximize the GMR of the electrodeposited multilayers.<sup>128</sup> Co-Ni compositions of the magnetic layer of around 50 % lead to the highest GMR effects.<sup>134</sup> This dependence is not fully understood and seems to be an optimization of several composition dependent properties that influence the GMR effect (anisotropy, saturation magnetization, and spin polarization).

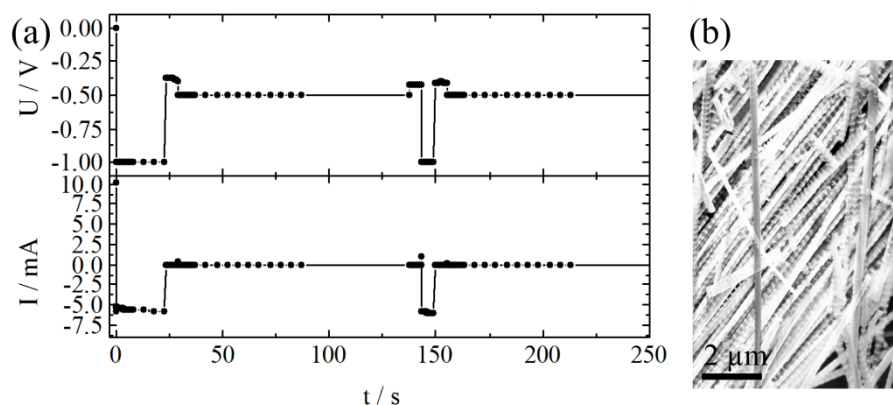


**Figure 3-2 (a) Pulsed electrodeposition parameters for Co/Cu multilayered nanowires for large (>100 nm) segments. Co is deposited at the higher voltage. (b) Co/Cu multilayered nanowires on the substrate with a segment length of 100 nm.**

\* Master's thesis of Bastian Lie, supervised during this thesis.

**Table 3-3** The electrolyte used for the electrodeposition of multilayered nanowires is a combination of 85 ml Ni-electrolyte (a) and 15 ml Co-electrolyte (b).

<u>(a) Ni-Electrolyte</u>	<u>Concentration / M</u>	<u>(b) Co-Electrolyte</u>	<u>Concentration / M</u>
CuSO <sub>4</sub>	0.01	CuSO <sub>4</sub>	0.01
Na <sub>2</sub> SO <sub>4</sub>	0.1	Na <sub>2</sub> SO <sub>4</sub>	0.1
H <sub>3</sub> BO <sub>3</sub>	0.25	H <sub>3</sub> BO <sub>3</sub>	0.25
H <sub>2</sub> NSO <sub>3</sub> H	0.25	H <sub>2</sub> NSO <sub>3</sub> H	0.25
NiSO <sub>4</sub>	0.74	CoSO <sub>4</sub>	0.74

In this work several electrolytes have been utilized. The applied recipe for the nanowire presented in chapter 6 is an 85 ml to 15 ml mixture of the electrolytes described in Table 3-3(a) and (b). Boric acid is added to the electrolyte as a buffer to keep the pH constant over the entire membrane during the deposition and to avoid the formation of complexes. The pH value of the two electrolytes is tuned by adding NaOH to 3.25 and 3.31, respectively. For each Cu layer a total charge equivalent to a segment length between 2 nm and 10 nm is deposited at a potential of -0.58 V, while magnetic layer around 12 nm are deposited at a potential of -1.5 V in order to achieve a composition of Co<sub>0.5</sub>Ni<sub>0.5</sub> in the magnetic layers according to Toth *et al.*<sup>135,\*†</sup> Lenczowski *et al.*<sup>136</sup> showed a maximum of the MR at a Cu ion concentration of 10 mM in the electrolyte and a 200 times higher Co ion concentration. It seems the Cu ion concentration, which is connected to the growth speed, is more relevant for high MR effects than the Co/Cu ion ratio. Due to low Cu concentrations, a small amount of Cu impurities in the magnetic layer is achieved. Using Faraday's law (3.5-3) the impurity concentration can be estimated by comparing the current during the Cu deposition with the current during electroplating of the magnetic layer. This estimation neglects any current-less processes like Cu replacing less noble Co or Ni atoms and secondary reactions that contribute to the overall current but not to the deposition like H<sub>2</sub> and O<sub>2</sub> evolution. Nevertheless, it can be used as an estimation to keep the Cu impurities below a set level. The drawback of low Cu concentrations is the long duration of the Cu deposition pulse due to a growth speed below 1 nm·s<sup>-1</sup>, while the growth speed of the magnetic layer is about 30 nm·s<sup>-1</sup>. Moreover, at even lower Cu concentrations ion depletion, contaminations and local pH changes due to oxygen reduction might have to be considered.<sup>128</sup> Cu does

\* The electrochemical deposition was done in the labs of the Institute for Solid State Physics and Optics in Budapest (Hungary) during a collaboration, which was funded by the DAAD.

† Due to deviating diffusion conditions in the template, the processes are not necessarily directly comparable. Nevertheless, these values are chosen as starting point.

not alloy with Co-Ni and a high Cu concentration in the magnetic layer leads to a granular structure. Liu *et al.*<sup>137</sup> reports a superparamagnetic magnetoresistance contribution in addition to the GMR effects in these structures. To avoid this, Cu impurities around 3% are favored.<sup>128,136,138</sup>

### 3.7 Release of the Nanowires

The nanowires are released from the template for individual characterization. The gold back-side electrode is removed by applying  $KI_3$ . Subsequently, a mixture of chromic acid and phosphoric acid is used to dissolve the template selectively. Afterwards, the nanowires are separated from the solution and diluted in ethanol. Three methods are available for the separation process: sedimentation using centrifugation, sedimentation using a magnet, and filtration. All of these methods have certain disadvantages. Centrifugation often bends or breaks the nanowires. Sedimentation with the help of a magnet is only possible for magnetic nanowires and the magnetized nanowires tend to agglomerate. Both of the sedimentation methods are based on replacing a part of the solution repeatedly with the final solvent until the solution is sufficiently clean from the etchant. Depending on the number of iterations, the remaining solution is more or less contaminated. Filtration of the solution is done with track-etched polymer membranes with pore size of  $0.45\ \mu\text{m}$ . A certain amount of the nanowires is lost in the pores or irretrievably sticks to the filter. Nevertheless, the filtration method usually results in the highest nanowire concentrations and is used in this work, as shown in Figure 3-3.

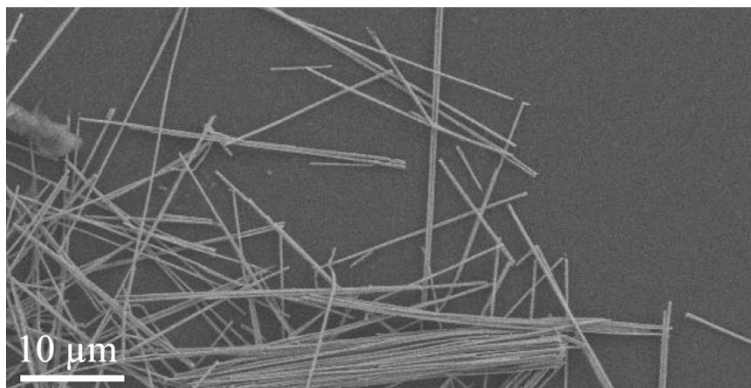


**Figure 3-3** Micrograph of Ni nanowires on a silicon substrate.



## 4 Measurement Platform

The aim of this chapter is to give an overview on the transport measurement platform, which is developed for the thermopower measurements on nanostructures presented in this thesis. A laser lithography process is established to define electrical contacts aligned to individual nanowires on a substrate. Two physical property measurement setups (VersaLab and Dynacool, *Quantum Design*) are extended to measure the magnetoresistance as well as the magnetothermopower of single nanowires in perpendicular magnetic fields up to 9 T, temperatures between 2 K and 400 K and temperature gradients up to 20 K. This chapter starts with the sections *Microscopic Contact Design*, *Macroscopic Circuit* and an overview on the *Measurement Equipment*. Then the *Measurement Routine* is explained and an overview of *Applications of the Seebeck Setup* during the last years is presented. The last chapter focuses upon the correction of *Secondary Effects* (Nernst voltages, electromagnetic induction voltage, and time-dependent drift), which is important for the following analysis.

### 4.1 Microscopic Contact Design

Electrical transport measurements on single nanowires are challenging due to their small dimensions. Surface oxidation turns in a significant experimental issue and electric potentials that are insignificant in bulk materials lead to destructive current densities. Typical nanowire measurement platforms are based on thermally isolated membranes like shown in Figure 4-1 and require high efforts in lithography and micromanipulation. An individual nanowire is placed on the pre-defined structure and measured under well-defined temperature conditions and temperature gradients up to  $0.25 \text{ K}/\mu\text{m}$ .<sup>23-25,139</sup> A significant advantage of free-standing platforms is that composition and structure of the elevated nanowire can be analyzed by microscopy techniques based on transmission (e.g. transmission electron microscopy or X-ray magnetic circular dichroism microscopy). Nevertheless, this approach requires complex substrates and challenging fabrication steps, like e-beam lithography, alignment of the nanowire, etching a thin membrane, and removing the native oxide to achieve ohmic contacts. Depending on the sample material, the latter can be an impossible challenge. A more suited approach is developed in this thesis. The oxide of the nanowire is in-situ removed and the micro device is subsequently defined onto the nanowire, which is situated on the substrate. For this reason the measurement structure published by Shapira *et al.*<sup>16</sup> is modified to study the thermoelectric effects of individual nanowires under the influence of applied magnetic fields (see Figure 4-2). Temperature gra-

dients of  $3 \text{ K}/\mu\text{m}$  can be applied with this setup. The temperature profile of the resistance thermometers is simulated (*COMSOL Multiphysics*) to understand the behavior of different geometries and optimize the electrical contact structure, as shown in Figure 4-2(c). The electrical contact alignment, heater size, and thermometer size are adjusted to ensure a smooth temperature profile within the thermometer and improve the accordance to the nanowire temperature. The structure is simulated in collaboration with bachelor and master students, as described in their theses.<sup>140-142</sup>

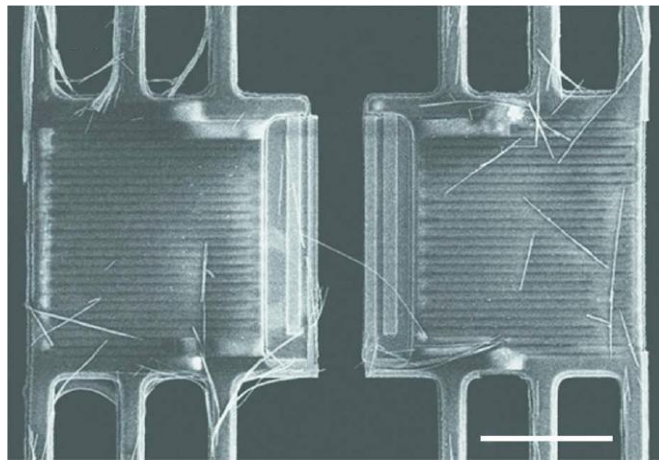


**Figure 4-1** State of the art device published by Mavrokefalos *et al.*<sup>26</sup> consisting of two free-standing platforms, which can be individually heated. The temperature is measured on both ends of the elevated nanowire. The scale bar is  $10 \mu\text{m}$ .

The nanowires with silicon dioxide coating are dispersed in ethanol and subsequently deposited on a glass substrate with  $150 \mu\text{m}$  thickness. A lift-off resist (LOR-3B at 2000 rpm for 45 s, *Micro Chem*) and a positive photoresist (ma-P 1205 at 3500 rpm for 30 s, *micro resist technology*) are applied with a spin coater and baked on a hot plate for 250 s at  $180^\circ\text{C}$  and 30 s at  $100^\circ\text{C}$ , respectively (Figure 4-3(a)). Using a laser writer ( $\mu\text{PG 101}$ , *Heidelberg Instruments*), the photoresist is exposed and subsequently developed for about 40 s. The photoresist thickness is chosen to be about 420 nm and the LOR around 210 nm, enough to cover nanowires with diameters of 180 nm in the LOR layer and to deposit the contact material without interconnects to the photoresist. The exposed photoresist is developed, while the lift-off resist that gets into contact with the developer is dissolved continuously during the process. An undercut is created to achieve sufficient lift-off conditions, as shown in Figure 4-4. Prior to the metallization an in-situ radio-frequency argon sputter etching step removes the  $\text{SiO}_2$  shell and surface oxides of the nanowire in order to achieve low resistance ohmic contacts (Figure 4-3(e-d)).

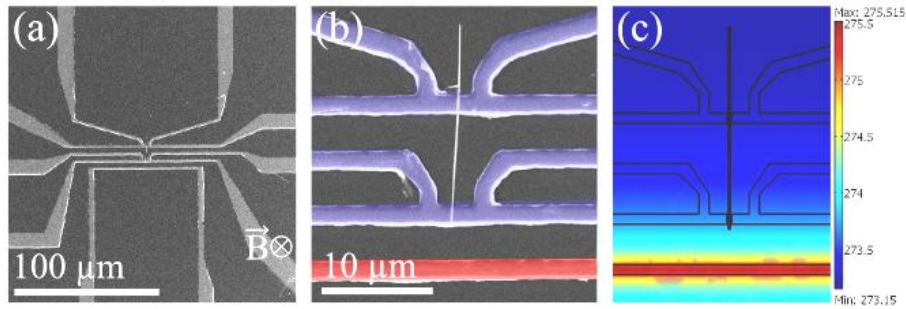


**Figure 4-2(a)** Micrograph of the Seebeck measurement structure. **(b)** Magnification of the structure with the heating wire (red) and a nickel nanowire (white) between two thermometers (blue). **(c)** Finite element analysis simulation (COMSOL) of Joule heating in the microheater and the resulting temperature profile.

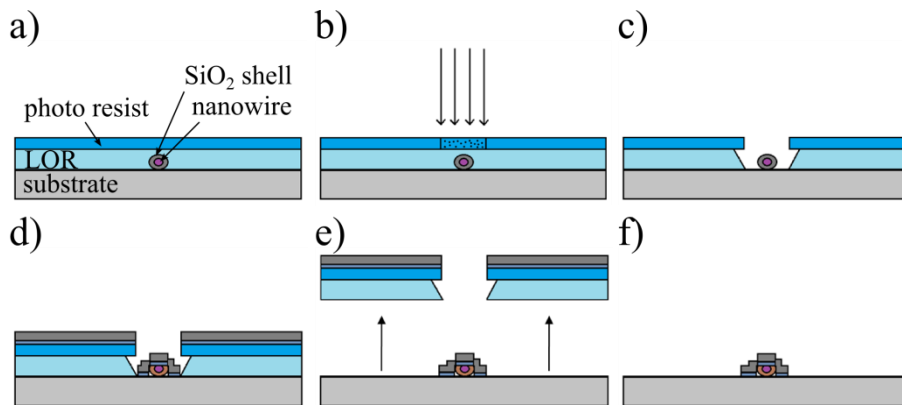


**Figure 4-3** Step-wise description of the lithographic process: spin coating of the two resists (a), the exposure (b), the development (c) with undercut structure, the sputter etching and metallization (d), the lift-off process (e), and the electrically contacted single nanowire (f).

The electrical contacts consist of a few nanometers adhesive titanium and a 60 nm thick platinum layer or alternatively a combination of aluminum and gold, which are deposited on the developed photoresist structure before the lift-off process in the Remover 1165 (*Shipley*). A scanning electron microscope micrograph of a typical device for thermoelectric characterization of a single nanowire is shown in Figure 4-2(a) and (b). The microheater is located perpendicular to the nanowire. Two resistance thermometers are placed at a distance of 8  $\mu\text{m}$  along the nanowire and serve for three purposes: probing the temperature difference  $\Delta T$  and measuring both the resulting thermovoltage  $U_{\text{thermo}}$  between the hot and the cold contact of the nanowire and the electrical conductivity  $\sigma$ . By measuring these three values, the Seebeck coefficient  $S = -U_{\text{thermo}}/\Delta T$  and the power factor  $\text{PF} = S^2\sigma$  can be calculated simultaneously.

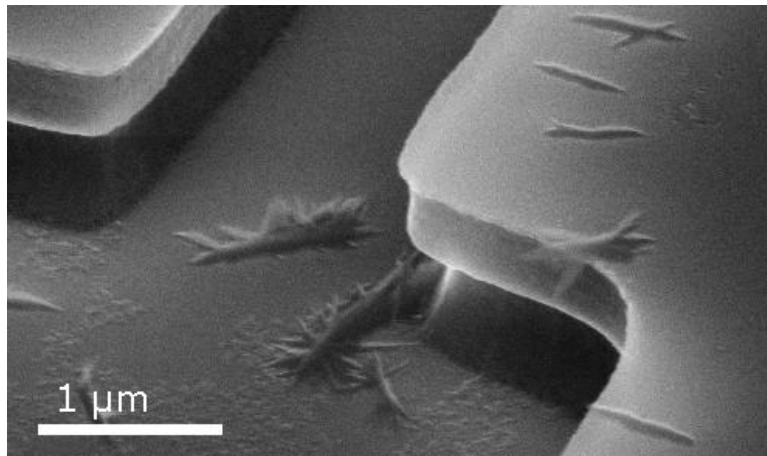


**Figure 4-4** Micrograph of a developed microstructure with undercut structure due to the double layer of photoresist and lift-off resist comparable to the sketch in Figure 4-3(c).

## 4.2 Macroscopic Circuit

Electrical contacts are lithographically attached to the nanowires on the glass substrate, which is then placed on the VersaLab sample holder for electrical measurements. For a good thermal and mechanical connection to the sample holder up to 400 K, silver paste is used as a glue. By this method, the sample is removable after the measurement without breaking the thin glass substrate. The wire bonding technique is used to connect the microscopic electrical contact structure to the macroscopic electrical contacts of the sample holder. For this purpose, a 20 μm thin aluminum bonding wire is pressed and ultrasonically welded onto the contact material. The electrical contacts of the microstructure are short-circuit to prevent discharges, due to different potential of the nanowire and the wire bonding setup. The short-circuiting should reduce the electrical current during the discharge by the factor of  $R_{NW}/R_{shortcut}$ , which is about 100. Additional 1 kΩ resistances in series with the nanowire can increase this factor to about 2000. Since four electrical contacts are connected to each nanowire's end, this protection is effectively reduced by a factor of four. The schematic of a typical 4-point resistance measurement circuit with protective resistances and switches to shorten the electrical contacts is shown in Figure 4-5. Due to these precautions, electronic discharges cause no problems in this setup.

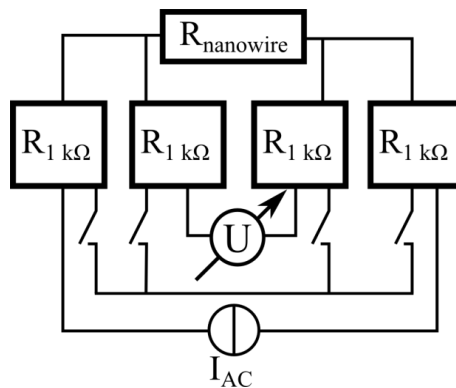


**Figure 4-5 Schematic of the electronic circuit of a 4-point resistance measurement with 1 kΩ protective resistances and switches to shortcut all connections to the nanowire.**

### 4.3 Measurement Equipment

In this section, the measurement properties and the electrical equipment used in the Seebeck measurement setup are described. All cables are shielded and the shielding is interconnected on floating potential. All instruments work on floating potentials as well. Thus, the setup should be independent of external influences.

#### Microheater

To create the temperature gradient along the nanowire, a few milliwatts are applied by the voltage-current source E3644A (*Agilent*) to the microheater. The Joule heating creates temperature differences up to 20 K along the nanowire. By measuring the resistance of the heater, the heater temperature is estimated to reach about 700 K at a current of 10 mA and the cryostat RT, as shown in Figure 4-6(a). In this experiment, the hot thermometer serves as the heater. If the substrate is homogeneous, the ratio between the resulting temperature difference  $\Delta T = T_{\text{HOT}} - T_{\text{COLD}}$  and the rise of the average temperature  $\bar{T} = (T_{\text{HOT}} + T_{\text{COLD}})/2$  is constant and depends only on the geometry. In the case of Joule heating in the hot thermometer  $T_1$  this ratio is 1, while in the geometry of the Seebeck measurement structure (separated microheater and thermometer) this ratio is about 33 %, as shown in Figure 4-6(b). This behavior has been analyzed during the master's thesis of Ann-Kathrin Michel.<sup>141</sup>

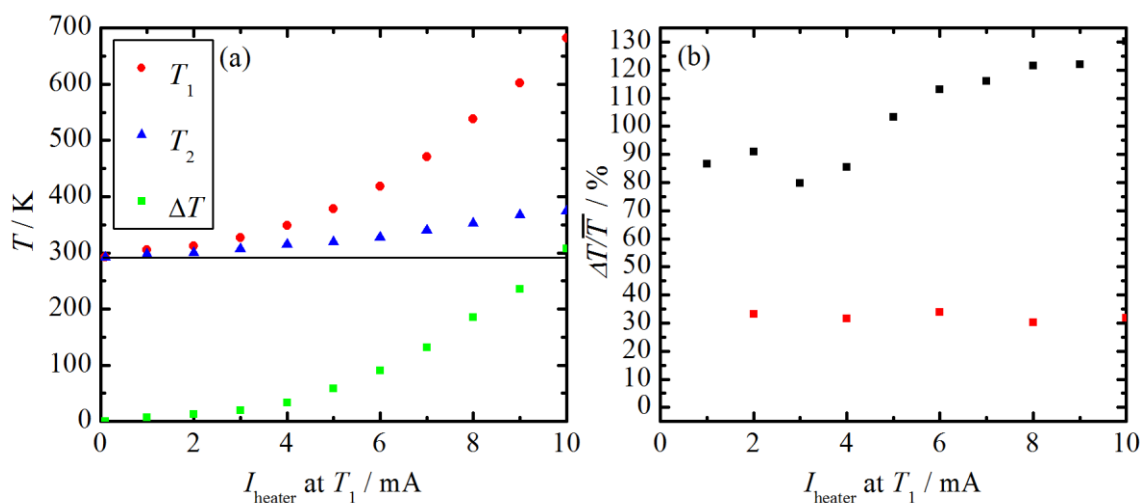


**Figure 4-6 (a) Temperature behavior of the heater ( $T_1$ ), the cold thermometer ( $T_2$ ) and the temperature difference  $\Delta T$  dependent on the heater current. (b) Heating characteristic—temperature difference normalized by the average temperature—of the measurement geometry used in (a) (black) and a typical Seebeck measurement device (red).**

#### Temperature Difference

The temperature difference is determined by measuring the resistance of two resistance thermometers. The ac resistance is measured at 128 Hz and 189 Hz by the lock-in amplifier of the electronic transport option using a feedback controlled alternating current source with amplitude of 10  $\mu\text{A}$ . The measured values are calibrated against the cryostat temperature and the temperature difference is calculated.

#### Thermovoltage

The thermovoltage is measured by a 2182A nanovoltmeter (*Keithley*) with an input impedance of  $>10\text{ G}\Omega$  and corrected by the voltage offset at zero heat voltage, which usually is in the range of 1  $\mu\text{V}$ . The Keithley nanovoltmeter is set to the lowest range of 10 mV and used in different measurement modes: fast single shot measurements used for sweeps and averaged measurements with higher precision as well as statistical error values.

#### Nanowire Resistance

The resistance measurements are performed with a feedback controlled alternating current source at a constant current of 10  $\mu\text{A}$  by applying the lock-in technique with the electronic transport option of the cryostat. Due to the use of the four-probe technique, only the nanowire resistance with a negligible contribution of the contact resistance is measured. The values for

the nanowire dimensions are subsequently determined by scanning electron microscopy (SEM) and the electrical conductivity is calculated using  $\sigma=4l/\pi d^2 U$  with a typical measurement length of  $l \approx 8 \mu\text{m}$  and the nanowire diameter of  $d \approx 200 \text{ nm}$ .

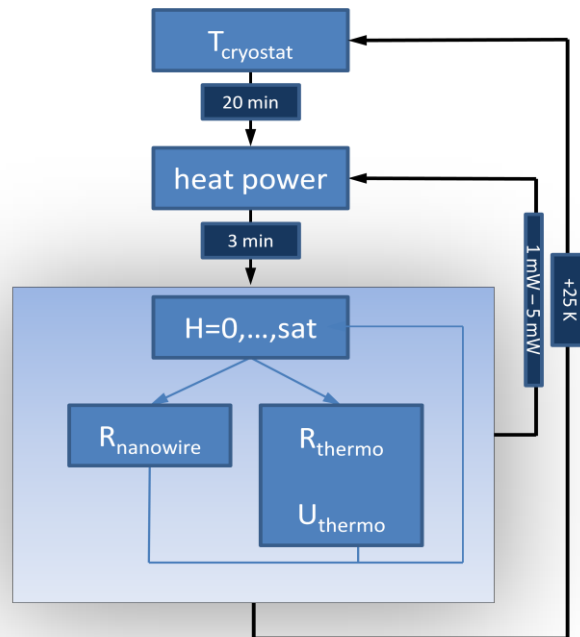


**Figure 4-7** Flow chart of the iterative measurement procedure to measure either the thermovoltage and the temperature difference or the resistance of the nanowire.

#### 4.4 Measurement Routine

During a full measurement cycle the cryostat temperature  $T_{\text{cryostat}}$  is changed stepwise between 50 K and 400 K. At each increment, electric powers of about 1 mW, 2 mW and 5 mW are applied to the heater, as displayed in Figure 4-7. The software, which is used to control the measurement parameters, is described in the appendix. To probe the temperature difference, the ac resistance of both thermometers is measured and calibrated against  $T_{\text{cryostat}}$  at zero heat power. Additionally, either the resistance or the thermovoltage of the nanowire is measured in thermal equilibrium, which is necessary to reduce the noise level. A waiting time of up to 20 minutes is necessary for stable temperatures of the electrical connections in the cryostat and a constant thermovoltage offset, as shown in Figure 4-8. Additional waiting times are implemented at each heating power to reach equilibrium conditions, as shown Figure 4-9.

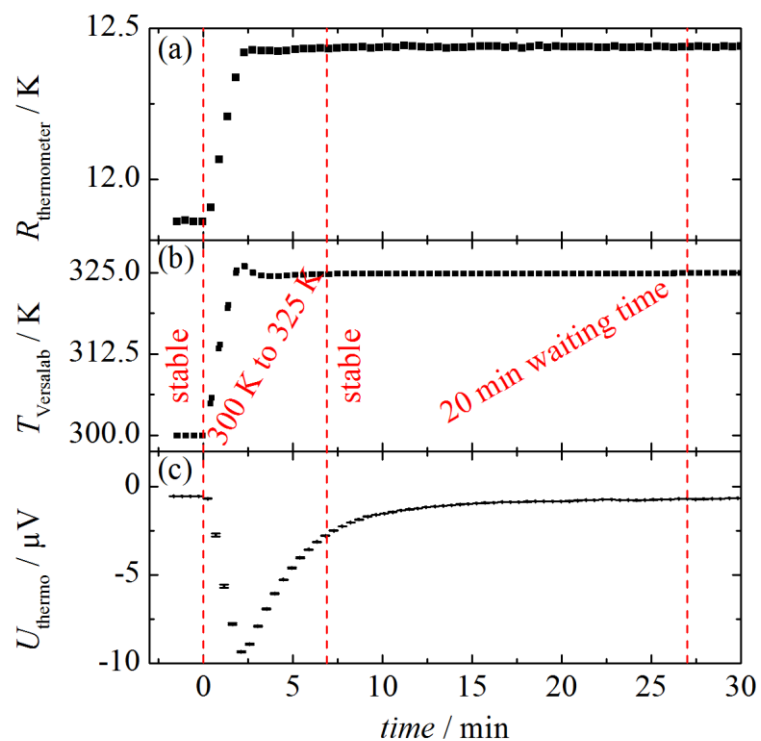


**Figure 4-8** Time depended behavior of the VersaLab cryostat during a temperature approach from 300 K to 325 K at a rate of 20 K/min. The resistance of the hot resistance thermometer is shown in (a) with a similar behavior as the cryostat base temperature displayed in (b). The thermal voltage (c) shows strong fluctuations after the cryostat base temperature is in equilibrium and considered as stable by the VersaLab, which is due to the longer time scale necessary for the system to reach equilibrium.

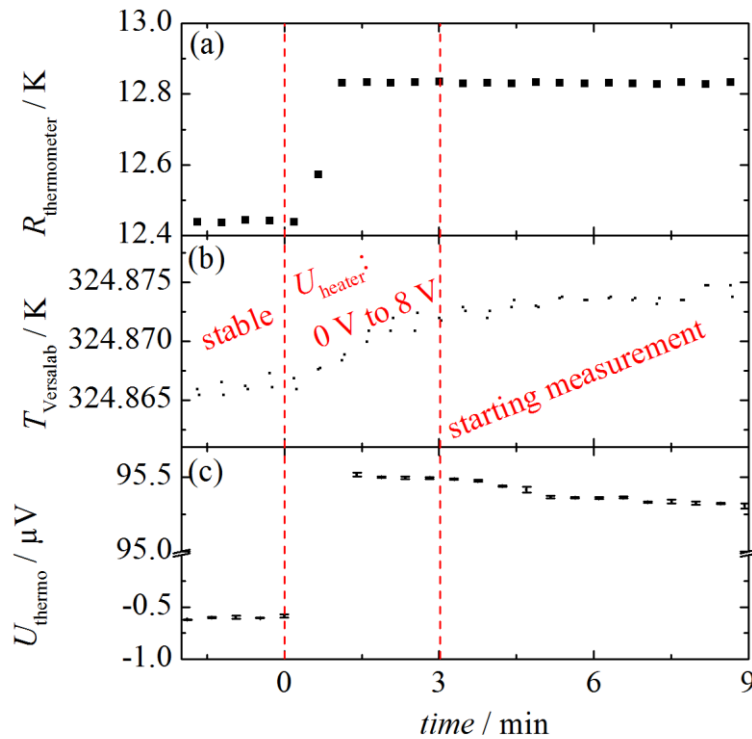


**Figure 4-9** Time depended behavior of the resistance thermometer close to the heater (a), the cryostat base temperature (b) and the thermovoltage (c) during activation of a 8 V heat voltage in the micro heater, which roughly corresponds to 3 mW heater power. The scale in the stable state after 1.5 minutes is magnified to shown the small thermopower decrease.

## 4.5 Applications of the Seebeck Setup

This section will give an overview of the applications of the Seebeck measurement setup by summarizing already realized and published experiments. Two different measurement structures are used: The nanowire and thin film lithographic contact structure—shown in Figure 4-10(a) and (b). The first measurements with this setup are performed on electrochemically synthesized  $\text{Bi}_2\text{Te}_3$  nanowires. The results are shown in Figure 4-11. The synthesis was conducted by *William Töllner*,<sup>143</sup> while the measurements results are described in the Bachelor's thesis of *Jan G. Gluschke*.<sup>142</sup> The influence of annealing in a helium atmosphere is in-situ studied on ternary  $\text{Bi}_2\text{Te}_3$ -based nanowires—displayed in the same figure—and published by *Svenja Bäßler et al.*<sup>144</sup> In these electrochemically synthesized materials annealing at moderate temperatures leads to significant changes, which increase or decrease the thermoelectric properties depend-

ing on the materials. A similar annealing study is conducted in cooperation with *Sonja Heiderich*<sup>145</sup> on electrochemically synthesized  $\text{Bi}_{0.92}\text{Sb}_{0.08}$  nanowires. In addition, gate voltage dependent measurements on gas-phase synthesized  $\text{Fe}_3\text{O}_4$  nanowires are shown in Figure 4-12(a), as published by *Johannes Gooth et al.*<sup>146,147</sup> The Verwey transition in these samples is detected via Seebeck coefficient measurements, as shown in Figure 4-12(b). Currently, *Bacel Hamdou et al.* investigates single crystalline BiSbTe nanowires—grown with the vapor-liquid-solid method—temperature and magnetic field dependent with quantum effects of surface states in the electrical conductivity and the Seebeck coefficient. It seems these effects are pronounced towards higher temperatures in the thermovoltage compared to the electrical conductivity, which can be utilized to study the effects at higher temperatures.

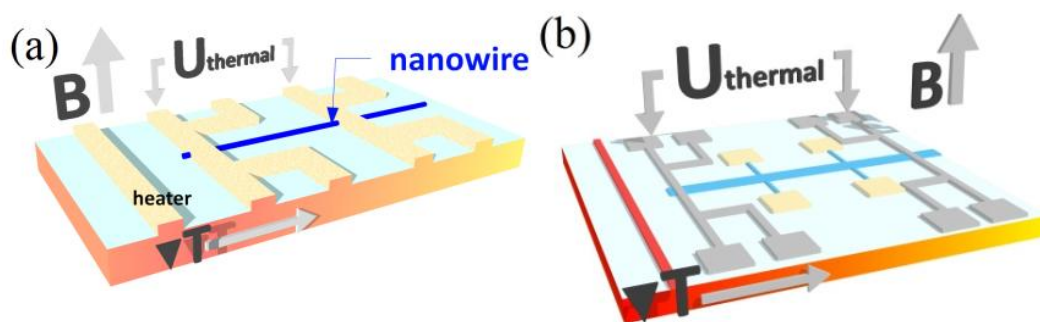


Figure 4-10 Electrical contact design for nanowire (a) and thin film (b) measurements.

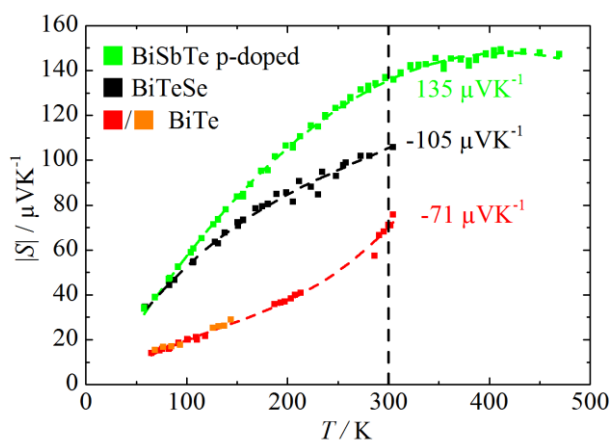
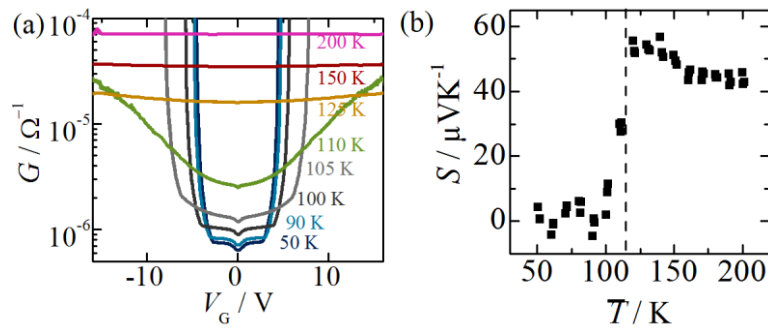


Figure 4-11 Seebeck coefficients of BiTe, BiSbTe and BiTeSe nanowires.<sup>142,144</sup>



**Figure 4-12 (a) Temperature and gate voltage dependent conductance measurements of  $\text{Fe}_2\text{O}_3$  nanowires and (b) temperature dependent Seebeck coefficient measurements showing a typical Verwey transition at 115 K.**<sup>146,147</sup>

The lithographic contact design for thin films is used for measurements on ALD deposited SbTe films. *Sebastian Zastrow et al.*<sup>148</sup> published the Seebeck coefficients, electrical conductivities, and Hall coefficients of these samples. The combination of these three properties is necessary to characterize semiconductors without distinct majority carriers. Recently, a similar work is conducted on ALD  $\text{Bi}_2\text{Te}_3$  thin films, which are deposited at different temperatures resulting in varying crystal sizes. In this publication of *Changdeuck Bae et al.*<sup>149</sup> the variation of electrical conductivity and Seebeck coefficient due to changes of lattice defects and the type of defect activation is analyzed. In cooperation with the *Prof. Oepen's* group of Universität Hamburg the thermopower of Co/Pt multilayers in different magnetic fields is measured. These thin film samples display a novel interface magnetoresistance,<sup>150,151</sup> which influences the thermopower. By relating thermopower and resistance, new information about the mechanism behind the interface magnetoresistance is gained.

The Seebeck measurement setup is currently extended by adding a groove below the nanowire, as shown in Figure 4-13. The thermal coupling between substrate and sample is removed and the thermal conductivity of the nanowire can be measured using either the so-called 3 $\omega$  method or a steady state method, called Völklein methode.<sup>23,152</sup> The nanowires are aligned on already etched grooves or the grooves are etched below the nanowires. Measuring the thermal conductivity is necessary to test the Wiedemann-Franz law<sup>76,77</sup> and to calculate the efficiency of the material in thermoelectric generators.<sup>78</sup> The temperature gradient in elevated nanowire is linear, which makes precise characterization of the temperature difference in certain segments of the nanowire possible. For spin valve structures and tunnel barriers, this precisely defined temperature profile is useful to calculate the Seebeck coefficients. Up to now, most publications use simulations to predict temperature differences of complex nanostructures,<sup>17-20</sup> which should be carefully interpreted due to varying material parameters.

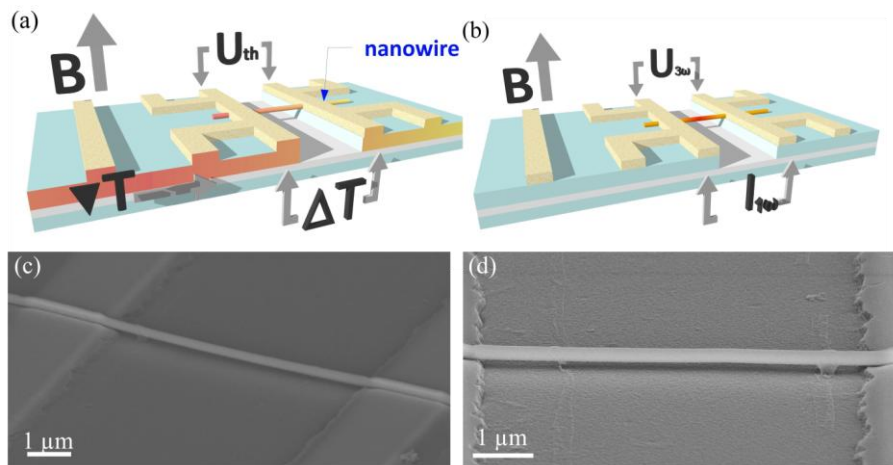


**Figure 4-13** Further improvement by adding a groove below the nanowire to enable thermopower (a) and thermal conductivity (b) measurements on the same sample. SEM micrographs of the etched groove with nanowire on a glass substrate are shown in (c-d).

#### 4.6 Secondary Effects

Thermovoltages are typically in the  $\mu\text{V}$ -range. Additional voltage sources have to be considered, due to temperature gradients and magnetic fields in the setup. To understand the various voltage sources, a  $\text{Co}_{0.39}\text{Ni}_{0.61}$  nanowire is studied under the influence of heater voltages up to 18 V ( $\Delta T$  of 22 K) at 50 K, as shown in Figure 4-14(a). The heater increases the average nanowire temperature  $\bar{T}$  from 50 K to 120 K. As specified by the Mott formula (2.2-4) the thermopower  $S$  depends linearly on the temperature  $\bar{T}$ , which is evident from Figure 4-14(b). Therefore, the non-linearity of  $U_{\text{thermo}}$  against  $\Delta T$  can be explained by the increase of  $S$  with  $\bar{T}$ , while the non-monotonic behavior for small  $\Delta T$  indicates significant uncertainties for small measurement values. Figure 4-15 shows a typical magneto-thermoelectric power curve of a Ni nanowire at RT. In this magnification, an asymmetry is obvious, which is caused by different secondary effects: *electromagnetic induction*, *Nernst effect* and a *time dependent drift*. By correcting these effects, the thermovoltage curve can be recovered, as shown in grey in Figure 4-15. In order to quantify the distortions four different saturation values  $U_{\text{sat}1}$  to  $U_{\text{sat}4}$  are defined. One distortion is the difference between the upward and downward curve. The magnitude of the difference depends on the sweeping rate  $r$  of the magnetic field and is independent of the heater voltage as shown in Figure 4-16.

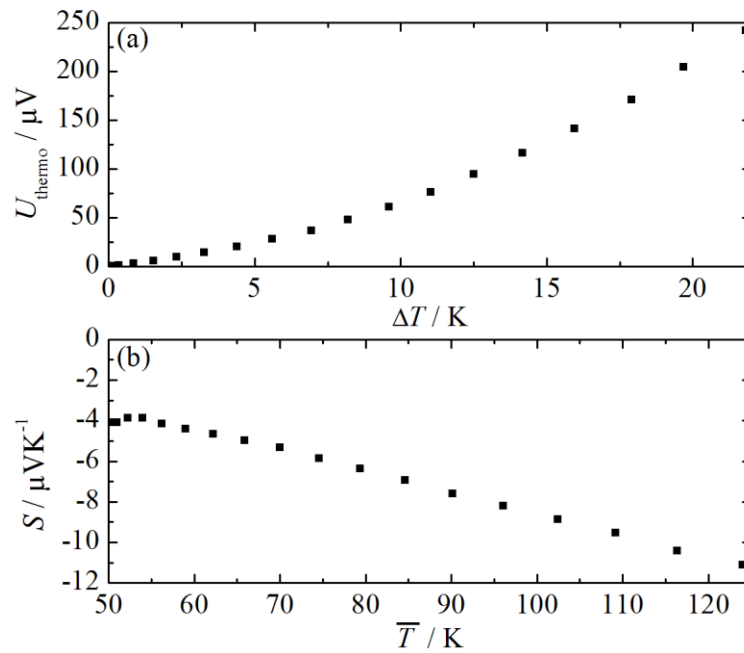


**Figure 4-14(a)** Thermovoltage of a  $\text{Co}_{0.39}\text{Ni}_{0.61}$  nanowire at 50 K as a function of the temperature difference shows an increasing slope at higher temperature differences. **(b)** The Seebeck coefficient  $S$ —the slope of (a)—decreases linear with temperature.

This dependence on the change of the magnetic flux is known from electromagnetic induction given by Faraday's law:<sup>153</sup>

$$U_{\text{induction}} = n \cdot \int \frac{d\vec{B}}{dt} d\vec{A}. \quad (4.6-1)$$

It is quantified by the difference between both saturation values on the right hand side:

$$U_{\text{induction}} = (U_{\text{sat4}} - U_{\text{sat3}}) / 2. \quad (4.6-2)$$

At a sweeping rate of  $100 \text{ Oes}^{-1}$  this induction voltage has an average value of  $U_{\text{induction}} = (0.2625 \pm 0.0042) \mu\text{V}$ . An effect is noticeable in the saturation region, which is linear with the magnetic field:

$$dU_{\text{nemst}} / dH = (U_{\text{sat3}} - U_{\text{sat1}} - U_{\text{sat2}} + U_{\text{sat4}}) / (2H_{\text{sat}}). \quad (4.6-3)$$

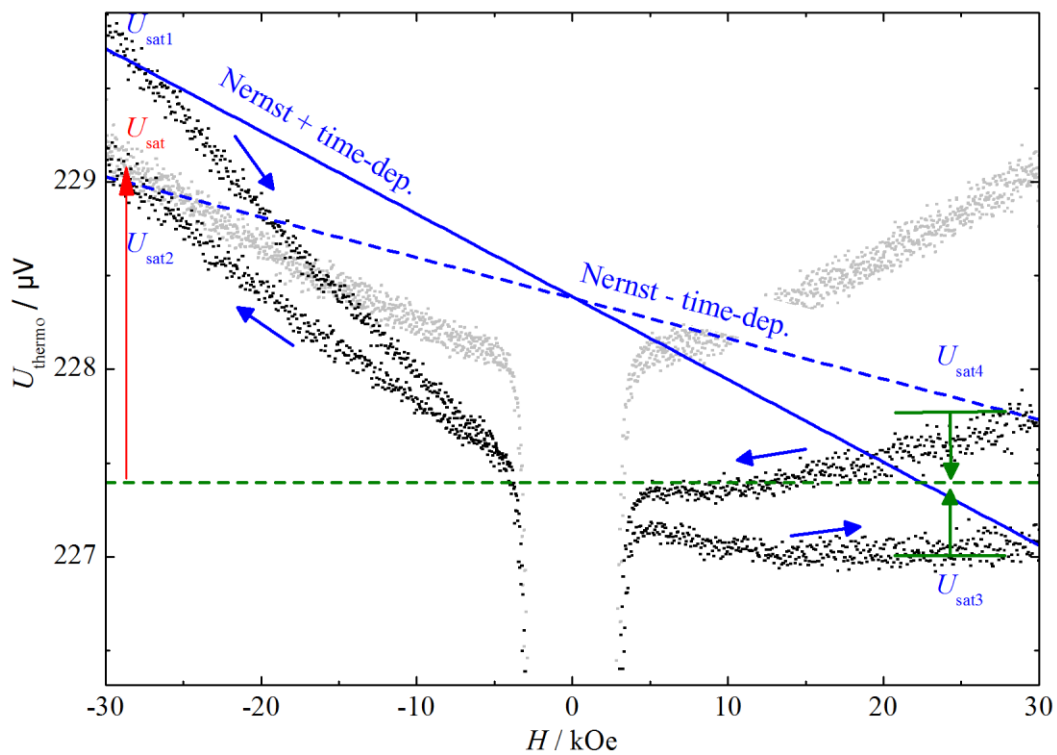


**Figure 4-15** Thermovoltage of a Ni nanowire at an average temperature of 362 K and a temperature difference of 31 K. The as measured data is displayed in black, while the corrected data—without secondary effects—is displayed in gray.

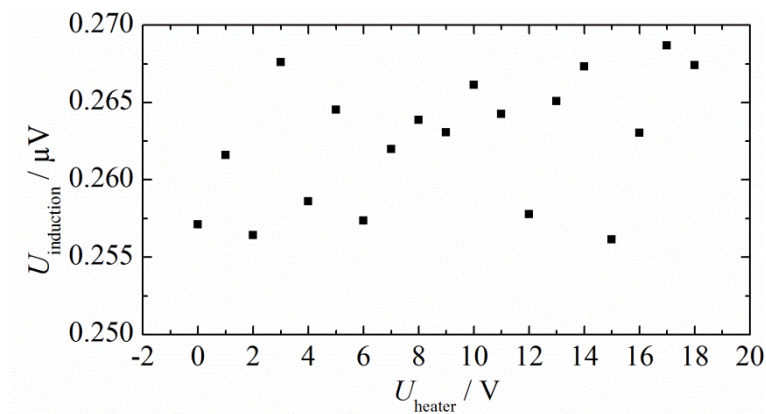


**Figure 4-16** Induction voltage at a sweeping rate of 100 Oe/s.

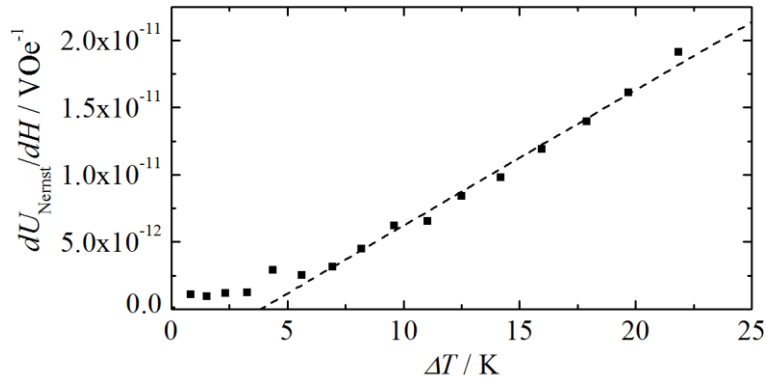


**Figure 4-17 The Nernst effect of the electrical contact structure determined in the saturation region.**

This voltage is proportional to  $H$  and  $\Delta T$ , as shown in Figure 4-17. It can be concluded that this voltage arises from the Nernst effect—also called Ettingshausen-Nernst effect—given by:<sup>154</sup>

$$U_{\text{nemst},y} = N\Delta T_x \frac{y}{x} B_z. \quad (4.6-4)$$

The Nernst effect depends linearly on a temperature gradient as the Hall effect depends linearly on an electrical current, as shown Appendix (6.4-1) to (6.4-4). A Nernst voltage of  $U_{\text{nemst},y}$  arises due to a perpendicular temperature difference  $\Delta T_x$  in a perpendicular magnetic field  $B_z$ , as sketched in Appendix: Figure 7-5. Due to the measurement geometry, the electrical contact structure contributes to the Nernst voltage dominantly. The geometry of the electrical contact in the direction of  $U_{\text{nemst},y}$  and  $\Delta T_x$  is described by  $y$  and  $x$ , respectively. By keeping the geometry and  $\Delta T_x$  unchanged and varying the contact material from Pt to Au, a similar Nernst voltage with opposite sign is expected from bulk literature values ( $N_{\text{Au}} = -15.8 \text{ nV(TK)}^{-1}$  and  $N_{\text{Pt}} = 13 \text{ nV(TK)}^{-1}$  at RT)<sup>155</sup>. From simulations it can be assumed that the gradient in the electrical contacts scales linear with the temperature difference between the thermometers  $\Delta T$ . Therefore, the relative values can be compared as follows:

$$\frac{N_{\text{Au}}}{N_{\text{Pt}}} = \frac{dU_{\text{Au,measured}}/dH}{dU_{\text{Pt,measured}}/dH} \frac{\Delta T_{\text{Pt}}}{\Delta T_{\text{Au}}}. \quad (4.6-5)$$

Indeed the ratio of the Nernst coefficients determined by the measurement of -1.44 agrees well with the literature ratio of -1.22. The slope  $dU_{\text{Nernst}}/dH$  in Figure 4-17 scales linear with  $\Delta T$  with an offset on the x-axis. This is reasonable, considering that for small  $\Delta T$  any temperature gradient in the electrical contact is diminished due to the high thermal conductivity and no Nernst effect is measured.

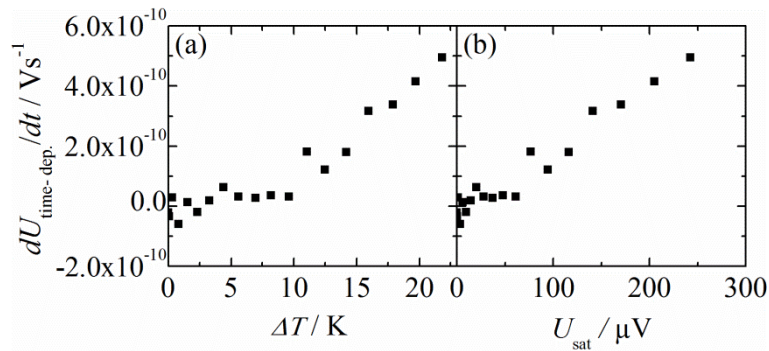


**Figure 4-18 Linear slope of the time-dependant drift of the thermovoltage. The drift is linear to the thermovoltage rather than to the temperature difference.**

The duration of a typical magnetic field sweep is ten to twenty minutes. During this time the measured thermovoltage shows a slight offset between start and end magnitude, which is often explainable by a time-dependent drift. Since the sweeping rate  $r$  will change sign during the hysteresis the time-dependent part of the measured voltage will change sign:

$$dU_{\text{time-dep}}/dt = (U_{\text{sat3}} - U_{\text{sat1}} + U_{\text{sat2}} - U_{\text{sat4}})/(2H_{\text{sat}}) \cdot r. \quad (4.6-6)$$

The assumption of a linear behavior after the initial heating phase is verified by measurements similar to Figure 4-9. Comparing Figure 4-18(a) and (b) it seems that the drift depends rather on the size of the thermovoltage than on the applied heater power represented by  $\Delta T$ . The influence of two competing mechanisms can explain the observed behavior. A slow heating of the overall cryostat temperature noticeable in Figure 4-9, due to the additionally applied heat leads to an increased  $|S|$  and an increase of  $|U_{\text{thermo}}|$ . And a decrease of  $\Delta T$ , due to the increase of the overall cryostat temperature, leads to a decrease of  $|U_{\text{thermo}}|$ . It seems that at low temperatures the first mechanism dominates and  $|U_{\text{thermo}}|$  increases with time, while at RT the latter dominates and  $|U_{\text{thermo}}|$  decreases with time.

$$U_{\text{sat}} = U_{\text{sat1}} - U_{\text{nemst, sat}} + U_{\text{induction}} \quad (4.6-7)$$

The error of the saturation value due to the influence of the Nernst and the time-dependent effect is below 1 %. At first glance, this seems negligible, but in fact, this correction is crucial for comparisons of  $S$  and  $R$  in the following chapters.\*

---

\* Due to the small secondary voltages, the assumption of additive voltages is accurate. Otherwise, a combination of the Nordheim-Gorter rule and the two-band model has to be carefully applied (see section 2.2).

## 5 Thermoelectric Transport in Anisotropic Magnetoresistance Nanowires

The Mott formula<sup>8</sup> describes the diffusive part of the thermopower and also predicts a direct relationship between  $S$  and  $\sigma$  in ferromagnetic materials with negligible non-diffusive contributions. In the contrary, the experimental results do not always obey these clear predictions and a more complicated relationship is often presumed. Avery *et al.*<sup>156</sup> states that “it is tempting to explain the reduction in thermopower with changing resistivity using a constant offset or simple scaling factor, but the observed differences in both thermopower magnitude and slope illustrate more complicated relationship between the two quantities.” Further, they suggest additional measurements on numerous samples as well as a broader range of temperatures to understand the dependencies. Despite several similar publications, this has not been fully accomplished until now.<sup>13,16,38</sup> In this chapter, the dependencies are investigated as suggested on single Co-Ni alloy nanowires of different compositions. The material system shows large absolute thermopowers ( $<-14.5 \mu\text{VK}^{-1}$ ) and large AMR effects as high as 6.5 % compared to other ferromagnetic alloys at RT.<sup>27,28</sup> Therefore, this alloy is an ideal candidate to investigate the magneto-thermopower under the influence of the magnetic field. Additionally, the high aspect ratio—length to width ratio—of the nanowires results in an uniaxial shape anisotropy, as discussed earlier in section 2.3.2. This results in a defined magnetization behavior and lower saturation fields ( $H_s^\perp=2\pi\cdot M_s$ ) in comparison to thin film samples ( $H_s^\perp=4\pi\cdot M_s$ ), when the magnetic field is applied perpendicular to the easy axis of the magnetization. In an earlier work on the magnetization behavior of these nanowires, it was observed that the shape anisotropy is distorted by the magnetocrystalline anisotropy with increasing Co content.<sup>99</sup> The main reason is the transition of the crystalline structure from fcc for Ni-rich (>50 %) nanowires to hcp phase for the Co-rich ones. Therefore, the magneto transport properties are studied composition dependent, but also depending on the transition from dominating shape anisotropy to dominating magnetocrystalline anisotropy. The average composition of the samples is determined by using energy dispersive X-ray analysis (EDX) within a scanning electron microscope (SEM, ZEISS SIGMA using a field emission cathode). The analysis is carried out on the cross section of each AAO membrane. An error of around 5 % can be expected by this method. Additionally, the composition of individual nanowires is determined by EDX within a transmission electron microscope (TEM, JEOL JEM 2100 at the University of Oviedo), as shown in Appendix: Figure 7-4(a-b), and the homogeneity of the deposition along and across the nanowires axis is confirmed. The composition measured by TEM-EDX deviated from the average SEM-EDX data by 5 %, which is with-

in the precision of the measurement, but also demonstrates statistical deviation of individual nanowires from the average. Due to experimental reasons, the composition of the particular measured nanowire cannot be determined by either method. Therefore, the average SEM-EDX values are assumed.

In the first two sections of this chapter, measurement results of the *magnetoresistance* and the *magneto-thermopower* on alloy nanowires in magnetic fields are presented as a function of the temperature. The results are hereby put into context with each other in the section “*The Mott formula— $S$  vs.  $R^{-1}$* ”. In the following section “*Permalloy nanowires*”, basic results on a second material system are presented. This chapter is finalized with the *conclusions on alloy nanowires*.

## 5.1 Magnetoresistance

As a first characterization of the thermoelectric transport properties in the nanowires, the electrical resistivity  $\rho$  is determined. A typical nanowire with the electrical contact structure is shown in Figure 4-2(a-b). The geometry of the nanowire is determined by scanning electron microscopy. The electrical resistivities at RT are calculated to be 13.2  $\mu\Omega\text{cm}$  for Ni, 21.7  $\mu\Omega\text{cm}$  for  $\text{Co}_{0.24}\text{Ni}_{0.76}$ , 19.7  $\mu\Omega\text{cm}$  for  $\text{Co}_{0.39}\text{Ni}_{0.61}$  and 19.4  $\mu\Omega\text{cm}$  for  $\text{Co}_{0.71}\text{Ni}_{0.29}$  with an uncertainty of about 15 %, arising from uncertainties of the diameter. The corresponding bulk values reported in the literature are lower with 7.8  $\mu\Omega\text{cm}$  for Ni and about 11  $\mu\Omega\text{cm}$  for all remaining Co-Ni compositions.<sup>44</sup> Increased resistivities of not annealed electrodeposited thin films is well known and reported for Co-Ni by Tóth *et al.*<sup>27</sup> This is attributed to the nanocrystallinity and crystal defects, resulting from the electrochemical deposition process. The temperature dependent resistance is shown in Figure 5-1. The alloys show a residual resistivity between 7.0  $\mu\Omega\text{cm}$  and 8.7  $\mu\Omega\text{cm}$  extrapolated to zero temperature, while residual resistance of the Ni nanowire is almost negligible. These values agree well with literature values between 3.48  $\mu\Omega\text{cm}$  and 10.3  $\mu\Omega\text{cm}$  for 24 % and 71 % Co content.<sup>157</sup> The structural and compositional properties have been confirmed by TEM analysis shown for a Ni-rich nanowire in Figure 5-2 and for a Co-rich nanowire in Figure 5-3. In particular, the polycrystalline nature of the deposited materials is observed in the various diffraction patterns as well as in the bright field TEM images. Due to contrast difficulties resulting from the thickness of the nanowire, only few crystals could be analyzed with the TEM. Therefore, the statistics is not sufficient to draw conclusions regarding the size of the crystallites, but from previous X-ray diffraction (XRD) measurements performed on nanowire arrays of the same compositions hcp crystal sizes of  $9\pm 2$  nm are expected.<sup>99</sup> In addition, lattice dislocations and defects are often observable in bright field micrographs (see Fig-

ure 5-3 (a-c)). A more detailed analysis of the diffraction patterns is presented in the Appendix: Figure 7-2 and Figure 7-3.

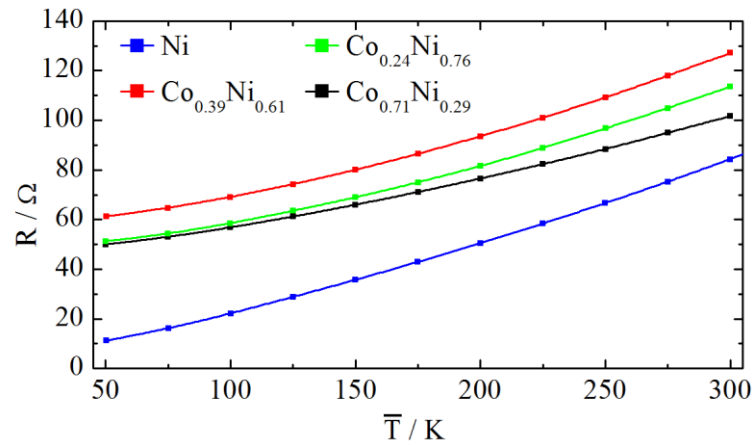


**Figure 5-1** The nanowire resistance at zero magnetic field as a function of the temperature.

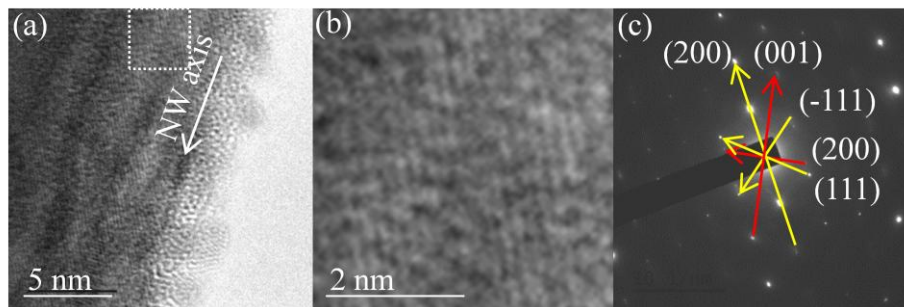


**Figure 5-2** (a) TEM of a  $\text{Co}_{0.39}\text{Ni}_{0.61}$  nanowire with oxide shell of few nanometers. The marked the area (white square) indicates the corresponding magnified area in (b). The corresponding selected area electron diffraction (SAED) pattern is shown in (c), with arrows on the reflexes that can be assigned to lattice planes represented in Miller indices (hkl). The amount of reflexes proves the polycrystalline character of the sample. The yellow arrow can be assigned to fcc lattice along the (0,1,-1) direction, while the red arrow represents a fcc lattice along the (0,1,0) direction.

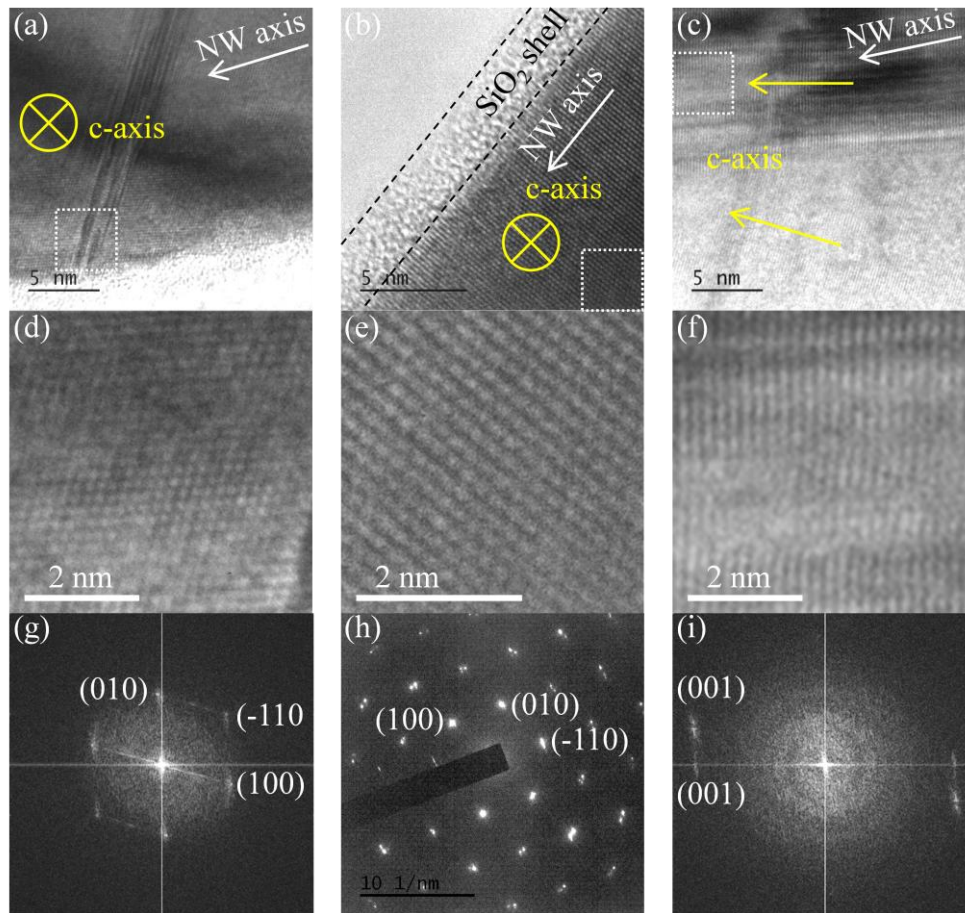


**Figure 5-3** (a-c) Transmission electron micrographs of three  $\text{Co}_{0.71}\text{Ni}_{0.29}$  nanowires with oxide shell of few nanometers. The yellow markers represent the c-axis of the hcp Co-Ni lattice obtained from the SAED patterns shown in (g-h). The marked areas (white squares) indicate the corresponding magnified areas in (d-f). In (g-i) Miller indices (hkl) are assigned to the observed diffraction patterns. (g) and (h) show very similar patterns, which can be attributed to a view axis along the c-axis. In (i) the (001) plane fits well to the observed diffraction patterns, which are slightly tilted towards each other indicating the polycrystalline character of the samples.

### 5.1.1 Magnetoresistance at RT

Figure 5-4 shows the influence of the applied magnetic field direction on the magnetoresistance ( $MR = \rho_H / \rho_0 - 1$ ) behavior of two nanowires with different Co content. Vega *et al.*<sup>99</sup> published crystallographic analysis and magnetometry study on nanowire arrays and verified a dominating shape anisotropy in nanowires with Co content below 50%. The strong easy axis in direction of the nanowire axis results in a vanishing AMR effect in this direction, as displayed by the open green symbols in Figure 5-4. In the contrary, nanowires with Co content above 60% show hcp crystal phases with dominating magnetocrystalline anisotropy in comparison to the shape anisotropy. Consequently, the remanent magnetization is not completely aligned parallel to the nanowire axis and results in stronger MR effects in parallel applied magnetic field when compared to the perpendicular direction. From the ratio of parallel to perpendicular effects it can be concluded that the magnetization of the Co-richest nanowire (ratio of 2:1) is randomly aligned in zero magnetic fields (two perpendicular axes to one parallel axis).

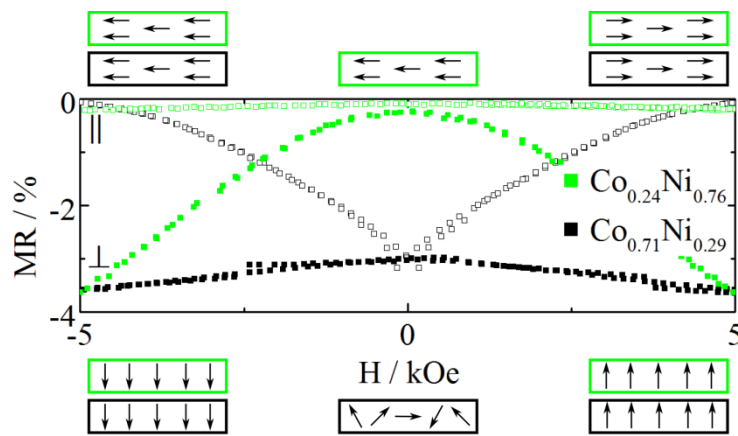


**Figure 5-4 Magnetoresistance relative to the saturation value of a parallel to the nanowire axis applied magnetic field. The open/closed symbols represent the measurement in parallel/perpendicularly applied magnetic fields, respectively.**

The setup is restricted to magnetic fields of 5.5 kOe, which is however not sufficient to completely saturate the Co-richest nanowires in perpendicular direction. Therefore, the actual ratio could be presumably lower. To verify this conclusion, the c-axes—the easy axis in this case—are obtained from selected area electron diffraction (SAED) patterns shown in Figure 5-3 (a-c). The distances and angles between the diffractions spots are compared to lattice parameters (Appendix: Table 7-1 and Appendix: Figure 7-3). Within this small statistics, the c-axes is preferably

aligned perpendicular and in a few cases parallel to the nanowire axis. This is consistent with XRD measurements with a preferred c-axis perpendicular to the nanowire axis.<sup>99\*</sup> The following measurements are focused on the perpendicular MR, which is measured in the VersaLab cryostat with magnetic fields up to 3 T. Figure 5-5 shows MTEP—discussed in the next chapter—and MR measurements of different Co-Ni alloy nanowires during sweeps of the magnetic field from negative to positive values. The curves are measured at RT, but due to an applied voltage of 10 V to the heater, the average temperatures of the four samples are quite different. The observed saturation fields in perpendicular direction increase with Co content from 3.2 kOe for the Ni nanowire to 11 kOe for the Co-richest nanowire. This fits very well to the literature values assuming uniaxial anisotropy ( $H_S^\perp = 2 \pi M_S$ )<sup>100</sup> of 3.2 kOe for Ni and of 8.8 kOe for Co.<sup>67</sup> The composition dependent change is caused by the increase of the saturation magnetization with increasing Co content. In addition, at Co contents higher than 60 % the magnetocrystalline anisotropy contribution from hcp phases overshadows the uniaxial shape anisotropy and the saturation field becomes higher than the simple model ( $H_S^\perp = 2 \pi M_S$ ) predicts.

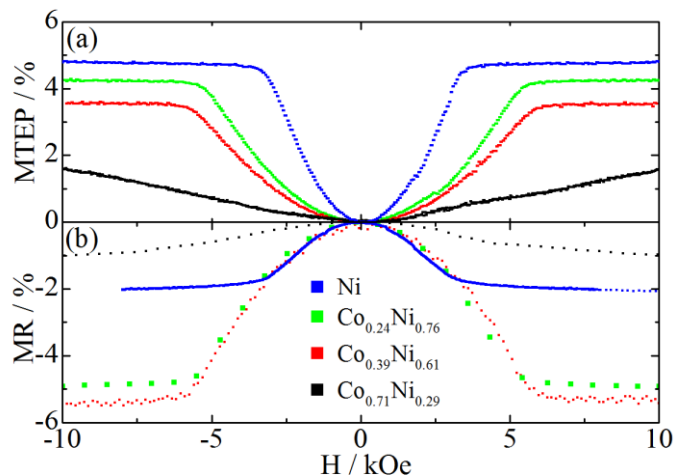


**Figure 5-5 (a) Magneto-thermoelectric power and (b) corresponding magnetoresistance curves in a perpendicular applied magnetic fields above RT.**

\* The (2 -1 -1 0) peak has increased intensity, while the (0002) peak shows a smaller intensity than expected from a standard polycrystalline sample.

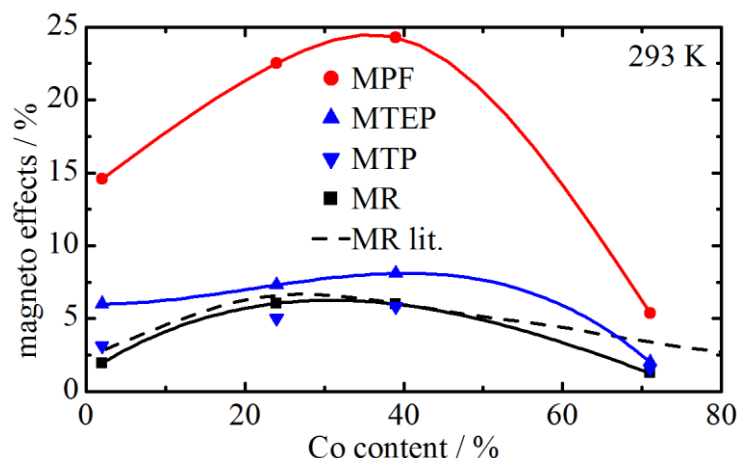


**Figure 5-6** MTEP, MTP, MR, and MPF are interpolated at 293 K. The literature values of the AMR in bulk alloys are taken from McGuire *et al.*<sup>44</sup>

To give an overview of the maximum effects Figure 5-6 shows the dependence on the composition at RT. The magnitude of the MR effects of the four alloy compositions are comparable to reported values in nanowire literature<sup>158-160</sup> and with the exception of the Co-richest sample comparable to AMR bulk literature.<sup>28,44,45</sup> The effects are quite high for AMR effects in general with a maximum of 6 % and only a factor of six times smaller than the highest values measured on GMR multilayered nanowires.<sup>58</sup> The agreement of the perpendicular MR of Ni-rich nanowires with AMR literature is a proof for a saturated magnetization along the nanowire axis in remanence. As already mentioned the MR of the Co-richest sample is lower than expected from the literature, as shown in Figure 5-6. This is explainable by the increased magnetocrystalline anisotropy and a distribution of the effect on perpendicular and parallel direction (see Figure 5-4), while only the perpendicular effect is measured. *Magneto-optic Kerr effect* (MOKE) experiments using a 4  $\mu\text{m}$  laser spot on single nanowires are shown in Figure 5-7. This magnetometry method possesses the ability to measure the relative magnetization of the outer shells of a single nanowire in a parallel magnetic field. The single Barkhausen jumps of the Ni-rich nanowires clearly indicate uniaxial anisotropy parallel to the nanowire, while the Co-richest nanowire curve can be interpreted as partly jump-like and partly reversible/rotational switching.<sup>99</sup> By vibrating sample magnetometry (VSM), the magnetization hysteresis in perpendicular and parallel magnetic fields with respect to the nanowire axis is recorded. From the curves in perpendicular magnetic fields, the anisotropy field distribution (AFD) is determined. This method was developed by Barandiaran *et al.*<sup>161</sup> and applied to nanowires by de La Torre Medina *et al.*<sup>162</sup> It provides a simple approach to determine the field necessary to saturate the material along the magnetization hard axis. For nanowire arrays, the magnetization behavior is a combination of the anisotropy of single nanowire as well as the nanowire-nanowire interactions in the array.

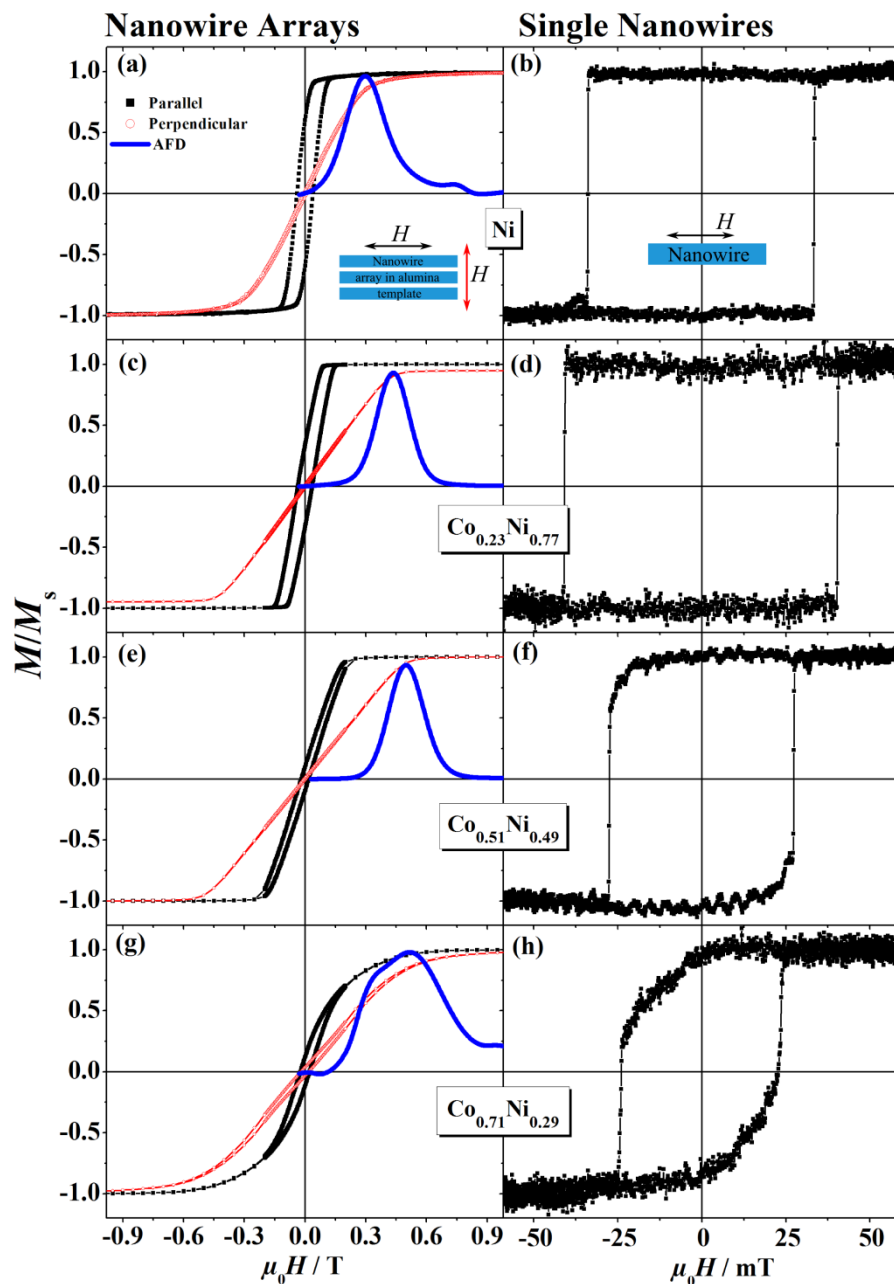


Figure 5-7 Relative magnetization curves displaying the different magnetization behavior of Co-Ni alloy nanowire arrays and single nanowires. Measurements are done by vibrating sample magnetometry (left hand side) and magneto-optical Kerr magnetometry (right hand side) in cooperation with Stephan Martens and published in Vega *et al.*<sup>99</sup> The anisotropy field distribution (AFD) curve is obtained from perpendicular hysteresis loops. The coercive fields of the single nanowire measurements are affected by statistical deviations between nanowires.

A substantially different magnetic behavior is observed in the Ni-rich nanowires compared to the Co-rich nanowires, as discussed in detail by Vega. *et al.*<sup>99</sup> and verifies the conclusions of the transport measurements. By applying X-ray photo electron emission microscopy (XPEEM), similar to the results published by Kimling *et al.*,<sup>163</sup> the magnetic domain structure of a Ni-rich and a Co-rich nanowire is recorded. In comparison with MOKE, additional information of the domain positions as well as the perpendicular contributions is available. Due to intensity shift of the X-ray beam quantitative results of the magnetization are difficult, but by a rough normalization to the background noise differences can be detected. Figure 5-8 shows the bistable magnetization behavior Ni-rich nanowire in contrast to the complex domain structure with multiple domains of the Co-rich nanowire in Figure 5-9. Figure 5-9 (d) and (e) show the different perpendicular magnetization contributions depending on the Co content, which is much higher than in the Ni-rich nanowire, due to an rather isotropic anisotropy distribution. Simulations of the switching process of granular Co nanowire arrays predict similar results to the XPEEM images.<sup>164</sup>

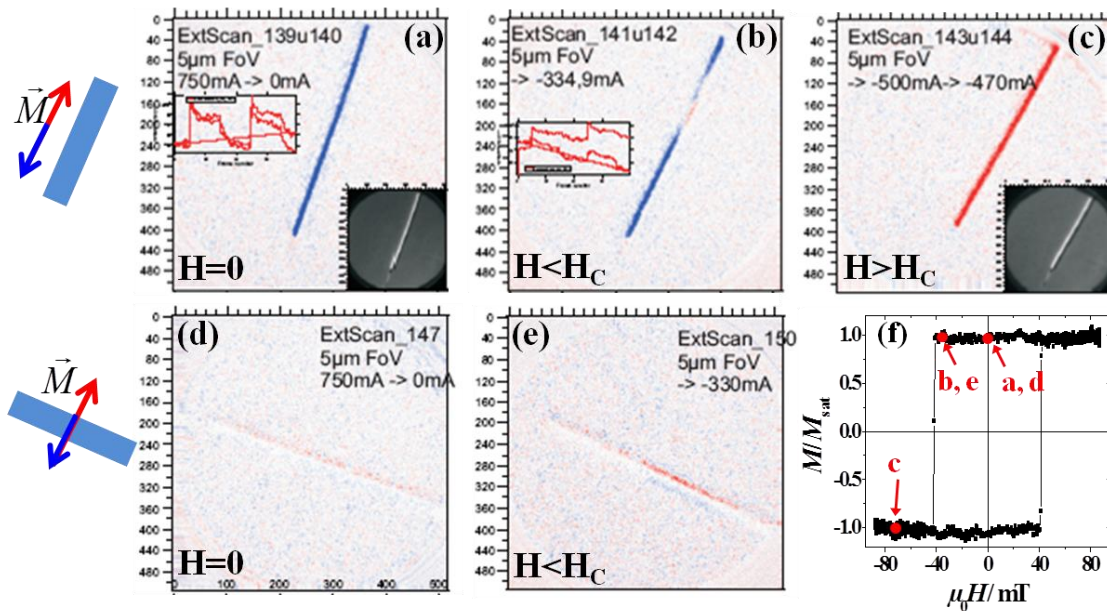


Figure 5-8 XPEEM images showing components of the magnetization in the directions parallel (a, b, c) and perpendicular (d, e) to the nanowire axis and at different applied magnetic fields ( $H_C$  is the coercive field) for a single  $\text{Co}_{0.38}\text{Ni}_{0.62}$  nanowire. The magnetization configuration shown in (b) is a very rare state and untypical for these nanowires.\*

\* These results are obtained within a large cooperation and first published in Ref. <sup>206</sup>.

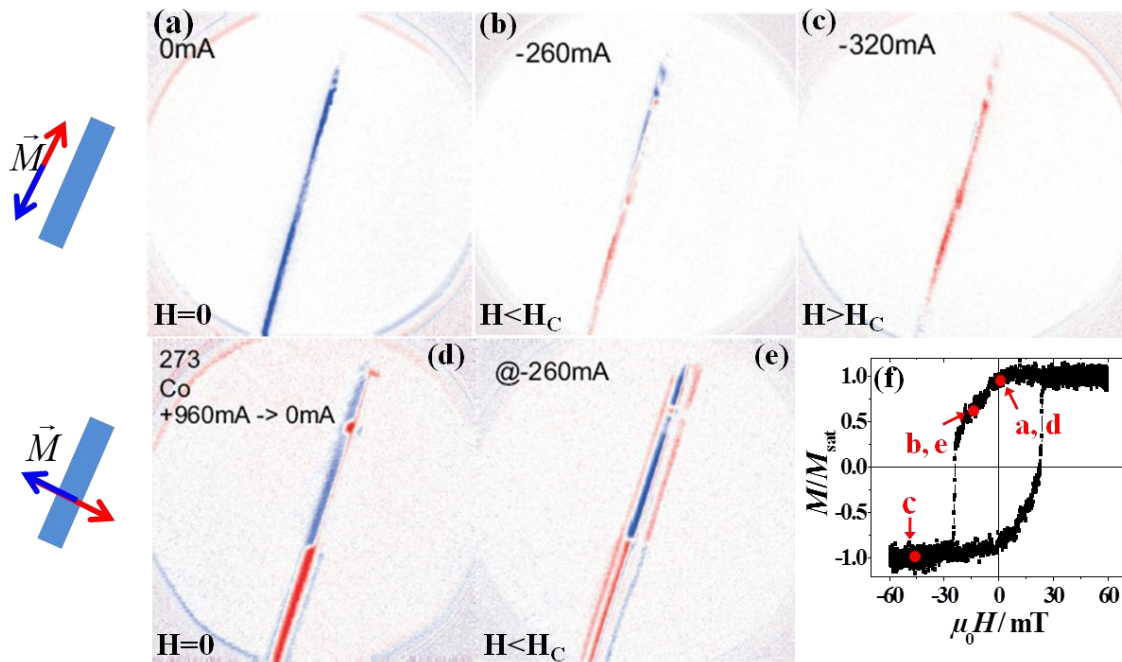


Figure 5-9 XPEEM images showing components of the magnetization in the directions parallel (a, b, c) and perpendicular (d, e) to the  $\text{Co}_{0.71}\text{Ni}_{0.29}$  nanowire axis at different applied magnetic fields ( $H_C$  is the coercive field).\*

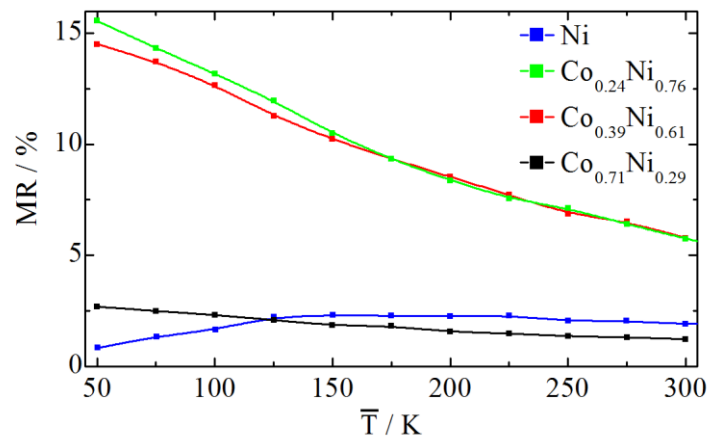


Figure 5-10 The transverse MR as a function of the temperature.

### 5.1.2 Temperature dependent MR

The temperature dependent MR curves—shown in Figure 5-10—display much higher effects in samples with intermediate Co content compared to the pure Ni and the Co-richest nanowire.

\* These results are obtained within a large cooperation and first published in Ref. <sup>206</sup>.

This behavior can be expected from bulk literature values for Co-Ni alloys,<sup>28,44,45</sup> as discussed in the previous section. Interesting is the decreasing MR of the Ni nanowire at temperatures below 150 K, which is probably due to the decrease of phonon scattering and dominating defect scattering, resulting in a decreased AMR.<sup>28</sup>

## 5.2 Magneto-Thermopower

The Seebeck coefficients or thermopowers of the nanowires are measured in perpendicular magnetic fields and are expected to behave similar to bulk literature values. Due to an increasing uncertainty with temperature, the RT values are extrapolated from lower temperatures considering a linear behavior. The RT values of  $-16 \mu\text{VK}^{-1}$  for Ni,  $-16 \mu\text{VK}^{-1}$  for  $\text{Co}_{0.24}\text{Ni}_{0.76}$ ,  $-21 \mu\text{VK}^{-1}$  for  $\text{Co}_{0.39}\text{Ni}_{0.61}$  and  $-29 \mu\text{VK}^{-1}$  for  $\text{Co}_{0.71}\text{Ni}_{0.29}$ . are in good correspondence with the bulk value for Ni with  $-14.5 \mu\text{VK}^{-1}$  and exceed the bulk value of Co with  $-25.8 \mu\text{VK}^{-1}$  (see Table 2-1).<sup>72,73</sup> The increase of  $S$  of the alloy with respect to the pure element might be surprising, but this behavior is known for example from literature on Fe-Ni alloys.<sup>165</sup> In the following sections, the magnetic field and temperature dependent behavior of the thermopower is analyzed.

### 5.2.1 Temperature Dependent $S$

The Seebeck coefficients show a monotonic increase with the temperature (see Figure 5-11), which is in agreement with literature in the case of a single type of charge carrier, dominating diffusive thermopower and consistent scattering channels.<sup>68</sup> Deviations are mostly due to measurement errors of the resistance thermometers. Fitting the temperature difference over the whole temperature range can reduce deviations, while the uncorrected data gives a good idea of the accuracy. There are no indications for phonon-drag effect, which would appear as an inflexion point or a local maximum or minimum of  $S$  between 20 K and 150 K. The measured Ni values compare very well with the results of Shapira *et al.*<sup>16</sup> In nanowire experiments no phonon-drag is typically observed, while literature data on bulk Ni shows a characteristic phonon-drag peak between 20 K and 100 K, as shown in Figure 5-11.<sup>166,167</sup> Shapira argues that phonon confinement in the 30 nm nanowire suppresses the phonon-drag contribution. Also Zink *et al.*<sup>168</sup> detected no phonon-drag in sputtered Ni thin films and it seems reasonable to contribute this to a confinement effects from either the sample and/or the electrical contacts.<sup>41,42,68</sup> The offset between annealed bulk Ni and Co literature and nanowire measurements is probably equivalent to the absolute thermopower of Pt, due to absolute thermopower values of the bulk data.<sup>72,167</sup> Unfortunately, the contact material in the annealed bulk Ni literature is not specified

in the publications. Bulk data from Maeda *et al.*<sup>165</sup>—calibrated against Pt contacts—shows a better correspondence, but a significant deviation above 150 K, which reveals the difficulties to determine universal values.

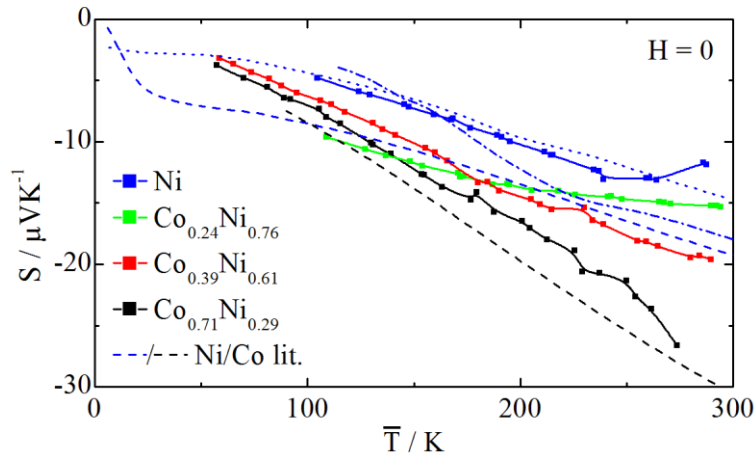


**Figure 5-11** Temperature dependence of the Seebeck coefficient at zero applied magnetic field of the nanowires and three literature curves blue: (dashed) annealed absolute bulk Ni/Co values,<sup>72,167</sup> (dashed-dotted) bulk Ni against Pt,<sup>165</sup> and (dotted) Ni nanowire against Pt.<sup>16</sup>

### 5.2.2 Magnetic Field Dependent Thermopower—MTEP

The magnetic field dependent MTEP of different Co-Ni compositions are displayed in Figure 5-5(a) on page 66. During the measurement, the cryostat is set to RT, but the applied heater voltage raises the average temperatures of the individual nanowires. As discussed for the MR, the observed saturation field increases with Co-content and fits to literature values. To compare the effect values qualitatively, the different saturation values are fitted to 294 K and plotted against the composition in Figure 5-6. The MTEP shows roughly the behavior of the MR but is generally higher except for the Co-richest nanowire. If the offset in the Seebeck coefficient due to the platinum contacts is estimated by literature values given by Roberts *et al.*<sup>9</sup>, the MTP values can be calculated according to section 2.2.4. Applying the literature value of pure bulk Pt is a rough estimation, but the results show a good agreement with the MR data in Figure 5-6. The deviation between MTEP and MR is probably the direct result of a magnetic field independent offset of the electrical contacts, which influence gets weaker with increasing absolute Seebeck coefficient. The impact of the correction is remarkable and possibly explains why the measured MTEP values in literature are often deviating from MR values.<sup>31,32,36,38,62,90,159,169-173</sup> A more detailed study of the relation between MTEP, MTP and MR according to the Mott formula and measurement data is conducted on multilayered nanowires in chapter 6.

### 5.2.3 Temperature dependent MTEP

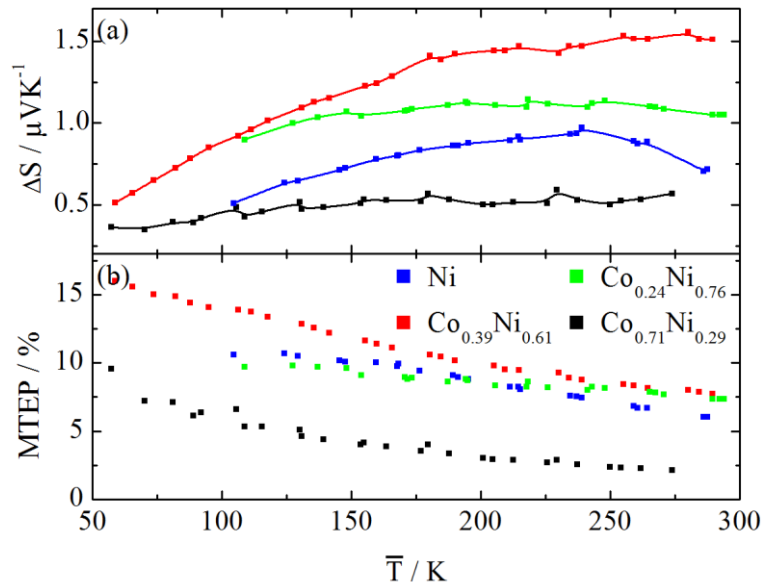


**Figure 5-12** Temperature dependence of the absolute (a) and the relative change (b) of the Seebeck coefficient in the magnetic field of the four nanowire samples between zero magnetic field and saturation field.

The temperature dependence of the absolute change of the Seebeck coefficient between zero and saturation magnetic fields  $\Delta S = S_0 - S_{\text{sat}}$  is shown in Figure 5-12(a). The maximum  $\Delta S = 1.5 \mu\text{VK}^{-1}$  is measured at RT in  $\text{Co}_{0.39}\text{Ni}_{0.61}$  nanowires. Recently, a value of  $4.5 \mu\text{VK}^{-1}$  has been reported for permalloy/Cu/permalloy spin valves, although it is difficult to estimate the temperature gradient in such structures.<sup>19</sup> Similar to the MR, the absolute change of the Seebeck coefficient due to the perpendicularly applied magnetic field is weak for the Ni wire and the Co-richest sample and stronger for the alloys with intermediate compositions. This relation can be derived from the Mott formula, as discussed in the next chapter. The relative change of the Seebeck coefficient—the MTEP—is displayed in Figure 5-12(b). Although, the effect sizes and general temperature behavior are comparable to the MR for some compositions, there are also considerable deviations for example in the case of the Ni nanowire. At this point the MTP could be calculated for the whole temperature range similar to Figure 5-6 on page 67, unfortunately the results are unsatisfying and cannot be understood at this point. The main reason is the deviation between the literature values and the actual Seebeck coefficient of our contact material. Although the deviation seems small at RT, it becomes obvious at lower temperatures. The Ni nanowire at 100 K has a measured thermopower of  $-4.8 \mu\text{VK}^{-1}$ , the absolute literature value of pure bulk Pt<sup>85</sup> is already  $4.296 \mu\text{VK}^{-1}$ . As a result, the absolute thermopower  $S_{\text{Ni}}$  ( $\sim -0.5 \mu\text{VK}^{-1}$ ) would be of the same magnitude than the absolute change in the applied magnetic fields  $\Delta S_{\text{Ni}}$  shown in Figure

5-12(a), which is unreasonable as discussed in chapter 6. The analysis of the MTP is delayed to measurements on multilayered nanowires, which can be more differentiated evaluated due to higher effects.

The power factors (PFs) in remanence at RT are calculated to be 1.7 mW/K<sup>2</sup>m for Ni, 1.1 mW/K<sup>2</sup>m for Co<sub>0.24</sub>Ni<sub>0.76</sub>, 2.0 mW/K<sup>2</sup>m for Co<sub>0.39</sub>Ni<sub>0.61</sub> and 3.7 mW/K<sup>2</sup>m for Co<sub>0.71</sub>Ni<sub>0.29</sub> nanowire. The PF is a measure of the power output of thermoelectric generators made out of the materials and the thermopowers are in reference to Pt, which is typical in the thermoelectric community. For comparison, the PF of a common thermoelectric bulk material like Bi<sub>2</sub>Te<sub>3</sub> at RT is up to 1.9 mW/K<sup>2</sup>m, while the PF in nanowires is typically five times smaller.<sup>174,175</sup> The magnetic field induced changes between zero and saturation field—called *magneto power factor* (MPF)—range between 0.20 mW/K<sup>2</sup>m (5.4 %) for the Co-richest sample and 0.49 mW/K<sup>2</sup>m (24 %) for the Co<sub>0.39</sub>Ni<sub>0.61</sub> nanowire. The MPF is plotted against the composition in Figure 5-6 on page 66. The thermoelectric power factors  $PF=S^2\rho^{-1}$  are calculated in zero magnetic field and saturation as shown in Figure 5-13 as a function of the temperature. In metals the heat is dominantly carried by electrons and the thermal and electrical conductance are proportional. Therefore, the figure of merit in metals is typically proportional to  $S^2$ . Using this proportionality via the Wiedemann-Franz law,<sup>76,77</sup> the ZT of these Co-Ni alloys can be determined to be between 0.01 and 0.034 at RT, which is low compared to commercially available thermoelectric materials with a ZT of 1 and results in a factor of 100 to 20 lower efficiency compared to ZT of 1.<sup>176</sup> Thermoelectric generators have a typically low efficiency compared to the Carnot efficiency and their application is restricted to niches or to utilizing waste heat of existing generators. The geometry and temperature conditions in these applications are given parameters and the thermoelectric modules have to be design accordingly. High efficiency materials need typically more surface area to compensate their low thermal conductivity. As several publications show, a fixed heat flow and a restricted surface area leads to situations, in which high PF materials can convert more heat power than high ZT materials and are ultimately more efficient.<sup>79,80</sup> Therefore, due to the high PF of Co-Ni alloys with high Co content are suitable for specific applications as a thermoelectric material.

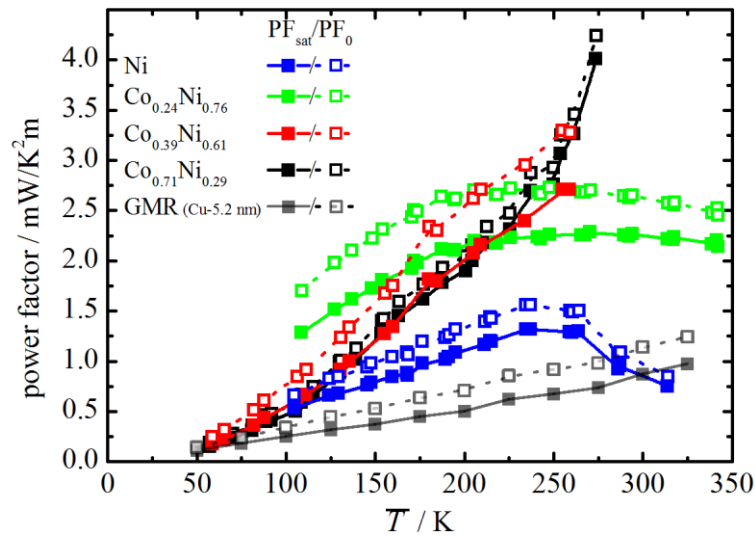


**Figure 5-13** Temperature dependence of the PF in zero magnetic field and saturation field. For comparison, the values of a typical GMR nanowire (Cu-5.2 nm) are displayed.

### 5.3 The Mott Formula— $S$ vs. $R^{-1}$

Figure 5-5(a) and (b) show the MTEP and the MR as a function of perpendicular applied magnetic fields. Comparing the curves of the individual nanowires reveals a strong correlation between both effects. The proportionality of  $S$  and  $R^{-1}$  below the saturation field is shown in Figure 5-14. In general, the dependence between the diffusive thermopower and the electrical conductivity is described by the Mott formula (2.2-21). The magnetic field dependency of the Seebeck coefficient is a direct result of the MR and the energy derivative of the resistivity is magnetic field independent. To compare the different samples relative values are used. The change of the Seebeck coefficient in the applied magnetic field can be related to the MR:

$$\begin{aligned} \Delta S(H) &= \frac{cT}{\rho_0} \text{MR}_{\text{inf}}(H) \left( \frac{d\rho}{dE} \right)_{E=E_f} \\ &= cT \cdot \text{MR}_{\text{inf}}(H) \left( \frac{d \ln \rho_0}{dE} \right)_{E=E_f} \end{aligned} \quad (5.3-1)$$

with the inflationary magnetoresistance  $\text{MR}_{\text{inf}}(H) = 1 - \rho_0/\rho(H)$  and  $c = \pi^2 k_B^2 / 3q$ . Figure 5-15(b) displays this relation by the data from the curves in Figure 5-5 with the applied magnetic field as an implicit variable. The absolute change of the Seebeck coefficient of the Ni-rich compositions shows a linear dependency to the MR. As shown previously in Figure 5-14, the nanowires show a deviation from this relation above the saturation field.

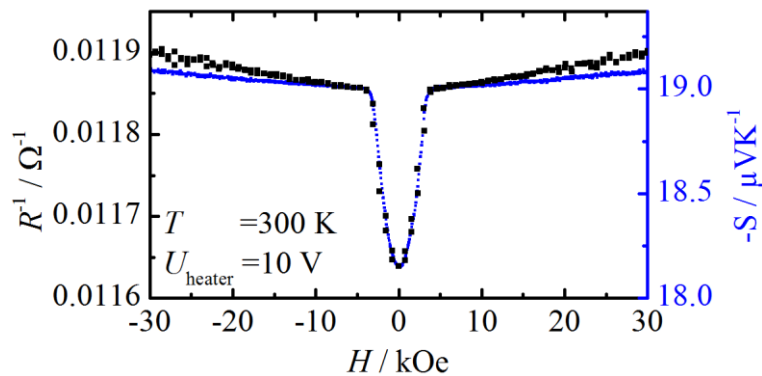


**Figure 5-14** Magnetoconductance and corresponding magneto-thermoelectric power curve with the cryostat at RT and a heater voltage resulting in a temperature difference of 11.5 K. The linear relationship between  $R^{-1}$  and  $S$  is obvious in the AMR dominated part. Above the saturation, a clear deviation is observable.

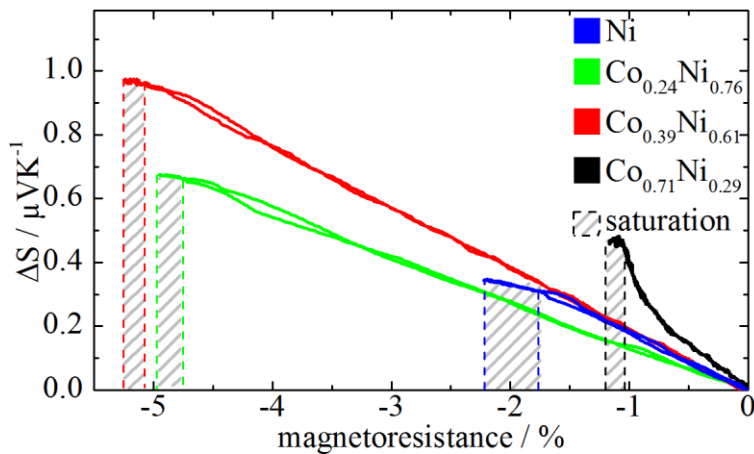


**Figure 5-15** The thermopower data from Figure 5-5 are plotted against the  $MR_{inf}$  with the applied magnetic field as an implicit variable. The saturation region of the AMR effect is marked by hatched boxes.

The data suggest that the MMR does not lead to the same linear relationship as the AMR. It seems both regimes accomplish a linear relationship, although the changes in the saturation are too small to make precise statements. The slope is decreased above the saturation fields, which indicate a stronger influence of the AMR effect on the thermopower compared to the MMR. In the case of the Co-richest nanowire, the slope increases by a factor of three and again decreases above saturation (see Figure 5-15). This leads to the assumption that another contribution to the MR is present that influences  $S$  stronger than the MR compared to the AMR. One characteristic that differentiates the Co-richest nanowire is the hcp crystal structure with a preferred  $c$ -axis orientation perpendicularly to the nanowire axis, as discussed in section 5.1.1. The hcp

crystal structure exhibits dominating magnetocrystalline anisotropy compared to the shape anisotropy, which leads to a granular reversal behavior and a manifold occurrence of magnetic domain boundaries between crystal grains. The magneto effects due to these boundaries might result in additional non-diffusive thermopower contributions (magnon-drag thermopower) or lead to different ( $dp/dE$ ) values and a non-linear Mott behavior. Although domain wall resistance is a topic of interest since the 70's, only recently results on the thermopower of domain walls are published. A transition between the anisotropic magneto-thermopower and a second domain wall related effect could explain the observed behavior. Most straight forward is an explanation by the MMR or magnon-drag thermopower,<sup>96,177</sup> due to the composition change or the domain structure, even though it is questionable if a small effect like the MMR could explain changes in this order of magnitude. In Co and Ni thin films a resistance change due to narrow domain walls in the range of 1 % was found and attributed to GMR related effects.<sup>178</sup> A similar behavior is known from granular Ag/Co systems that show GMR effects.<sup>94</sup> Due to superparamagnetic particles in such systems, the magnetic field behavior deviates from the typical  $H^2$  behavior of the AMR/GMR effect. This could lead to a field dependent transition from one effect to the other. By determining reliable ( $dp/dE$ ) or ( $d\ln\rho/dE$ ) values for the different magnetoresistance effects and by comparing them to the measurement, this could be tested. Although such measurements are challenging and different material systems are probably not comparable, this seems like an interesting way to distinguish different magnetoresistance effects.

## 5.4 Permalloy Nanowires

Josep M. Montero Moreno prepared permalloy nanowires with diameters of  $138\pm 10$  nm, which are measured to verify previous thermopower results on a second material system. The deposition method and recipe are described elsewhere.<sup>179</sup> The temperature and temperature gradient dependent switching field was studied on these nanowires and compared to Co-Ni nanowires. These results in parallel magnetic fields should not be the topic of this thesis and are discussed elsewhere.<sup>141\*</sup> The measured Seebeck coefficients  $S$ , change of  $S$  in the magnetic field  $\Delta S$ , and MTEP are presented in Figure 5-16. The composition of a permalloy nanowire is analyzed by TEM-EDX shown in Figure 7-4(c) and found to be 39 at.% Fe and 61 at.% Ni. The negative Seebeck coefficient is not surprising for a Ni-rich alloy, while the positive literature value of the ab-

---

\* Master's thesis of Ann-Katrin Michel, supervised during this PhD thesis.

solute thermopower of Fe ( $15 \mu\text{VK}^{-1}$ ) is dominated by the negative thermopower of Ni.<sup>73,75</sup> This behavior was found even for Fe-rich nanowires with thermopower magnitudes higher than  $-30 \mu\text{VK}^{-1}$ .<sup>165</sup> The SAED patterns suggest fcc lattice as expected for Fe-Ni alloys, which is in accordance with literature that reports fcc lattice below 50 at.% Fe—electrodeposited from a comparable electrolyte.<sup>180</sup> In comparison with Co-Ni alloy nanowires, the Seebeck coefficient is higher, but also shows a characteristic maximum around room temperature. According to Maeda *et al.*,<sup>165</sup> this is due to the temperature dependent “magnetic part” of the Seebeck coefficient due to the remanent magnetization. This magnetic contribution to the Seebeck coefficient should decrease with higher Ni content and it seems that the measured values fit between literature curves for 50 % Ni and pure Ni.<sup>16,165</sup>

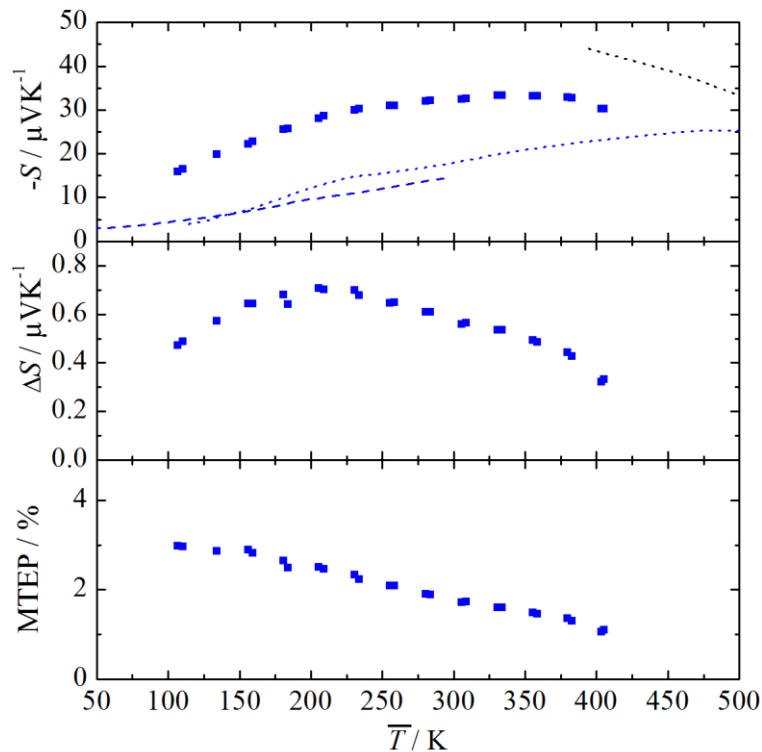


**Figure 5-16 (a)** Seebeck coefficients  $S$ , change of  $S$  in the magnetic field  $\Delta S$  and MTEP of a permalloy nanowire. Literature curves against Pt: (black dotted)  $\text{Ni}_{0.5}\text{Fe}_{0.5}$  bulk, (blue dotted) Ni bulk,<sup>165</sup> and (blue dashed) Ni nanowire.<sup>16</sup>

## 5.5 Conclusion AMR and MTEP of Co-Ni alloy Nanowires

Magnetic field and temperature dependent transport measurements on single nanowires with four different Co-Ni compositions are presented. The measurement setup proves to be a reliable and versatile way for the thermoelectric characterization of nanowires and even nanostructured thin films, as published several times.<sup>39,144,146,148</sup> By using TEM analysis, the crystal structures of the samples are evaluated. The Co-richest sample shows a hcp structure, while the Ni-rich samples show fcc structures. The resistance and residual resistivity of the nanowires is about a factor of two higher than bulk literature values, which is reasonable for as-prepared electrochemically deposited samples. At RT a maximum AMR effect of 6 % is reached for the two samples with medium Co content. The temperature dependent measured Seebeck coefficients and AMR values similar to those reported in the literature for bulk Co-Ni alloys and Ni nanowires. The magneto-thermoelectric power and the absolute change of the thermopower in the magnetic field are determined temperature dependent. By correcting the MTEP values by literature values of Pt, the contact material, the MTP values at RT are obtained, which show a convincing agreement with the AMR values, as investigated further in the next chapter. In the case of the Ni-rich nanowires, a linear relationship between the magnetic field dependent modulation of the Seebeck coefficient and the electrical conductivity is found as expected from the Mott formula, while the Co-richest nanowires show a distinct non-linear behavior. In addition, the thermoelectric properties of a Permalloy nanowire are measured to verify the results on a second material system. Returning to the motivation and the statement of Avery *et al.*,<sup>156</sup> it seems the relationship of the Ni-rich nanowires can indeed be described by a simple scaling factor and motivates further investigations in the next chapter.



## 6 Thermoelectric Transport in Giant Magnetoresistance

### Nanowires

Recently, Heikkilä *et al.*<sup>21,22</sup> introduced the concept of spin heat accumulation for perpendicular-to-plane transport in spin valve or multilayered structures that might lead to a violation of the Wiedemann-Franz law. The highly interesting spin-Peltier effect<sup>172</sup> and the novel spin-Seebeck effect<sup>12</sup> could lead to similar deviations, which are observable in the magnetotransport behavior. Multilayered nanowires with giant magnetoresistance (GMR) record values of 35 %<sup>58</sup> are the perfect model systems to experimentally investigate spin dependent current perpendicular-to-plane transport. In literature, the Co-Ni/Cu multilayered nanowires generally show higher GMR effect sizes<sup>58,125,181-183</sup> compared to Co/Cu multilayered nanowires.<sup>31,126,169-171,184-187</sup> Although, up to now no Seebeck coefficient values of electrodeposited Co-Ni/Cu multilayered nanowires are published. A similar picture as for the Co-Ni alloyed nanowires in the previous chapter can be expected with significantly higher magnitudes. This makes a deeper analysis possible compared to the alloyed nanowires. The measurement procedure is optimized to reduce offsets and secondary effects, while obtaining a complete magnetic field and temperature dependent characterization. To avoid an induction voltage offset, the measurements are conducted at constant magnetic fields. Nernst effects and time-dependent changes are corrected, as described in section 4.6. The magnetoresistance and magneto-thermopower include components related to the GMR, the anisotropic magnetoresistance (AMR), and the magnon magnetoresistance (MMR). Below the saturation field, the GMR and AMR effects dominate, while above the saturation field the MMR affects the magnetotransport.<sup>47</sup> The AMR and MMR effects can be estimated from Co-Ni bulk effects considering the additional residual resistance of interfaces and copper segments. The composition of the samples is determined by SEM-EDX on the cross section on the membrane and TEM-EDX on single nanowires, as shown in Figure 6-1. The homogeneity of the composition along and across the nanowire axis is confirmed by TEM-EDX—as shown in Appendix: Figure 7-4(d-g). A relative error of the composition between 5 % and 8 % is expected using these methods. The statistical deviation between TEM-EDX line scans on different nanowires is in the same range. The TEM-EDX measurements are corrected by the average Cu background signal of (27±5) % from the Cu grid sample holder. The average compositions determined by SEM-EDX and the corrected composition from TEM-EDX data aligns very well for the sample that is investigated with both methods, as shown in Appendix: Table 7-2. With information about the geometry and composition, the average thickness of the single layers can be estimated, as given in Table 6-1. Missing values are interpolated from the

nominal deposition values. The uncertainties add up to  $\pm 2.2$  nm due to these corrections (Appendix: Table 7-2). Therefore, the layer thicknesses are rather used to denote the samples than to demonstrate any thickness dependence. The alternative of using the nominal values of the deposition volume per surface also has its flaws, due to undefined surface area of the porous templates. The determination of the layer thicknesses of electrodeposited multilayered nanowires is a remaining problem.<sup>58</sup>

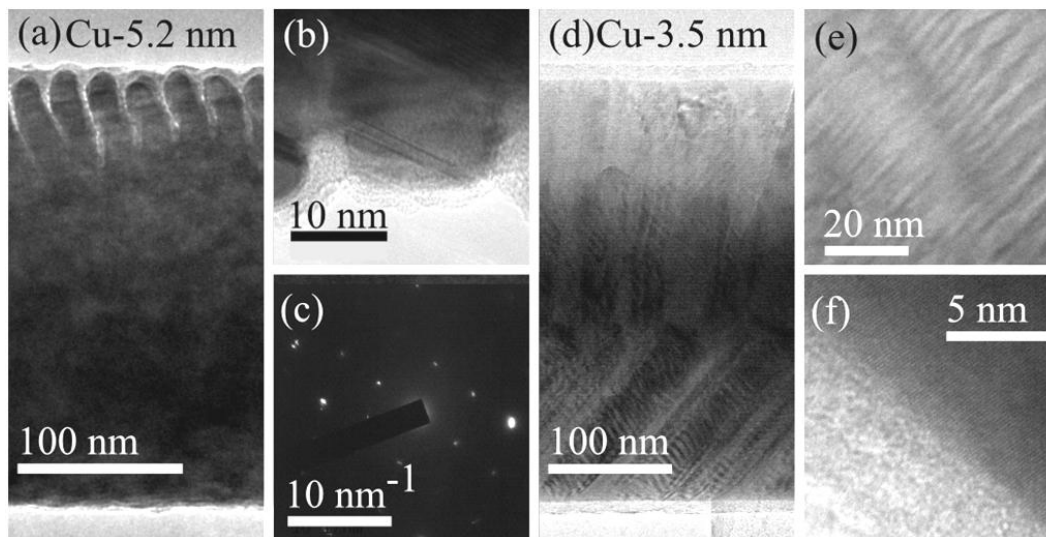


**Figure 6-1** (a) TEM image of sample Cu-5.2 nm with an average bilayer thickness of 22 nm. (b) TEM image and (c) the respective SAED spectra. (d) TEM image of sample Cu-3.5 nm with layered crystals or defects. (e) Magnification of bilayers with a thickness of 8.7 nm. (f) High resolution TEM with the oxide layer.

The SEM is used to determine the average diameter along the nanowire axis and the lengths of the measured nanowire sections. The diameters of the measured nanowires vary up to a factor of two, which is an extreme case of statistical deviation in the self-ordered process, but should not directly influence the physical properties. From the TEM analysis, the passivating ALD  $\text{SiO}_2$  shell is determined to be about 5 nm in thickness. Therefore, the diameter is reduced by 10 nm in the calculations. The Cu layer seems to be partly dissolved, as it can be seen in the top part of Figure 6-1(a). This could lead to an increased resistivity considering the original cross section, while diameter independent properties (MR, MTEP, or  $S$ ) should not be influenced (neglecting size effects).

The first two sections of this chapter outline the results of the *magnetoresistance* and the *magneto-thermopower* in magnetic fields and at different temperatures of multilayered nanowires.

The results are put into context with each other in the section *The Mott Formula—S vs. R-1*. In the following section *Conclusion Co-Ni/Cu Multilayered Nanowires* an overview of the results is given.

**Table 6-1** The bilayer thicknesses, the lengths  $l$  of the measured nanowire sections, and the average diameters of the nanowires according to TEM analysis are summarized. The overall compositions of Co-Ni and Cu layers (corrected by the average Cu background of the microscope) are given. In addition, the resistivities at RT are calculated.

Sample- $l_{\text{Cu}}$ / nm	$l_{\text{bilayer}}$ / nm	$l_{\text{NW}}$ / $\mu\text{m}$	$d_{\text{NW}}$ / nm	Co-Ni/Cu / atom ratio	$\rho$ / $\mu\Omega\text{cm}$
Cu-0.2 nm*	n/a	8.63	217 $\pm$ 7	n/a	30.7
Cu-0.8 nm*	n/a	8.00	182 $\pm$ 3	n/a	36.8
Cu-0.9 nm	17.3 $\pm$ 1.3	8.40	266 $\pm$ 3	33-66/3	33.2
Cu-1.4 nm	17.5 $\pm$ 1.5	8.24	214 $\pm$ 10	50-50/6	50.8
Cu-3.5 nm	8.7 $\pm$ 1 (9.2) <sup>†</sup>	8.04	165 $\pm$ 9	42-58/69 <sup>†</sup>	44.9
Cu-5.2 nm <sup>‡</sup>	22.6 $\pm$ 1.1	7.79	169 $\pm$ 3	30-70/29	28.7
Cu-5.2 nm <sup>§</sup>	22.6 $\pm$ 1.1	8.19	320 $\pm$ 13	30-70/29	67.6

## 6.1 Magnetoresistance

Crucial to understand the magnetotransport in the nanowires are the resistivity  $\rho$  and the magnetoresistance (MR),<sup>43-45</sup> which describes the change of the electrical resistance in external magnetic fields  $H$ . The resistivities at RT varies between 28  $\mu\Omega\text{cm}$  and 50  $\mu\Omega\text{cm}$ , as shown in Figure 6-2, with no dependence on the Cu layer thickness, as it is expected from a simple serial resistor model of the different layers. Thus it seems that the zero field resistance is dominated by unsystematic changes of the impurity concentration, the crystalline structure, and lattice defects. The almost linear curves with decreasing slope towards low temperatures are in agreement with literature.<sup>31,188</sup> The residual resistivity obtained from the temperature behavior

\* The Cu thickness for the sample name is fitted from the nominal values with an error of about  $\pm 2$  nm.

<sup>†</sup> Calculated values from TEM (SEM) data. The composition determined from SEM-EDX is 50-50/72.

<sup>‡</sup> Sample used for parallel/perpendicular resistance measurements at RT.

<sup>§</sup> Sample used for perpendicular magnetic field and temperature dependent resistance and thermopower measurements.

can be expected between  $16 \mu\Omega\text{cm}$  and  $35 \mu\Omega\text{cm}$ . These values are a factor of two to five higher than for the alloyed nanowires, which seems reasonable considering the additional scattering due to Cu impurities, interfaces, and spin dependence. A dependence on the Co-Ni composition is unexpected since Co-Ni alloys are known to have an almost constant resistivity of  $11 \mu\Omega\text{cm}$ .<sup>44</sup> Errors in the diameter measurement have to be considered and might lead to deviations up to 15 % of the resistivity. In literature it is not very common to give the electrical resistivities for multilayered nanowires, probably due to high contact resistances and an unknown geometry of the nanowires in the template. A few reference values at RT are  $35 \mu\Omega\text{cm}$ <sup>188</sup> for sputtered CIP Co-1 nm/Cu-1 nm multilayers,  $10 \mu\Omega\text{cm}$  to  $50 \mu\Omega\text{cm}$ <sup>189,190</sup> for electrodeposited CIP  $\text{Ni}_{0.81}\text{Cu}_{0.19}/\text{Cu}$  thin films with different thicknesses, and  $11 \mu\Omega\text{cm}$  to  $15 \mu\Omega\text{cm}$ <sup>171,173</sup> for electrodeposited Co-10 nm/Cu-10 nm multilayered nanowires measured in the template with an estimated diameter of 60 nm. Lenczowski *et al.*<sup>136</sup> investigated the CIP resistivity of electrochemically deposited Co/Cu thin films and found a decrease from  $15 \mu\Omega\text{cm}$  at 1 nm Cu layer thickness to  $5 \mu\Omega\text{cm}$  at 5 nm. Doudin *et al.*<sup>191</sup> did a similar analysis for the CPP MR of electrochemically deposited Co/Cu nanowires against the bilayer thicknesses and found increasing MR values with decreasing layer thicknesses. The values measured in this work cannot be directly compared to this literature, but seem to be reasonable in magnitude. In general, the resistivity should decrease with increasing Cu layer thickness.<sup>136</sup>

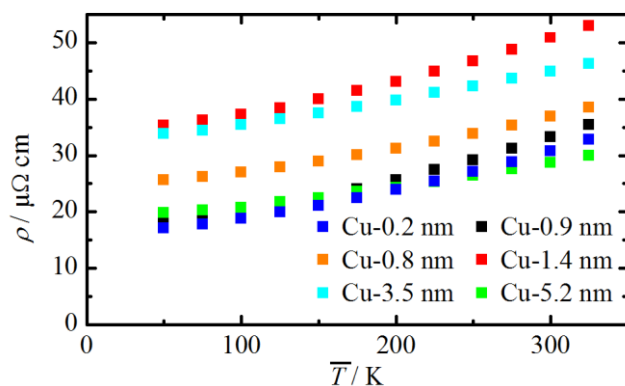


**Figure 6-2 Resistivity of the multilayered nanowires as a function of the temperature.**

Since it is difficult to directly compare the resistivity of different multilayered samples, the relative change due to an applied magnetic field—the magnetoresistance ( $\text{MR} = \rho_{\text{H}}/\rho_{0,1} - 1$ ) value—is useful to characterize the samples. It is possible to distinguish GMR and AMR effects by comparing the MR in magnetic fields parallel and perpendicular to the nanowire axis. The GMR effect is independent of the direction of the applied magnetic saturation field, but the AMR value depends on the magnetization direction in respect to the electrical current. Therefore, the dif-

ference in the saturation values corresponds to the AMR effect. In Figure 6-3 the MR behavior at RT is shown for perpendicular and parallel applied magnetic fields. The magnetoresistance effects differ significantly between the samples. According to Liu *et al.*<sup>137</sup> three regimes can be distinguished in electrochemically deposited multilayers:

- i) continuous bilayers
- ii) pinholes in the non-magnetic layer
- iii) pinholes in the magnetic layer

With continuous bilayers the typical GMR dominated behavior (samples: Cu-1.4 nm, Cu-3.5 nm, and Cu-5.2 nm; see Figure 6-3(d-f)) can be expected. Below a certain thickness, pinholes form in the Cu layer and direct exchange coupling leads to a permanent parallel alignment of the magnetic layers. As a result, the GMR effect vanishes and only the AMR effect remains (samples: Cu-0.2 nm and Cu-0.9 nm; see Figure 6-3(a-b)). The AMR ratio is expected to be smaller compared to bulk, due to the additional resistance of the non-magnetic layers and interfaces. For pinholes in the magnetic layer, the so called superparamagnetic magnetoresistance (SPM) occurs due to ferromagnetic islands in the non-magnetic matrix.<sup>128,137,192</sup> These ferromagnetic nanoparticles interact with spin polarized currents and show GMR effects. Their paramagnetic behavior above the blocking temperature leads to an almost linear magnetic field dependence of the magnetoresistance. The typical SPM behavior is not observed, as expected due to the high thickness of the magnetic layers in the investigated samples. Hence, the MMR dominates above the saturation field.\* The AMR effect dominates in sample Cu-0.2 nm and Cu-0.9 nm. The almost bulk-like AMR value above 4 % indicates small additional resistances of Cu layers and interfaces and most magnetic layers are interconnected through the non-magnetic layer. The saturation field of the Cu-3.5 nm sample is around 0.5 T in perpendicular direction and the curves in Figure 6-3(e) show only a fraction of the full effect. In the cryostat setup, higher magnetic fields are available and AMR effects of -1 % and GMR effects of -15.4 % are measured for the Cu-3.5 nm sample, which indicate a high interface resistance and closed layers. The Cu-0.8 nm, Cu-1.4 nm, and Cu-5.2 nm samples show a clear GMR contribution with smaller AMR contributions, which indicates mostly closed layers. The samples with significant GMR contributions Figure 6-3(d-f) deviate from the typical behavior of electrochemically deposited multilayered films of increasing GMR ratios with decreasing Cu layer thickness.<sup>136,189</sup> This is expected

---

\* However, it is generally challenging to distinguish SPM and MMR contributions since both are almost linear with the magnetic field.

due to different magnetic layer thicknesses and compositions. Our perpendicular magnetoresistance values at RT are between -3.9 % for Cu-0.2 nm, -3.6 % for Cu-0.8 nm, -3.6 % for Cu-0.9 nm, -9.3 % for Cu-1.4 nm, -15.4 % for Cu-3.5 nm, and -11 % for Cu-5.2 nm, while the record values for electrodeposited Co-Ni/Cu multilayered nanowires is -35 %<sup>\*</sup>.<sup>58</sup> To achieve these high magnitudes smaller diameters and continuous bilayers below a thickness of 7 nm are necessary.

---

\* Evans *et al.* specify the  $MR_{inf}$  values of -55 %, which is translated to the given MR values.

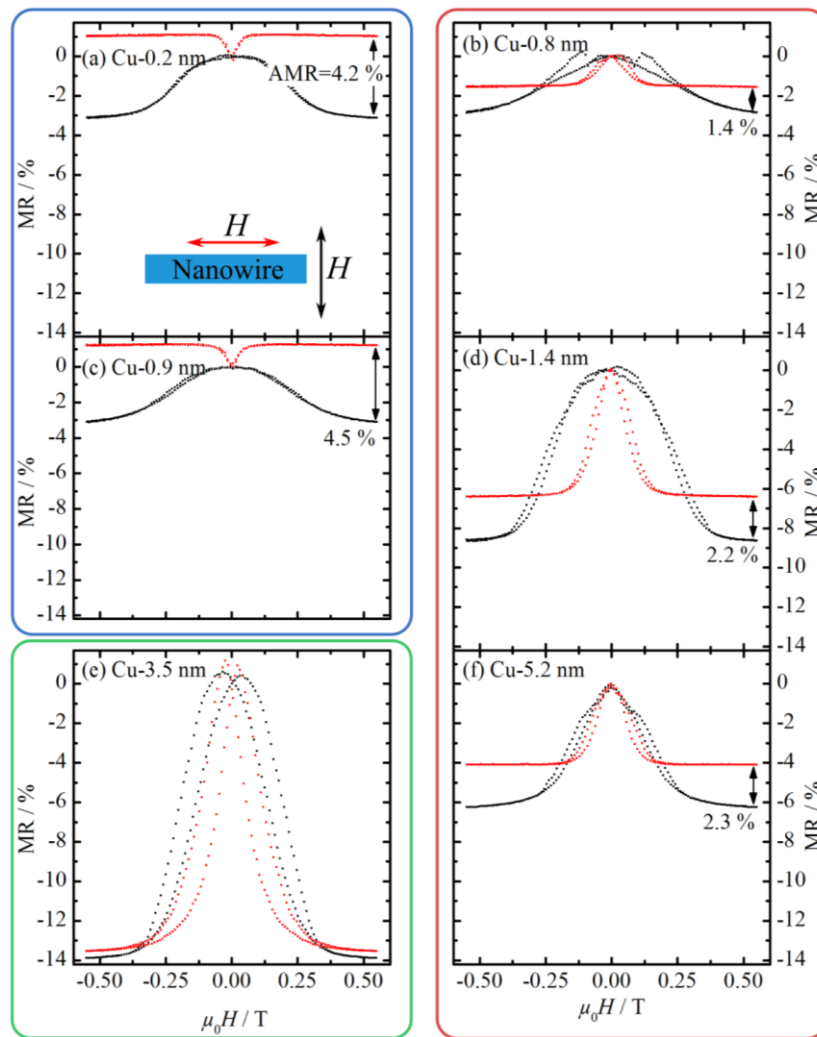


**Figure 6-3** MR of the Co-Ni/Cu multilayered nanowires in parallel and perpendicular direction of the magnetic field in reference to the nanowire axis (electrical current direction) at RT. The samples in the blue boarder show AMR dominated behavior due to pinholes in the non-magnetic layers. The samples in the red boarder, show significant GMR effects, due to mostly continuous bilayers and the sample in the green boarder shows a dominating GMR effect. In the perpendicular direction, the full effect size might not be achieved due to insufficient magnetic fields.

### 6.1.1 Temperature dependent MR

The temperature dependent perpendicular MR effects are shown in Figure 6-4 and display the typical temperature behavior. The GMR dominated nanowires (above 1 nm Cu layer thicknesses) display a linear behavior, while the slopes of the AMR dominated nanowires are flattening

towards lower temperatures, similar to the MR curves in the previous chapter. The difference of the general GMR magnitude of the two Cu-3.5 nm curves is probably due to aging of the nanowire, while being stored in ethanol from October 2011 to the measurement in July 2013. A measurement in October 2013 showed comparable effect sizes at RT and confirms the aging effect. Measurements in March 2014 show MR values of 5 % at RT and a semiconducting temperature behavior, which indicates an oxidation of the nanowire.

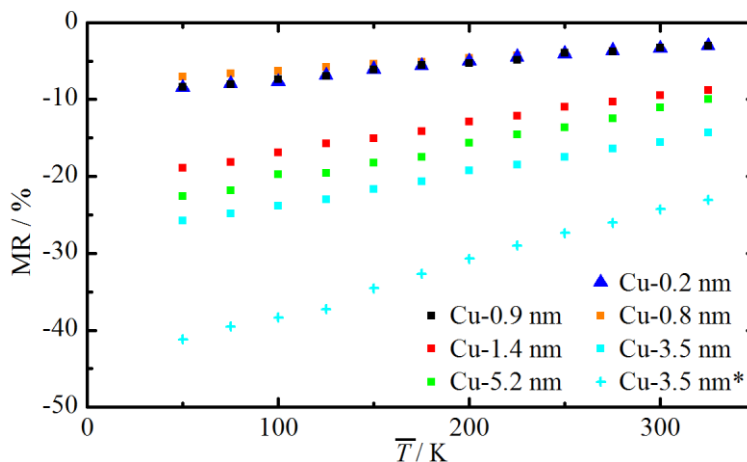


**Figure 6-4** Temperature dependent MR of the multilayered nanowires perpendicular magnetic fields. The samples above 1 nm Cu layer thicknesses show dominating GMR behavior. \*This data is measured two years earlier than the second Cu-3.5 nm data.

## 6.2 Magneto-Thermopower

The thermopower or Seebeck coefficient of a multilayered nanowire can be described by the so called Nordheim-Gorter rule (section 2.2.3) as a series of Co-Ni and Cu elements.\* The compositions and geometries given in Table 6-1 are used for the theoretical calculation. In addition, the thermopowers of Co-Ni alloy nanowires (see previous chapter), literature values of  $S_{\text{Cu}}$ <sup>44</sup> and the resistivities<sup>74</sup> are used to apply the Nordheim-Gorter rule. The estimated thermopower values in reference to platinum increases with decreasing Cu layer thicknesses from  $-17 \mu\text{VK}^{-1}$  to  $-25 \mu\text{VK}^{-1}$ , for two reasons: The decreasing ratio of Cu to Co-Ni and—more importantly—the change of Co compositions of magnetic layer from 30 % to 50 % ( $S_{\text{Co-Ni}}$  changes from  $-18 \mu\text{VK}^{-1}$

\* A similar calculation using the Nordheim-Gorter rule is published for the CIP geometry by Nishimura *et al.*<sup>188</sup> as well as the CPP geometry by MacDonald on page 106<sup>196</sup> and by Gravier *et al.*<sup>172</sup>

to  $-24 \mu\text{VK}^{-1}$  at RT). The thermopowers, determined in this work, vary at RT between  $-15 \mu\text{VK}^{-1}$  and  $-24.5 \mu\text{VK}^{-1}$ . These values fit well to the calculation as shown in Figure 6-5. For some measurements the RT values are extrapolated from low temperature values, due to errors in the determination of  $\Delta T$  at RT, as shown in Figure 6-6.

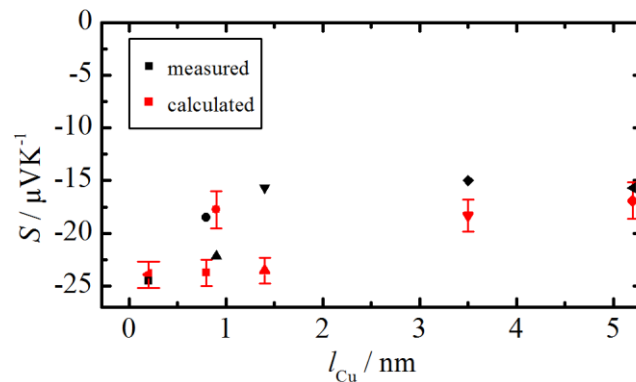


**Figure 6-5 Measured Seebeck coefficients and calculated values from Cu thicknesses determined from TEM-EDX data with errors due to 5 % uncertainty of the Co-Ni composition.**

### 6.2.1 Temperature Dependent Thermopower

The thermopower shows a monotonic increase with the temperature (shown in Figure 6-6) as expected for most metals due to a single type of charge carrier and dominating diffusive thermopower.<sup>68</sup> For comparison to literature, the Nordheim-Gorter rule (section 2.2.2) is used to calculate the theoretical absolute thermopower for Co/Cu and Ni/Cu multilayers by combining bulk values of Co, Ni, Cu, and Pt.<sup>9,44,72,85,165</sup> Since the composition has a stronger influence than the layer thicknesses the calculations are done for a constant layer thickness ratio between the magnetic and non-magnetic layers of 5:1 (the samples have ratios between 2:1 and about 80:1; see Figure 6-5 for the calculation for each geometry at RT). Most measurement values align between the theoretical values, although higher values would be perfectly reasonable, since Co-Ni alloys achieve higher thermopowers than pure Co. It seems that the deviating Cu content shifts the Cu-0.9 nm curve upwards and the Cu-3.5 nm curve downwards more than anticipated. The phonon-drag peak around 75 K in the literature curves is related to the bulk Pt literature and not observable in the nanowire measurements. This is expected due to size effects as discussed later. The deviation above 150 K from the linear behavior of  $S$  for some samples can be attributed to measurements artifacts. These artifacts are occasionally observed in the alloy nanowire measurements as well. Detailed evaluation of the thermometer data reveals that the cold thermometer is the source of these deviations. It seems that the film thickness of

the electrical contact structure is too thin to achieve low ohmic contacts over the intersecting nanowire on the cold side. While on the hot side the nanowire is ending within the thermometer—leaving a connection around the nanowire, as shown in Figure 4-2. Therefore, the cold thermometer data of sample Cu-0.9 nm and Cu-5.2 nm is substituted by the temperature data of sample Cu-1.4 nm, which is successfully measured. To consider different thermometer resistance the data is scaled to fit the low temperature region. Where it was possible, the faulty data is substituted by thermometer data of a comparable device and scaled to fit the low-temperature region.

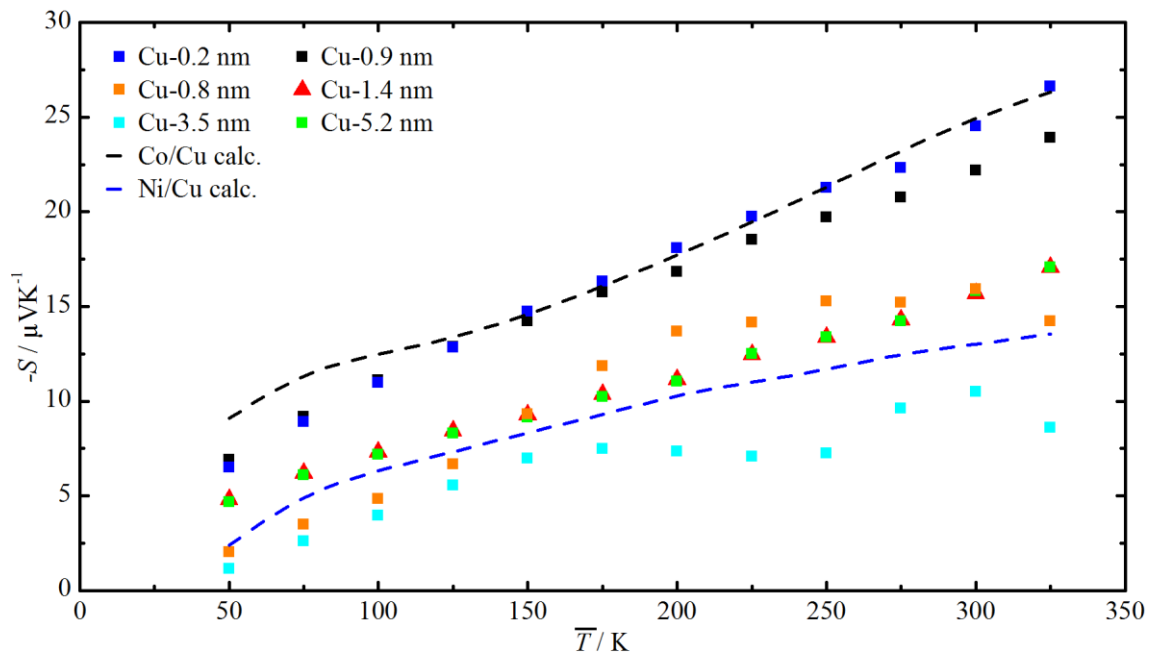


**Figure 6-6** Temperature dependent thermopower of the multilayered nanowires and calculated Co/Cu and Ni/Cu multilayers values with a layer thickness ratio of 5:1 using literature bulk data for  $S_{\text{Co}}$ ,  $S_{\text{Ni}}$  and  $S_{\text{Cu}}$ .

### 6.2.2 Magneto-Thermoelectric Power–MTEP

At each temperature step, the magnetic field dependence of the thermopower is measured and the MTEP value is calculated. The RT values of the MTEP are 2.7 % for Cu-0.2 nm, 4.2 % for Cu-0.8 nm, 3.5 % for Cu-0.9 nm, 14.7 % for Cu-1.4 nm, 29.1 % for Cu-3.5 nm, and 14.5 % for Cu-5.2 nm. This is the first time the thermopower of Co-Ni/Cu multilayers is measured; the results are comparable to the values of Co/Cu multilayered nanowires, which range between 5 % and 32 %.<sup>31,32,171-173,188,193</sup> The measured MTEP have a higher magnitude than the MR, which is in agreement with most CIP nanowire literature and CPP thin film literature.<sup>31,171-173,193</sup> On the contrary, two publications on CIP thin film measurements show the opposite behavior with

higher MR than the MTEP.<sup>32,188</sup> Kobayashi *et al.*<sup>194</sup> studied the difference between CIP and CPP measurements on the same sample and found no systematic difference between the measurement directions.\* Therefore, this variation in literature might not be due to the alignment of the current with respect to the multilayers, but due to the used contact materials and measurement setup.

The MTEP (see equation (2.2-17)) depends on the thermopower of the electrical contacts. Because Co/Cu and Co-Ni/Cu multilayers have negative Seebeck coefficients, positive/negative absolute Seebeck coefficients of the electrical contacts  $S_{\text{contact,abs}}$  will lead to decreased/increased MTEP values compared to the MR.<sup>†</sup> This behavior is described in the previous chapter on alloy nanowires. In publications that specify the contact material the decreased/increased MTEP values seem to correlate with the positive/negative  $S_{\text{contact,abs}}$ . Shi *et al.*<sup>32</sup> used Fe as a contact material and measured decreased MTEP values. Gravier *et al.*<sup>31,171-173</sup> states systematically too low Seebeck coefficients in their measurements, which explains the repeatedly observed increased MTEP value.<sup>195</sup>

The absolute change of the Seebeck coefficient  $\Delta S$  due to the magnetic field is higher for the multilayered nanowires than for the Co-Ni alloy nanowires, namely between  $0.66 \mu\text{VK}^{-1}$  and  $4.4 \mu\text{VK}^{-1}$ .  $\Delta S$  is independent of the contact material and a useful property to compare magneto-effect of different materials. The highest  $\Delta S$  values of around  $8 \mu\text{VK}^{-1}$  at RT are measured by Shi *et al.*<sup>32</sup> and Nishimura *et al.*<sup>188</sup> on sputtered Co/Cu thin films with a non-magnetic layer thickness of 1 nm. These films showed CIP GMR effects of about 50 %.

### 6.2.3 Temperature dependent MTEP

The temperature dependent MTEP of the different samples is shown in Figure 6-7. Above 200 K the measured MTEP is similar in absolute magnitude to the magnetoresistance, but at lower temperatures the samples can be arranged into two groups. The MTEP of the Cu-0.8 nm and the Cu-3.5 nm samples continuously increases with decreasing temperature, while the other samples reach a maximum around 180 K. In the case of the Cu-3.5 nm nanowire both behaviors occur, which confirms that the deviation is not due to the nanowires themselves. As described in section 2.2.4, the MTEP includes the thermopower of the electrical contact structure. Due to inconsistencies of the sputtering setup, the electrical contact structure of the Cu-0.8 nm and

---

\* More precisely the current-at-angle-to-plane contribution was measured, which involves a CPP contribution.

† Fe, Au, Cu are positive at RT, while Pt is negative (see Table 2-1).

the Cu-3.5 nm samples incorporated Cr, which is already known to diminish the phonon-drag in Au.<sup>196</sup> As shown by Huebener,<sup>41</sup> the phonon-drag causes the absolute thermopower of Pt to cross zero around 180 K and reach a maximum around 70 K. Although no phonon-drag related peak is observed in the thermopower measurements, the Pt contacts still lead to a maximum of the MTEP at 180 K by decreasing/increasing the measured thermopower at lower/higher temperatures. In other words, the thermopower of the Pt contacts still shows the typical zero crossing between 150 K and 200 K. With the Cr impurities, this zero crossing seems to be suppressed and the thermopower of Pt-Cr adds an approximately constant increase to the MTEP value.\*

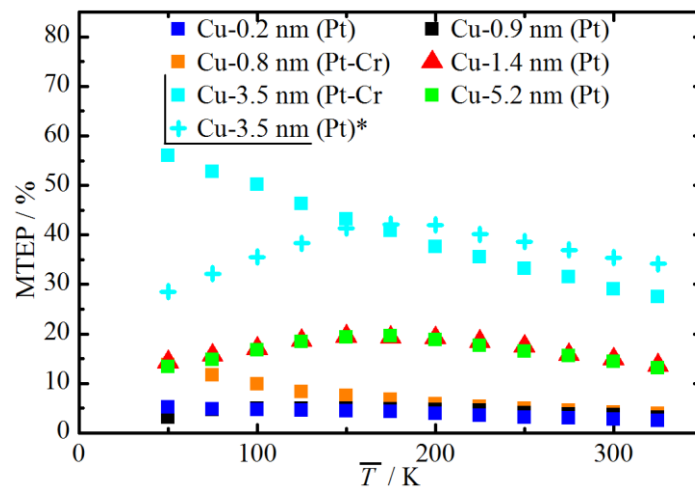


**Figure 6-7 Temperature dependent MTEP of the multilayered nanowires in perpendicular magnetic fields. Some curves show a characteristic maximum, while others decrease monotonic. This is due to the influence of different contact materials. The samples with dominating AMR effects (Cu-0.2 nm, Cu-0.8 nm, and Cu-0.9 nm) show low MTEP values. \* This sample is measured two years earlier than the second Cu-3.5 nm sample.**

The thermoelectric power factors  $PF=S^2\sigma$  are calculated at zero field and above the saturation field. The samples with dominating AMR effects (Cu-0.2 nm, Cu-0.8 nm, and Cu-0.9 nm) typically show higher PF values with lower magnetic effects, as expected from the thermopower behavior. The PFs are comparably small and the highest values are around the PF of the Ni nanowire discussed in the previous chapter. Nevertheless, the PFs are still higher than published  $\text{Bi}_2\text{Te}_3$  nanowire values,<sup>175</sup> which might pave the way for energy harvesting applications in the

\* The difference of the MTEP magnitude of the two Cu-3.5 curves is probably due to aging of the samples, as discussed on the GMR results.

future. Under specific conditions, it is likely that more heat power is converted by high PF materials than by high efficiency (high ZT) materials and in this case high PF materials are advantageous. The highest magneto-power factors are achieved in the Cu-3.5 nm nanowire with 40 % at RT. In literature MPF of over 200 % at RT are reported on sputtered Co/Cu thin films.<sup>32</sup>

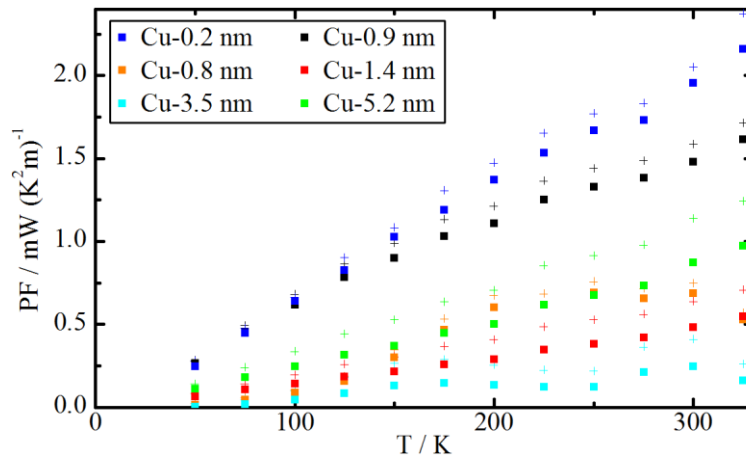


**Figure 6-8** The thermoelectric power factor  $PF=S^2\sigma$  of the devices in zero field (squares) and saturation (crosses) including the thermopower of the electrical contacts.<sup>9,10,85</sup>

### 6.3 The Mott Formula— $S$ vs. $R^{-1}$

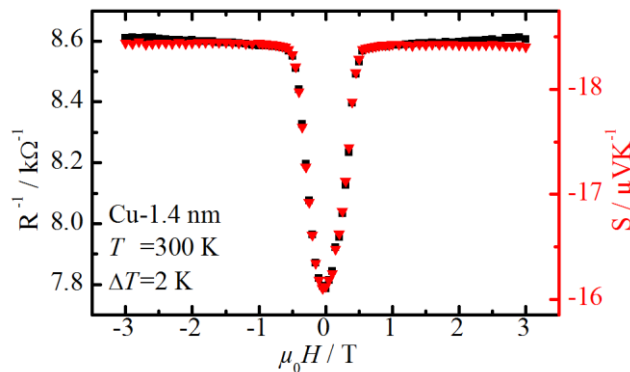


**Figure 6-9** Conductance and corresponding thermopower curves of the Cu-1.4 nm sample at RT and  $\Delta T$  of 2 K.

From the data, a strong correlation between thermopower and resistance in the magnetic field is again observed.  $S$  and  $R^{-1}$  at RT are shown in Figure 6-9 and clearly display a proportional behavior below the saturation field. The diffusive thermopower depends on the electrical conductivity, as described by the Mott formula (2.2-21), and the magnetic field dependency of the thermopower is a direct result of the MR effect. A linear relation between  $S$  and  $R_{\text{res}}^{-1}$ , with  $R_{\text{res}}$

being the residual resistance, was first found by Nordheim, Gorter, and Gold<sup>84,88</sup> with the impurity concentration as an implicit variable. Conover *et al.*<sup>36</sup> then predicted equal MTP and MR magnitudes and attempted to verify this experimentally. The Seebeck coefficient is correlated to the conductance in Figure 6-10. The linear slope increases with temperature while the offset on the y-axis decreases. From the linear fit of  $S$  as a function of  $\bar{T} \cdot R^{-1}$  at each temperature, the energy derivative can be calculated from the slope (see Figure 6-11) and  $S_{\text{offset}}$  can be extracted from the offset (see Figure 6-12). A temperature dependent increase of the slope is published on Co/Cu multilayers by Baily *et al.*<sup>193</sup> and by Shi *et al.*,<sup>32,35,90</sup> on Cu/Co/Cu/Ni-Fe multilayers by Kobayashi *et al.*,<sup>194</sup> and on Fe-Ag granular alloys by Sakurai *et al.*,<sup>34</sup> which are compared to our results in Figure 6-11. Figure 6-12 shows  $S_{\text{offset}}$  as a function of the temperature and the literature value of the absolute  $S_{\text{Pt}}$  (Roberts *et al.*<sup>9</sup> above 270 K and Moore *et al.*<sup>85</sup> below 270 K). To obtain these literature values, the Seebeck coefficient of Pt is measured against a superconducting materials at low temperature. Above the critical temperature, the Seebeck coefficients are calculated from the measured Thomson coefficients. Roberts *et al.*<sup>9,197,198</sup> explained this technique in detail. In order to keep the reference measurements consistent, only samples of highest purity are investigated.

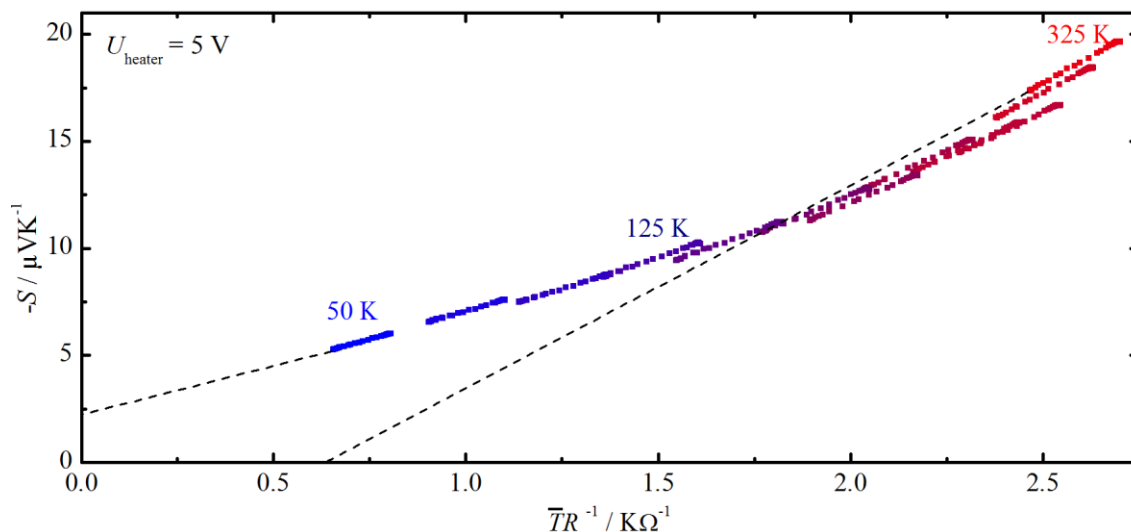


**Figure 6-10** Seebeck coefficient versus the conductance of the Cu-1.4 nm sample in 25 K steps from 50 K to 325 K is shown with the applied magnetic field as an implicit variable (scaled by the average temperature in order to display data of the wide temperature range). For simplicity only data for  $U_{\text{heater}}=5$  V is shown, which corresponds to a  $\Delta T$  of 3 K at 25 K and 2 K at 325 K.

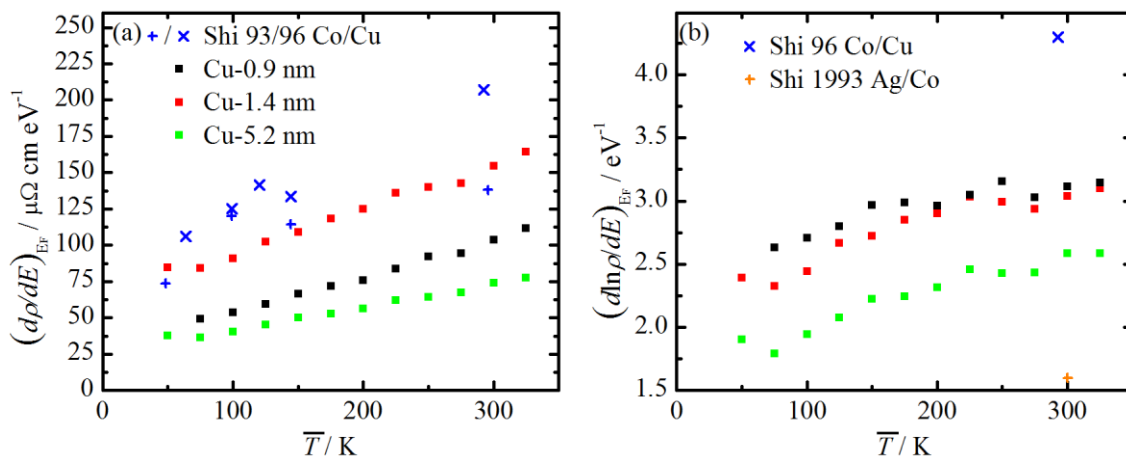


Figure 6-11 (a) Derivative of the resistivity of the energy at the Fermi energy derived from equation (6.3-2), which is proportional to the slopes in Figure 6-10. (b) Derivative of the logarithm of the resistivity of the energy, which is equivalent to the data in (a) normalized by the resistivity.<sup>32,35,94</sup>

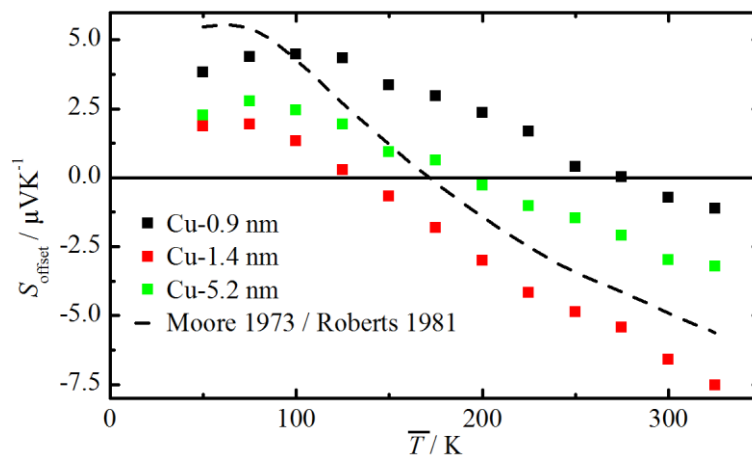
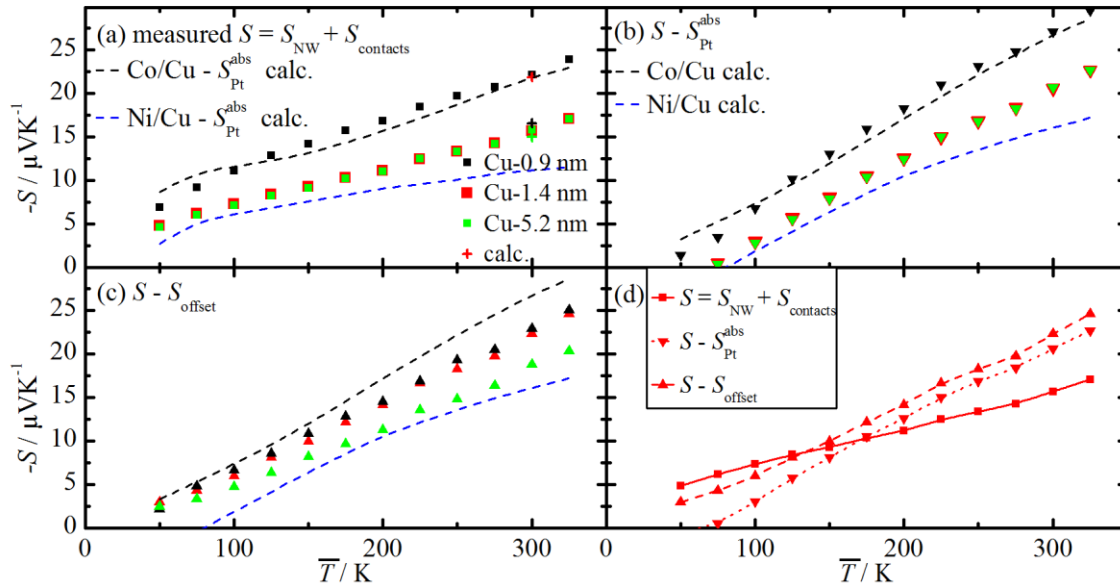


Figure 6-12 The offset from equation (6.3-2), which is the offset shown in Figure 6-10. The absolute literature values for Pt are displayed for comparison.<sup>9,85</sup>

The next step is to compare MTP and MR similar to Conover *et al.*<sup>36</sup> For the conversion of MTEP values into MTP values a correction of the absolute thermopower of Pt is necessary. To evaluate the application of this correction by the bulk literature value of  $S_{\text{Pt}}$ ,<sup>9,85</sup> the measured thermopowers of three nanowires and the corrected values are shown in Figure 6-13(a-b). This correction shifts each curve by a fixed value, and changes the curvature in opposite direction. This suggests a positive phonon-drag or magnon-drag contribution similar to the results for Ni bulk of Farrell *et al.*<sup>199</sup> In general, Co, Ni, and Cu bulk materials show a phonon-drag contribution at around 70 K, which is decreased in Ni bulk materials by adding Co impurities as Farrel *et al.* have shown.<sup>199</sup> In nanostructured materials, phonon transport is restricted—hence, the

phonon-electron scattering probability is reduced—which typically leads to negligible phonon-drag thermopower in electrochemically deposited materials.<sup>16,167,168,200</sup> Thus, all measured nanowires in the previous chapter show no phonon-drag effects. The magnon-drag effect is proven to be negligible in Ni and most likely negligible in Co.<sup>42,167,168</sup> Overall, the deviation in Figure 6-13(b) from the linear diffusive behavior seems unreasonable and could be an artifact of the correction.



**Figure 6-13** Temperature dependent thermopower of three multilayered nanowires. The measured data—including the thermopower of the electrical contacts—is shown in (a). The absolute thermopower corrected by subtracting literature values for  $S_{Pt}^{9,85}$  is shown in (b). The absolute thermopower corrected by subtracting  $S_{offset}$  is shown in (c). Calculated absolute values for Co/Cu and Ni/Cu multilayers are shown in (a) in reference to  $S_{Pt}$ , and absolute values in (b) and (c).<sup>9,72,165</sup> All three curves of the Cu-1.4 nm sample are shown in (d).

Due to the high sensitivity of  $S$  to impurities the materials used in ordinary measurement setups can be expected to deviate from the literature, resulting in rough estimations of the absolute Seebeck coefficients. In addition, size effects significantly suppress the phonon-drag thermopower in materials like Pt or Au.<sup>41,42</sup> Our fabrication technique of the electrical contacts requires a 15 minutes ac sputter cleaning and makes a contamination of the surface very likely. A Ti adhesion layer is sputtered prior to the Pt deposition. Both targets have a material purity of 99.95 %. The influence of a parallel circuit of the Ti and the Pt layer can be estimated by the

Two-Band model (section 2.2.3) using literature values.<sup>9,85,201-203</sup> Due to the almost 30 times higher resistance of 10 nm thick Ti layer compared to 40 nm thick Pt layer the influence of the Ti layer on the Seebeck coefficient can be expected to be about +0.5  $\mu\text{V/K}$  at RT. All these arguments make the determination of absolute thermopowers from literature values very challenging and deviations are likely.

In the following, a new approach to obtain the absolute thermopower of the electrical contacts is proposed. The measured Seebeck coefficients are in reference to the contact material, while the resistance measurements results in the electrical resistivity of only the nanowire. Any magnetic field dependence of the measured Seebeck coefficients  $S_{\text{measured}}$  is due to the nanowire. Although this allows magnetic field independent parts of  $S_{\text{NW}}(H)$ , the Mott formula (2.2-21) predicts that the magnetic field dependence of the Seebeck coefficient is proportional to the nanowire conductivity  $\rho_{\text{NW}}(H)^{-1}$  at any given temperature.\* This can be summarized in the following two formulas for the measured Seebeck coefficients:

$$S_{\text{measured}}(H) = S_{\text{NW}}(H) - S_{\text{contact}} \quad (6.3-1)$$

$$= -cT \left( \frac{d\rho}{dE} \right)_{E=E_f} \rho_{\text{NW}}(H)^{-1} - S_{\text{offset}} \quad (6.3-2)$$

with  $c = \pi^2 k_B^2 / 3q$ , with the charge of the charge carrier  $q$ .

In general, the offset of the Seebeck coefficient  $S_{\text{offset}}$  determined from the linear fit can arise from the following thermopower contributions:

- i) The thermopower of the electrical contacts ( $S_{\text{contact}}$ ),
- ii) non-diffusive thermopowers of the sample (drag effects), and
- iii) a deviation from the linear behavior of  $S(\rho^{-1})$  outside of the observed range (energy derivative of the resistivity).

In the investigated samples, the linear temperature behavior of the Seebeck coefficient suggests a dominating diffusive behavior. In pure Co, Ni, and Cu, the non-diffusive contribution to the total thermopower can be significant below 100 K. However, in the polycrystalline nanowires this non-diffusive thermopower can be excluded, as discussed previously. Hence, point (ii) can be neglected. In the observed magnetic field range the  $S(\rho^{-1})$  behavior is linear and the

---

\* This is valid for identical temperature profiles during thermopower and resistivity measurement.

energy derivative seem to be magnetic field independent, as discussed in section 2.2.5 and stated in literature several times. Therefore, point (iii) is carefully rejected leaving only point (i). For this material system  $S_{\text{contact}} \triangleq S_{\text{offset}}$  follows and as already predicted for Fe-Cr by Conover *et al.*<sup>36</sup> it follows:

$$\text{MTP} = \frac{S(H) - S_0}{S_{\text{NW},0}^{\text{abs}}} = -\frac{R(H) - R_0}{R(H)} = -\text{MR}_{\text{inf}}. \quad (6.3-3)$$

By comparing MTP to  $\text{MR}_{\text{inf}}$  or  $S_{\text{contact}}$  to  $S_{\text{offset}}$  a quantitative statement about the previous assumptions can be made. The other way around, this model can be applied to calculate the absolute thermopower of the electrical contacts by  $S_{\text{contact}} \triangleq S_{\text{offset}}$ . The temperature behavior of  $S_{\text{offset}}$  agrees qualitatively to the bulk Pt literature values, as shown in Figure 6-12, but of the Cu-0.9 nm and the Cu-5.2 nm curves are shifted to positive values and as expected the phonon-drag peak is reduced in all samples. The offset of the three samples deviates from each other. Since all three electrical contact structures show very similar heating and resistance behavior, this deviation is unexpected and in contrast to the previous assumptions. It might be a sign for non-diffusive thermopower contributions of the nanowire, which is questionable close to RT. Nevertheless, using these values as  $S_{\text{contact}}$  to obtain the absolute thermopower of the nanowire—see Figure 6-13(c)—leads to a linear temperature behavior up to RT as expected for nanostructured metals. Shi *et al.*<sup>89</sup> observed also a linear behavior for Co/Ni-Cu multilayers, which should be qualitatively comparable. In comparison to the correction with Pt literature values, the correction by  $S_{\text{offset}}$  is different for each sample and removes the curvatures completely. Theoretical values of the absolute thermopower and thermopower relative to the Pt contacts for Co/Cu and Ni/Cu multilayers are calculated using bulk literature values.<sup>9,44,72,85,165</sup> Again the layer thickness ratio between the magnetic and non-magnetic segments used in the calculation is 5:1. The good agreement of the experimental values with the theoretical values is a convincing argument for the  $S_{\text{offset}}$  correction. Additionally, the thermopower at RT of each sample is theoretically calculated for the individual geometry and composition (crosses in Figure 6-13(a)).

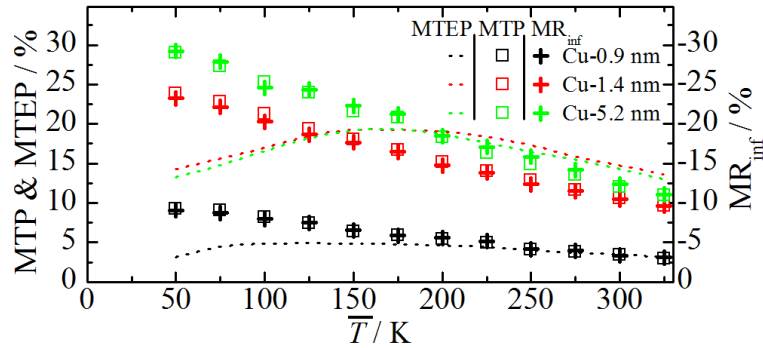


**Figure 6-14** The temperature dependent  $MR_{inf}$ , MTEP and MTP, which are corrected under the assumption of  $S_{contact} \triangleq S_{offset}$  and values. The MTEP is influenced by the contact material, while the MTP and the 4-point MR are independent of the contact material. The relation between MTP and  $MR_{inf}$  according to equation (6.3-3) is observed.

Applying that  $S_{contact} \triangleq S_{offset}$ , the MTP is evaluated and plotted in Figure 6-14. According to equation (6.3-3) the absolute values of MTP and the  $GMR_{inf}$  (as well as the  $MTP_{inf}$  and the MR) are equal for this material system. To illustrate the importance of the MTP calculation, the MTEP values are displayed as lines for comparison. In principle, any MTEP value can be measured depending on the contact material. In literature, non-monotonic temperature behavior of thermoelectric properties are often attributed to the phonon-drag or the magnon-drag of the sample,<sup>75,94,167</sup> whereas, our results show that measurement artifacts from the contact material should be carefully considered as well.

Several other coherent conclusions are based on this line of thoughts. According to equation (6.3-3), a finite MR value and vanishing  $S_{NW,0}^{abs}$  results in a vanishing  $S(H) - S_0$ . Additionally, a sign change of  $S_{NW,0}^{abs}$  induces a sign change of  $S(H) - S_0$ , which are exactly the result of one of the first MTEP publication from Piraux *et al.*<sup>91</sup> According to the Mott formula, the sign of  $S$  is given by the charge of the carriers and the energy derivative of the resistivity. In metals with negative magnetoresistance the MTP is positive, which requires the same signs of  $S_{NW,0}^{abs}$  and  $S(H) - S_0$ .

#### 6.4 Conclusion Co-Ni/Cu Multilayered Nanowires

For the first time, thermopower measurements on electrochemically deposited multilayered nanowires are presented. The high aspect ratio of the individual Co-Ni/Cu nanowires enables us to measure the current-perpendicular-to-plane GMR effect and the CPP magneto-thermopower. Using TEM and SEM, the geometries and layer thicknesses of the nanowires are determined. The calculated resistivities of the nanowires are about a factor of two higher than the values of Co-Ni alloy nanowires. MR measurements in parallel and perpendicular magnetic fields show that the Cu spacers with a thickness below 1 nm are not continuous and display almost negligible GMR effects. Samples with thicker Cu layers exhibit GMR effects between -9 % and -25 % at RT. The calculated theoretical Seebeck coefficients are in good agreement to the measurement results, considering the Seebeck coefficients of Co-Ni alloys as determined in the previous chapter. The temperature dependent magneto-thermopower as well as magnetoresistance are measured in perpendicular magnetic fields and resemble published literature data. A linear dependence of the thermopower and electrical conductivity of the nanowires with the magnetic field as an implicit variable is verified over a wide temperature range. This observation is in agreement with the Mott formula under the assumption of a magnetic field independent thermopower offset. This offset directly relates to the absolute Seebeck coefficient of the contact materials and is removed to obtain the absolute thermopower of the samples. The resulting absolute thermopower values seem more reliable than data obtained by the correction of literature values of the contact material. The calculated MTP is equal to the MR, as predicted by Conover *et al.*<sup>36</sup> Additionally, the energy derivative of the resistivity in the Mott formula is calculated, which can be correlated to the transmission function serving as a starting point in theoretical models, as recently published by Popescu and Kratzer.<sup>204</sup> They theoretically predict significant quantization effects in a ferromagnetic layer with a thickness below 1 nm, which change the transmission function of the minority spin channel. In addition, this quantization adds a strong anisotropy effect to the magneto-thermopower and magnetoresistance. Unfortunately, electrochemical deposition techniques seem to be unreliable in this thickness range, but this work convincingly shows the importance of the energy derivative of the resistivity for tailoring thermoelectric properties.

## 7 Conclusion

The aim of this thesis is to investigate experimentally the relationship between thermopower and electrical conductivity in ferromagnetic nanostructures. The Mott formula predicts a clear relation between the diffusive thermopower and the resistance in the magnetic field, while experimental results often show deviations. Ferromagnetic nanowires are electrochemically deposited into nanoporous alumina membranes with pore diameters around 200 nm. Magnetometry and structural analysis are conducted on individual Co-Ni alloy and Co-Ni/Cu multilayered nanowires with aspect ratios—ratio of length to width—as high as 150:1. A laser lithography process is adopted to pattern electrical contacts to single nanowires on a substrate. Furthermore, a versatile measurement setup is developed to measure the magnetoresistance and the thermopower in perpendicular magnetic fields up to 9 T, temperatures between 2 K and 400 K, and temperature gradients up to 20 K.

Co-Ni alloy nanowires with varying compositions are investigated. Below 50 % Co content a defined uniaxial magnetization behavior is found. The resistivities at RT are 13.2  $\mu\Omega\text{cm}$  for Ni and around 20  $\mu\Omega\text{cm}$  for the Co-Ni alloys, which is a factor of two higher than literature values of annealed bulk, as expected for electrodeposited materials. The AMR values of the individual nanowires reach a maximum of 6 % at RT in agreement with bulk literature. The measured Seebeck coefficients of the individual nanowires are between  $-16 \mu\text{VK}^{-1}$  and  $-29 \mu\text{VK}^{-1}$  and match those reported for Co and Ni bulk values in the literature. Ni-rich compositions show a linear relationship between thermopower  $S$  and the electrical conductivity  $\sigma$  as a function of the magnetic field, as expected from the Mott formula, which describes the diffusive thermopower contribution. Non-diffusive contributions—magnon-drag and phonon-drag—seem to be negligible in the investigated samples. The Co-richest (71 % Co) nanowires display a distinct non-linear behavior. This might be caused by the complex magnetization configurations in combination with magnon contributions or domain wall related effects. Further investigation of these deviations might give valuable information about the influence of magnons and domain walls on the thermopower and conductance.

To further investigate the linear behavior between  $S$  and  $\sigma$ , Co-Ni/Cu multilayered nanowires are investigated, which are a unique model system to observe perpendicular-to-plane magnetotransport. These nanowires exhibit MR effects of up to -25 % at RT. The Seebeck coefficient of electrochemically deposited multilayered nanowires is measured successfully. Utilizing SEM and TEM analysis, the geometry and composition of the multilayers is determined. Theo-

retical thermopowers of the samples are calculated using the previously acquired thermopowers of Co-Ni alloys. The measured values in the range of  $-15 \mu\text{VK}^{-1}$  to  $-24.5 \mu\text{VK}^{-1}$  at RT are in convincing agreement with the calculated values in the range of  $-17 \mu\text{VK}^{-1}$  to  $-25 \mu\text{VK}^{-1}$ . The linear behavior between  $S$  and  $\sigma$ —with the magnetic field as an implicit variable—is verified. Based on this behavior, a simple model is proposed to separate the diffusive thermopower of the sample from a magnetic field independent thermopower offset, without relying on literature values. This offset directly relates to the absolute Seebeck coefficient of the contact material, disregarding non-diffusive thermopower contributions, and agrees qualitatively to the literature values of the absolute thermopower of the contact material. Additionally, the MTP values, and the energy derivative of the resistivity are calculated as a function of temperature. In accordance with the model, equal magnitude of  $\text{MR}_{\text{inf}}$  and MTP values follow. In the contrary (thus minimizing the contribution of the electrical contacts), the model can be used to quantify the non-diffusive thermopower contribution of samples with deviations from the Mott behavior.

The thermoelectric power factor, which is proportional to the power output of the material used in a thermoelectric generator, is calculated and compared to typical thermoelectric materials. The Co-Ni alloys exhibit an—by a factor of two—increased power factor as compared to the Ni nanowire and can be further enhanced up to 24 % in perpendicular magnetic fields. The highest power factor of  $3.7 \text{ mW/K}^2\text{m}$  is competitive with high performance thermoelectric materials like  $\text{Bi}_2\text{Te}_3$ <sup>174</sup> and exceeds  $\text{Bi}_2\text{Te}_3$  nanowires by a factor of five.<sup>175</sup> In the case of multilayered nanowires, the power factor can be tuned up to 40 % at RT as a function of the magnetic field. Although the highest power factors reach only values of the Ni nanowires, the power factors are still higher than published  $\text{Bi}_2\text{Te}_3$  nanowire values.<sup>175</sup> Applications for thermoelectric power generation often have to comply with a fixed heat flow and restricted surface area. Under these conditions, it is likely that more heat power is converted by high PF materials than by high efficiency (high ZT) materials. In specific applications, high PF materials are advantageous.

Recent theoretical predictions indicate that current-perpendicular-to-plane magnetotransport in multilayers might lead to a deviation from the Wiedemann-Franz law—constant ratio of thermal and electrical conductivity. Additional heat transfer, without charge transfer, can be expected in materials with two conduction bands—minority and majority carriers—due to the spin-Peltier effect, the spin-Seebeck effect or the interspin energy exchange, although the magnitude and measurability of the effects are questionable. In systems with thermally decoupled spin channels, these effects could potentially lead to significant out-of-equilibrium contributions. To complete the characterization of the spin caloric transport properties, thermal con-

---

ductance measurements are currently performed on multilayered nanowires. These efforts could verify the mentioned theoretical predictions. For following thermopower studies, a change of the contact material from Pt to a “low thermopower” material like Cu is recommended. By comparing the  $S_{\text{offset}}$  of identical contact materials on different samples to Cu literature values, it should be easier to differentiate contact contributions from non-diffusive contributions. Further, to investigate the magnon-drag related deviations from the Mott behavior it would be interesting to evaluate and to compare results on Fe samples to the results on phonon-drag dominated Pt. Surprisingly, no publications address size effects of the non-diffusive thermopower due to nanostructuring systematically, although a significant influence is repeatedly assumed in literature. A systematic study of phonon-drag in Pt thin films and magnon-drag in Fe thin films with varying thickness would lead to much needed results on size effects of the thermopower. A state of the art topic for further investigation is magnetic tunnel junctions. Our proposed model could help correlating the magneto-thermopower and magnetoresistance values of magnetic tunnel junctions.



## Appendix: Seebeck Measurement Software

The graphical user interface of the control software is shown in Figure 7-1. The software automatically executes sweeps and controls external devices, which is not possible otherwise. The changeable parameters are the temperature range and increment, two different magnetic fields, any amount of heater voltages, gate voltage range and increment and applied current and range of the resistance measurements. Additionally, the user can specify parameters for step wise and continuous magnetic field sweeps. A separated set of heater voltages can be specified for the highest temperature step to achieve an annealing effect and a standby temperature, which will be approached by the setup subsequent to the measurement, can be defined. The measurement mode can be chosen between thermovoltage, electrical resistance with or without heater voltages, or a preliminary method for thermal conductivity measurements via a steady state method—called “Völklein method”.<sup>23</sup>

The screenshot shows a window titled "MultiVu Scripting" with the following parameters and controls:

- Data Path + Sample:** C:\QDVersaLab\Data\Tim\Seebeck\
- Sample Name:** Probe messung1
- Cold Temperature (K) to 50:** 50
- Warm Temperatur (K) to 400:** 300
- Temperature Step Size (K) sign shows:** 25 (11 Steps)
- Waiting Time at each Step (min):** 20
- H. Field 1 (Oe) to 30000:** 0
- H. Field 2 (Oe) to 30000:** 20000
- Gate Sweep U. min (V):** off, U. max: 10, U. steps: 1
- Heater Voltage divided by space (V) to:** 0 4 6 8
- Heater Voltage at highest Tstep (V) to:** off
- Field Sweep Versalab Temperature:** off, Heater V: 10, max: 30000
- Chose measured value:** Uthermo (10  $\mu$ A), Range: 4 V
- Set T after the measurement:** off

Buttons: OK, Cancel. Status: max R = 400000. Path: C:\QDVersaLab\Data\Tim\Seebeck\Probe messung1\Probe messung1\_20130624\_1257

Figure 7-1 Graphical user interface of the control software of the Seebeck measurement setup.

## Appendix: TEM analysis

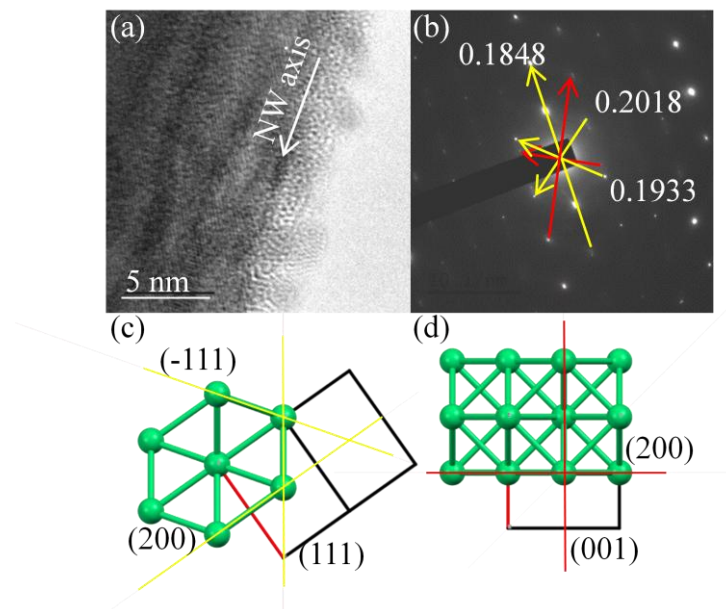
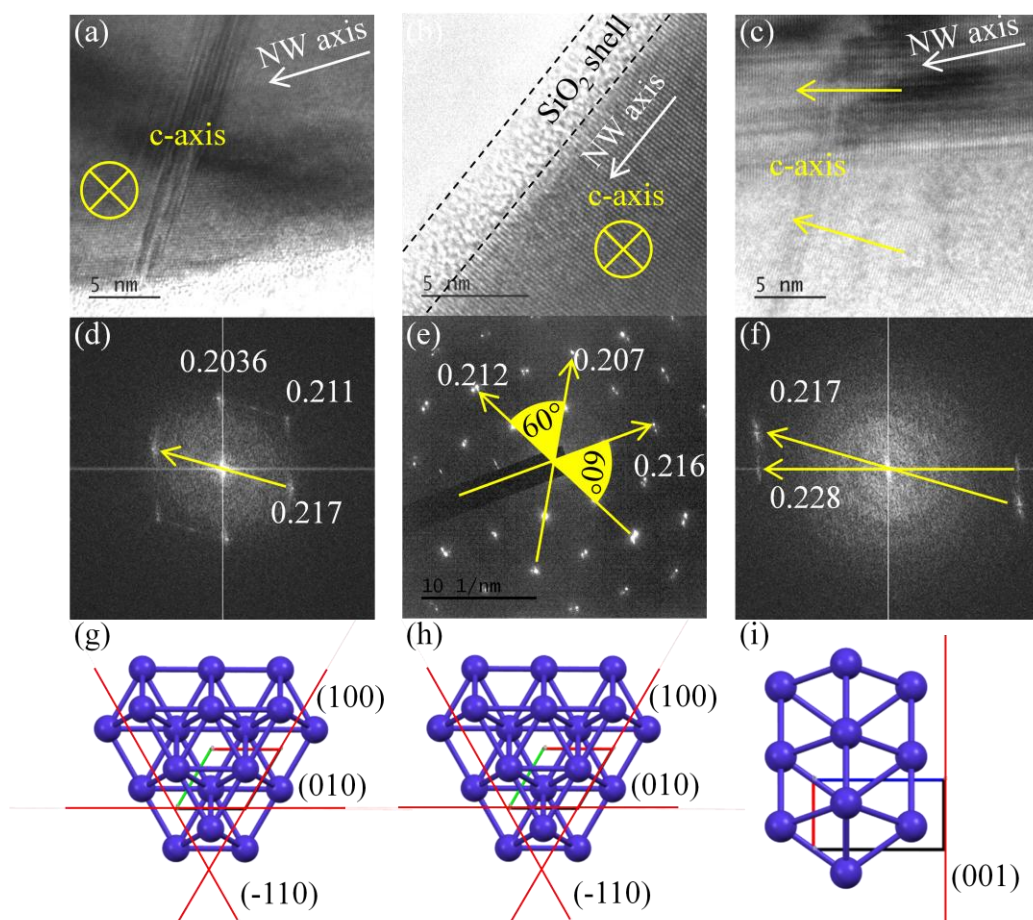


Figure 7-2 TEM of a  $\text{Co}_{0.39}\text{Ni}_{0.61}$  nanowire (a) and corresponding SAED pattern (b) with the distance of the reflexes in nm. Yellow arrows mark reflexes that are assigned to lattice planes shown in (c), while red arrows mark reflexes that can be assigned to planes shown in (d). (c) Fcc lattice along the (01-1) direction. (d) Fcc lattice along the (010) direction, with a-axis and b-axis are marked in red and green.

Table 7-1 The expected spacing between lattice planes given in miller indices (hkl) in a fcc lattice for Ni atoms and hcp lattice for Co atoms.<sup>67</sup>

(hkl)	fcc spacing / Å	hcp spacing / Å
(200)	1.772	1.086
(111)	2.046	1.198
(110)	2.506	1.254
(101)		1.916
(002)		2.034
(100), (-110)		2.171



**Figure 7-3** (a-c) Transmission electron micrographs of three  $\text{Co}_{0.71}\text{Ni}_{0.29}$  nanowires with an oxide shell of a few nanometers. The yellow markers represent the c-axis obtained from the SAED patterns shown in (d-f). (g-h) The hcp lattice along the c-axis (blue) is shown with the planes, with Miller indices (hkl) that represent the observed diffraction patterns. The a axis and b axis are marked in red and green. A sketch of an hcp lattice along the a axis is shown in (i) with the (001) plane which fits well to the observed diffraction pattern (f). (e) and (f) show several diffraction patterns, which are slightly tilted towards each other proving the polycrystalline character of the samples. The white numbers in (d-f) show the real distance of the respective reflex to the center in nm.

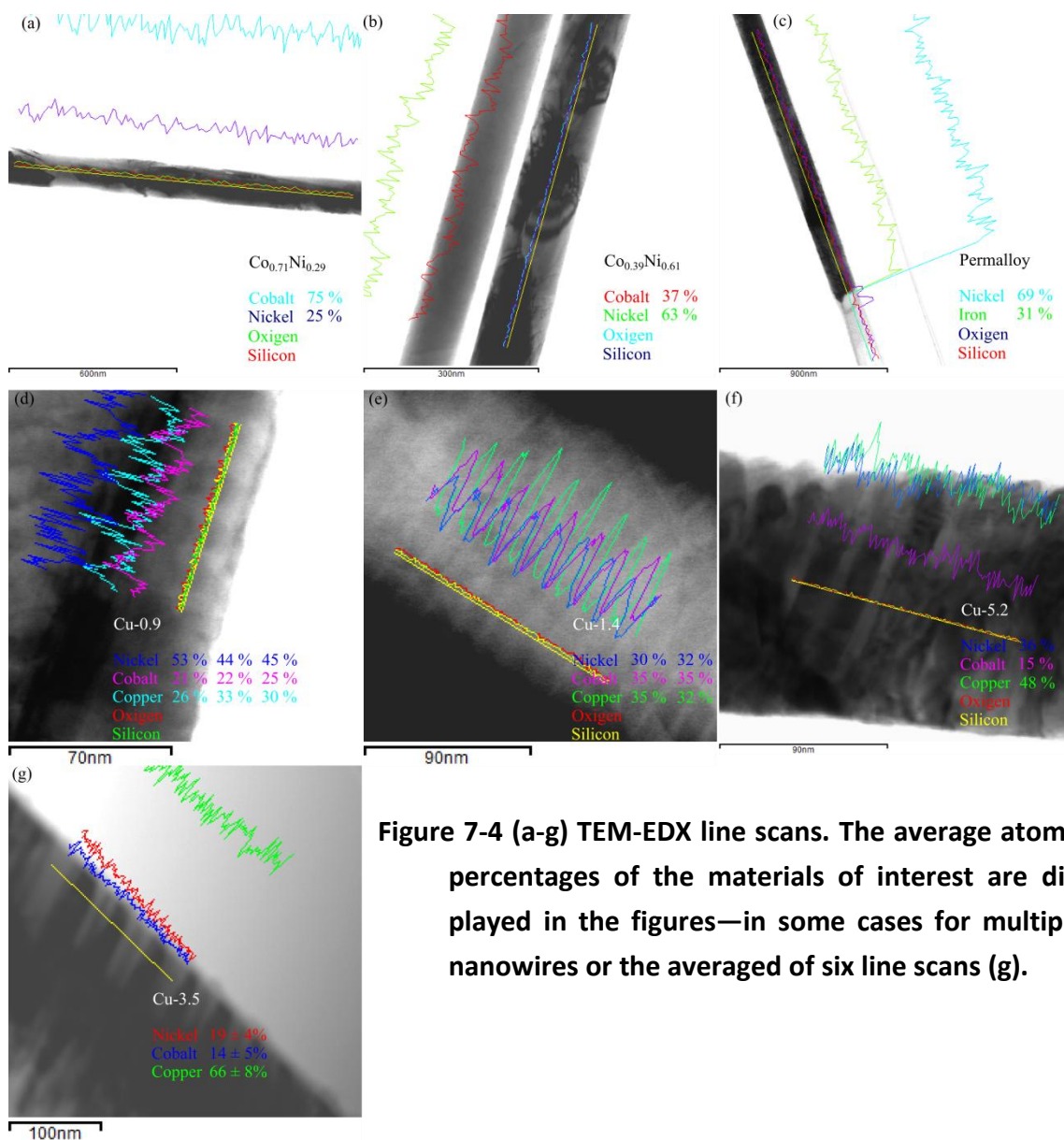


Figure 7-4 (a-g) TEM-EDX line scans. The average atomic percentages of the materials of interest are displayed in the figures—in some cases for multiple nanowires or the averaged of six line scans (g).

Table 7-2 Calculation of the layer thickness of multilayered nanowires from the composition obtained by SEM-EDX, TEM-EDX and TEM-EDX (BG), which is corrected by a Cu background of  $(27 \pm 5)\%$ .

$I_{\text{bilayer}} / \text{nm}$	Cu SEM / %	Cu TEM / %	Cu BG corr. / %	$I_{\text{Cu,SEM}} / \text{nm}$	$I_{\text{Cu,TEM}} / \text{nm}$	$I_{\text{Cu,BG corr}} / \text{nm}$
17.3		$31.4 \pm 5$	$2.9 \pm 7$		$5.2 \pm 0.8$	$0.9 \pm 2.2$
17.5		$34.6 \pm 5$	$6.0 \pm 7$		$5.9 \pm 0.9$	$1.4 \pm 1.6$
8.7	$42 \pm 5$	$69.5 \pm 8$	$41.0 \pm 9$	$3.8 \pm 0.5$	$5.8 \pm 0.7$	$3.5 \pm 0.7$
22.6		$50.3 \pm 5$	$21.8 \pm 7$		$11.0 \pm 1.1$	$5.2 \pm 1.7$

## Appendix: Hall and Nernst effect

$$\vec{E}_{\text{Hall}} = A_{\text{Hall}} \cdot \vec{j} \times \vec{B} \quad (6.4-1)$$

$$U_{\text{Hall},y} = \frac{A_{\text{Hall}}}{z} I_x B_z \quad (6.4-2)$$

$$\vec{E}_{\text{Nernst}} = N \cdot \text{grad}T \times \vec{B} \quad (6.4-3)$$

$$U_{\text{Nernst},y} = N \Delta T_x \frac{y}{x} B_z \quad (6.4-4)$$

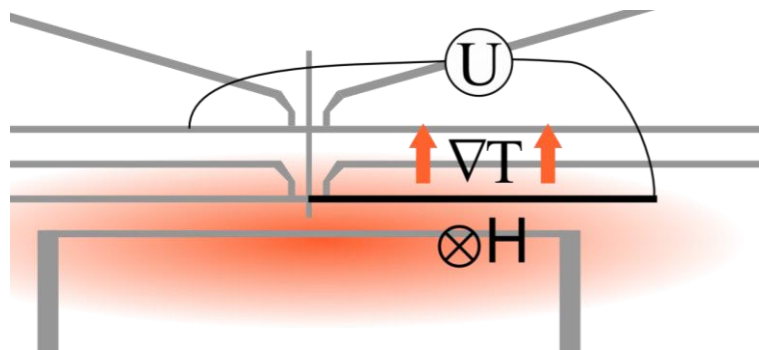


Figure 7-5 Alignment of the temperature gradient, magnetic field, and electrical contacts during a thermovoltage measurement. The highest Nernst voltage arises in the black marked part of the hot thermometer, where the temperature gradient in the electrical contacts is the highest.

## Appendix: Overview of Measurement Results at RT

**Table 7-3 Overview of the transport properties at RT of the Co-Ni alloy nanowires.**

Sample / nm	$\rho / \mu\Omega\text{cm}$	MR / %	$S / \mu\text{VK}^{-1}$	MTEP / %	MTP / %	$\Delta S / \mu\text{VK}^{-1}$
Ni	13.2	1.9	16	6.0	3.1	0.6
Co <sub>0.24</sub> Ni <sub>0.76</sub>	21.7	6.0	22	7.3	5.0	1.0
Co <sub>0.39</sub> Ni <sub>0.61</sub>	19.7	6.0	27	8.1	5.8	1.5
Co <sub>0.71</sub> Ni <sub>0.29</sub>	19.4	1.3	29	2	3.1	0.5

**Table 7-4 Overview of the transport properties at RT of the Co-Ni/Cu multilayered nanowires.**

Sample- $l_{\text{Cu}}$ / nm	$\rho / \mu\Omega\text{cm}$	MR / %	$S_{100\text{K}} / \mu\text{VK}^{-1}$	$S_{300\text{K}} / \mu\text{VK}^{-1}$	MTEP / %	$\Delta S / \mu\text{VK}^{-1}$
Cu-0.2 nm	30.62	-3.9	-11.0	-24.5	2.7	0.66
Cu-0.8 nm	28.11	-3.6	-4.8	-18.5*	4.2	0.78
Cu-0.9 nm	33.30	-3.6	-11.1	-22.2	3.5	0.78
Cu-1.4 nm	50.79	-9.3	-7.3	-15.7	14.7	2.31
Cu-3.5 nm	44.91	-15.4	-4.0	-15*	29.1	4.4
Cu-5.2 nm	67.60	-11	-7.2	-15.7	14.5	2.3

\* The 300 K values are linearly extrapolated from the low temperature behavior, due to measurement errors around RT. The uncorrected values at 100 K are displayed as well.

## Appendix: Publication List

J. Kimling, F. Kronast, S. Martens, T. Boehnert, M. Martens, J. Herrero-Albillos, L. Tati-Bisaths, U. Merkt, K. Nielsch, and G. Meier

*Photoemission electron microscopy of three-dimensional magnetization configurations in core-shell nanostructures*

Physical Review B **84**, 174406 (2011)

M. Meinert, J.-M. Schmalhorst, C. Klewe, G. Reiss, E. Arenholz, T. Boehnert, and K. Nielsch  
*Itinerant and localized magnetic moments in ferrimagnetic Mn(2)CoGa thin films probed by x-ray magnetic linear dichroism: Experiment and ab initio theory*

Physical Review B **84**, (2011)

M. Meinert, J.-M. Schmalhorst, M. Glas, G. Reiss, E. Arenholz, T. Boehnert, and K. Nielsch  
*Insights into the electronic structure of Co<sub>2</sub>FeSi from x-ray magnetic linear dichroism*

Physical Review B **86**, 054420 (2012)

S. Trtica, E. Meyer, M. H. Prosenc, J. Heck, T. Boehnert and D. Goerlitz

*Naphthalene-Bridged ansa-Nickelocene: Synthesis, Structure, Electrochemical, and Magnetic Measurements*

European Journal of Inorganic Chemistry 4486 (2012)

V. Vega, T. Boehnert, S. Martens, M. Waleczek, J. M. Montero-Moreno, D. Goerlitz, V. M. Prida, and K. Nielsch

*Tuning the magnetic anisotropy of Co-Ni nanowires: comparison between single nanowires and nanowire arrays in hard-anodic aluminum oxide membranes*

Nanotechnology **23**, 465709 (2012)

S. Zastrow, J. Gooth, T. Boehnert, S. Heiderich, W. Toellner, S. Heimann, S. Schulz, and K. Nielsch  
*Thermoelectric transport and Hall measurements of low defect Sb<sub>2</sub>Te<sub>3</sub> thin films grown by atomic layer deposition*

Semiconductor Science and Technology **28**, 035010 (2013)

J. Gooth, R. Zierold, J. G. Gluschke, T. Boehnert, S. Edinger, S. Barth, and K. Nielsch

*Gate voltage induced phase transition in magnetite nanowires*

Applied Physics Letters **102**, 073112 (2013)

T. Boehnert, V. Vega, A.-K. Michel, V. M. Prida, and K. Nielsch

*Magneto-thermopower and magnetoresistance of single Co-Ni alloy nanowires*

Applied Physics Letters **103**, 092407 (2013)

S. Baessler, T. Boehnert, J. Gooth, C. Schumacher, E. Pippel, and K. Nielsch

*Thermoelectric power factor of ternary single-crystalline Sb<sub>2</sub>Te<sub>3</sub>- and Bi<sub>2</sub>Te<sub>3</sub>-based nanowires*

Nanotechnology **24**, 495402 (2013)

S. Heiderich, W. Toellner, T. Boehnert, J. G. Gluschke, S. Zastrow, C. Schumacher, E. Pippel and  
K. Nielsch

*Magnetotransport and thermopower of single Bi<sub>0.92</sub>Sb<sub>0.08</sub> nanowires*

Phys. Status Solidi RRL **7**, 898 (2013)

C. Bae, T. Boehnert, J. Gooth, S. Lim, S. Lee, H. Kim, S. Heimann, S. Schulz, H. Shin, and K. Nielsch

*Thermopower Engineering of Bi<sub>2</sub>Te<sub>3</sub> without Alloying: The interplay between nanostructuring  
and defect activation*

Semiconductor Science and Technology **29**, 064003 (2014)

X. K. Hu, P. Krzysteczko, N. Liebing, S. Serrano-Guisan, K. Rott, G. Reiss, J. Kimling, T. Böhnert, K.  
Nielsch, and H. W. Schumacher

*Magneto-thermoelectric figure of merit of Co/Cu multilayers*

Applied Physics Letters **104**, 092411 (2014)

T. Böhnert, A. C. Niemann, A.-K. Michel, S. Bäßler, J. Gooth, B. Tóth, K. Neuróhr, L. Péter, I. Ba-  
konyi, V. Vega, V. M. Prida, and K. Nielsch

*Magnetothermopower and Magnetoresistance of single Co-Ni/Cu multilayered Nanowires*

Submitted (2014)



## 8 Bibliography

- [1] M. N. Baibich *et al.*, Phys. Rev. Lett. **61**, 2472 (1988), doi: [10.1103/PhysRevLett.61.2472](https://doi.org/10.1103/PhysRevLett.61.2472).
- [2] G. Binasch, P. Gruenberg, F. Saurenbach, and W. Zinn, Phys. Rev. B **39**, 4828 (1989), doi: [10.1103/PhysRevB.39.4828](https://doi.org/10.1103/PhysRevB.39.4828).
- [3] S. Wolf, A. Y. Chtchelkanova, and D. Treger, IBM J. RES. DEV. **50**, 101 (2006), doi: [10.1147/rd.501.0101](https://doi.org/10.1147/rd.501.0101).
- [4] E. Y. Tsymbal and D. G. Pettifor, Solid State Physics **56**, 113 (2001), doi: [10.1016/S0081-1947\(01\)80019-9](https://doi.org/10.1016/S0081-1947(01)80019-9).
- [5] J. F. Gregg, I. Petej, E. Jouguelet, and C. Dennis, J. Phys. D: Appl. Phys. **35**, R121 (2002).
- [6] Y. F. Tian and S. S. Yan, Sci. China-Phys. Mech. Astron. **56**, 2 (2013), doi: [10.1007/s11433-012-4971-7](https://doi.org/10.1007/s11433-012-4971-7).
- [7] G. Reiss *et al.*, Phys. Status Solidi B **236**, 289 (2003), doi: [10.1002/pssb.200301668](https://doi.org/10.1002/pssb.200301668).
- [8] N. F. Mott and H. Jones, *The Theory of the Properties of Metals and Alloys*. (Clarendon Press, Oxford, 1936), pp. 309–314.
- [9] R. B. Roberts, Philos. Mag. B **43**, 1125 (1981), doi: [10.1080/01418638108222579](https://doi.org/10.1080/01418638108222579).
- [10] N. Cusack and P. Kendall, Proc. Phys. Soc. **72**, 898 (1958).
- [11] G. E. W. Bauer, E. Saitoh, and B. J. van Wees, Nat. Mater. **11**, 391 (2012), doi: [10.1038/NMAT3301](https://doi.org/10.1038/NMAT3301).
- [12] K. Uchida *et al.*, Nature **455**, 778 (2008), doi: [10.1038/nature07321](https://doi.org/10.1038/nature07321).
- [13] A. D. Avery, M. R. Pufall, and B. L. Zink, Phys. Rev. Lett. **109**, 196602 (2012), doi: [10.1103/PhysRevLett.109.196602](https://doi.org/10.1103/PhysRevLett.109.196602).
- [14] M. Schmid *et al.*, Phys. Rev. Lett. **111**, 187201 (2013), doi: [10.1103/PhysRevLett.111.187201](https://doi.org/10.1103/PhysRevLett.111.187201).
- [15] E. Shapira, A. Holtzman, D. Marchak, and Y. Selzer, Nano Lett. **12**, 808 (2012), doi: [10.1021/nl2038425](https://doi.org/10.1021/nl2038425).
- [16] E. Shapira, A. Tsukernik, and Y. Selzer, Nanotechnology **18**, 485703 (2007).
- [17] N. Liebing *et al.*, Phys. Rev. Lett. **107**, 177201 (2011), doi: [10.1103/PhysRevLett.107.177201](https://doi.org/10.1103/PhysRevLett.107.177201).
- [18] M. Walter *et al.*, Nature Mater. **10**, 742 (2011), doi: [10.1038/NMAT3076](https://doi.org/10.1038/NMAT3076).
- [19] F. K. Dejene, J. Flipse, and B. J. van Wees, Phys. Rev. B **86**, 024436 (2012), doi: [10.1103/PhysRevB.86.024436](https://doi.org/10.1103/PhysRevB.86.024436).
- [20] H. Yu, S. Granville, D. P. Yu, and J.-P. Ansermet, Phys. Rev. Lett. **104**, 146601 (2010), doi: [10.1103/PhysRevLett.104.146601](https://doi.org/10.1103/PhysRevLett.104.146601).

- [21] T. T. Heikkilä, M. Hatami, and G. E. W. Bauer, *Phys. Rev. B* **81**, 100408 (2010), doi: [10.1103/PhysRevB.81.100408](https://doi.org/10.1103/PhysRevB.81.100408).
- [22] T. T. Heikkilä, M. Hatami, and G. E. Bauer, *Solid State Commun.* **150**, 475 (2010), doi: [10.1016/j.ssc.2009.12.015](https://doi.org/10.1016/j.ssc.2009.12.015).
- [23] F. Völklein *et al.*, *J. Electron. Mater.* **39**, 1950 (2010), doi: [10.1007/s11664-009-1046-2](https://doi.org/10.1007/s11664-009-1046-2).
- [24] A. I. Boukai *et al.*, *Nature* **451**, 168 (2008), doi: [10.1038/nature06458](https://doi.org/10.1038/nature06458).
- [25] P. Kim, L. Shi, A. Majumdar, and P. L. McEuen, *Phys. Rev. Lett.* **87**, 215502 (2001), doi: [10.1103/PhysRevLett.87.215502](https://doi.org/10.1103/PhysRevLett.87.215502).
- [26] A. Mavrokefalos *et al.*, *J. Appl. Phys.* **105**, 104318 (2009), doi: [10.1063/1.3133145](https://doi.org/10.1063/1.3133145).
- [27] B. G. Tóth *et al.*, *Eur. Phys. J. B* **75**, 167 (2010), doi: [10.1140/epib/e2010-00132-4](https://doi.org/10.1140/epib/e2010-00132-4).
- [28] J. Smit, *Physica* **17**, 612 (1951), doi: [10.1016/0031-8914\(51\)90117-6](https://doi.org/10.1016/0031-8914(51)90117-6).
- [29] S. S. P. Parkin, Z. G. Li, and D. J. Smith, *Appl. Phys. Lett.* **58**, 2710 (1991), doi: [10.1063/1.104765](https://doi.org/10.1063/1.104765).
- [30] H. Kano *et al.*, *Appl. Phys. Lett.* **63**, 2839 (1993), doi: [10.1063/1.110791](https://doi.org/10.1063/1.110791).
- [31] L. Gravier *et al.*, *J. Magn. Magn. Mater.* **271**, 153 (2004), doi: [10.1016/j.jmmm.2003.09.022](https://doi.org/10.1016/j.jmmm.2003.09.022).
- [32] J. Shi, R. C. Yu, S. S. P. Parkin, and M. B. Salamon, *J. Appl. Phys.* **73**, 5524 (1993), doi: [10.1063/1.353690](https://doi.org/10.1063/1.353690).
- [33] D. K. C. MacDonald and W. B. Pearson, *Proc. R. Soc. London A* **241**, 257 (1957), doi: [10.1098/rspa.1957.0126](https://doi.org/10.1098/rspa.1957.0126).
- [34] J. Sakurai *et al.*, *J. Phys. Soc. Jpn.* **66**, 2240 (1997), doi: [10.1143/JPSJ.66.2240](https://doi.org/10.1143/JPSJ.66.2240).
- [35] J. Shi *et al.*, *Phys. Rev. B* **54**, 15273 (1996), doi: [10.1103/PhysRevB.54.15273](https://doi.org/10.1103/PhysRevB.54.15273).
- [36] M. J. Conover *et al.*, *J. Magn. Magn. Mater.* **102**, L5 (1991), doi: [10.1016/0304-8853\(91\)90255-9](https://doi.org/10.1016/0304-8853(91)90255-9).
- [37] H. Itoh, J. Inoue, and S. Maekawa, *Phys. Rev. B* **47**, 5809 (1993), doi: [10.1103/PhysRevB.47.5809](https://doi.org/10.1103/PhysRevB.47.5809).
- [38] A. D. Avery, M. R. Pufall, and B. L. Zink, *Phys. Rev. B* **86**, 184408 (2012), doi: [10.1103/PhysRevB.86.184408](https://doi.org/10.1103/PhysRevB.86.184408).
- [39] T. Böhnert *et al.*, *Appl. Phys. Lett.* **103**, 092407 (2013), doi: [10.1063/1.4819949](https://doi.org/10.1063/1.4819949).
- [40] M. C. Cadeville and J. Roussel, *J. Phys. F: Met. Phys.* **1**, 686 (1971).
- [41] R. P. Huebener, *Phys. Rev.* **140**, A1834 (1965), doi: [10.1103/PhysRev.140.A1834](https://doi.org/10.1103/PhysRev.140.A1834).
- [42] A. Soni and G. S. Okram, *Appl. Phys. Lett.* **95**, 013101 (2009), doi: [10.1063/1.3167302](https://doi.org/10.1063/1.3167302).
- [43] L. Berger, *Physica* **30**, 1141 (1964), doi: [10.1016/0031-8914\(64\)90105-3](https://doi.org/10.1016/0031-8914(64)90105-3).
- [44] T. R. McGuire and R. I. Potter, *IEEE Trans. Magn.* **11**, 1018 (1975), doi: [10.1109/TMAG.1975.1058782](https://doi.org/10.1109/TMAG.1975.1058782).

- [45] H. C. Van Elst, *Physica* **25**, 708 (1959), doi: [10.1016/S0031-8914\(59\)97412-9](https://doi.org/10.1016/S0031-8914(59)97412-9).
- [46] J. M. Ziman, *Electrons and Phonons: The Theory of Transport Phenomena in Solids, The international series of monographs on physics* (Oxford University Press, Incorporated, 1962).
- [47] B. Raquet *et al.*, *Phys. Rev. B* **66**, 024433 (2002), doi: [10.1103/PhysRevB.66.024433](https://doi.org/10.1103/PhysRevB.66.024433).
- [48] W. Thomson, *Proc. R. Soc. London* **8**, pp.546 (1856).
- [49] R. C. O'Handley, *Modern Magnetic Materials* (John Wiley & Sons, Inc, 2000).
- [50] N. F. Mott, *Advances in Physics* **13**, 325 (1964), doi: [10.1080/00018736400101041](https://doi.org/10.1080/00018736400101041).
- [51] A. Fert and I. A. Campbell, *Phys. Rev. Lett.* **21**, 1190 (1968), doi: [10.1103/PhysRevLett.21.1190](https://doi.org/10.1103/PhysRevLett.21.1190).
- [52] N. F. Mott, *Proc. R. Soc. London A* **153**, pp. 699 (1936).
- [53] N. F. Mott, *Proc. R. Soc. London A* **156**, 368 (1936).
- [54] W. Wernsdorfer *et al.*, *Phys. Rev. Lett.* **77**, 1873 (1996), doi: [10.1103/PhysRevLett.77.1873](https://doi.org/10.1103/PhysRevLett.77.1873).
- [55] R. Hertel and J. Kirschner, *Physica B-Condensed Matter* **343**, 206 (2004), doi: [10.1016/j.physb.2003.08.095](https://doi.org/10.1016/j.physb.2003.08.095).
- [56] T. Böhnert, *Diplom (Univ.)*, Universität Hamburg, (2009).
- [57] S. S. P. Parkin, N. More, and K. P. Roche, *Phys. Rev. Lett.* **64**, 2304 (1990), doi: [10.1103/PhysRevLett.64.2304](https://doi.org/10.1103/PhysRevLett.64.2304).
- [58] P. R. Evans, G. Yi, and W. Schwarzacher, *Appl. Phys. Lett.* **76**, 481 (2000), doi: [10.1063/1.125794](https://doi.org/10.1063/1.125794).
- [59] V. Moruzzi, J. Janak, and A. Williams, *Calculated Electronic Properties of Metals* (Elsevier Science & Technology Books, 1978).
- [60] S. K. Upadhyay, A. Palanisami, R. N. Louie, and R. A. Buhrman, *Phys. Rev. Lett.* **81**, 3247 (1998), doi: [10.1103/PhysRevLett.81.3247](https://doi.org/10.1103/PhysRevLett.81.3247).
- [61] U. Bänninger, G. Busch, M. Campagna, and H. C. Siegmann, *Phys. Rev. Lett.* **25**, 585 (1970).
- [62] R. Mitdank *et al.*, *J. Appl. Phys.* **111**, 104320 (2012), doi: [10.1063/1.4721896](https://doi.org/10.1063/1.4721896).
- [63] R. A. de Groot, F. M. Mueller, P. G. van Engen, and K. H. J. Buschow, *J. Appl. Phys.* **55**, 2151 (1984), doi: [10.1063/1.333593](https://doi.org/10.1063/1.333593).
- [64] R. Meservey and P. M. Tedrow, *Physics Reports* **238**, 173 (1994), doi: [10.1016/0370-1573\(94\)90105-8](https://doi.org/10.1016/0370-1573(94)90105-8).
- [65] B. Raquet *et al.*, *J. Appl. Phys.* **91**, 8129 (2002), doi: [10.1063/1.1456434](https://doi.org/10.1063/1.1456434).
- [66] A. P. Mihai *et al.*, *Phys. Rev. B* **77**, 060401 (2008), doi: [10.1103/PhysRevB.77.060401](https://doi.org/10.1103/PhysRevB.77.060401).

- [67] C. Kittel, *Einführung in die Festkörperphysik (Introduction to solid state physics.)* (Oldenbourg, 2005), Vol. 14.
- [68] D. MacDonald, *Thermoelectricity: An Introduction to the Principles* (John Wiley & Sons, 1962).
- [69] H. J. Goldsmid, *Introduction to Thermoelectricity* (Springer Series in Materials Science, 2009).
- [70] P. Drude, *Annalen der Physik* **306**, 566 (1900), doi: [10.1002/andp.19003060312](https://doi.org/10.1002/andp.19003060312).
- [71] J.-P. Issi, J.-P. Michenaud, and J. Heremans, *Phys. Rev. B* **14**, 5156 (1976), doi: [10.1103/PhysRevB.14.5156](https://doi.org/10.1103/PhysRevB.14.5156).
- [72] M. J. Laubitz and T. Matsumura, *Can. J. Phys.* **51**, 1247 (1973).
- [73] M. J. Laubitz, T. Matsumura, and P. J. Kelly, *Can. J. Phys.* **54**, 92 (1976).
- [74] M. J. Laubitz, *Can. J. Phys.* **45**, 3677 (1967).
- [75] F. J. Blatt, *Can. J. Phys.* **50**, 2836 (1972), doi: [10.1139/p72-377](https://doi.org/10.1139/p72-377).
- [76] L. Lorenz, *Annalen der Physik* **223**, 429 (1872), doi: [10.1002/andp.18722231107](https://doi.org/10.1002/andp.18722231107).
- [77] G. Wiedemann and R. Franz, *Annalen der Physik* **165**, 497 (1853), doi: [10.1002/andp.18531650802](https://doi.org/10.1002/andp.18531650802).
- [78] D. Rowe, *Thermoelectrics Handbook: Macro to Nano* (Taylor & Francis, 2010).
- [79] D. Narducci, *Appl. Phys. Lett.* **99**, (2011), doi: [10.1063/1.3634018](https://doi.org/10.1063/1.3634018).
- [80] G. Roy, E. Matagne, and P. J. Jacques, *J. Electron. Mater.* **42**, 1781 (2013), doi: [10.1007/s11664-012-2430-x](https://doi.org/10.1007/s11664-012-2430-x).
- [81] C. Herring, T. H. Geballe, and J. E. Kunzler, *Phys. Rev.* **111**, 36 (1958), doi: [10.1103/PhysRev.111.36](https://doi.org/10.1103/PhysRev.111.36).
- [82] L. Gurevich, *Acad. Sci. USSR. J. Phys.* **9**, 312 (1945).
- [83] F. J. Blatt, *Proc. Phys. Soc.* **83**, 1065 (1964).
- [84] A. V. Gold, D. K. C. Macdonald, W. B. Pearson, and I. M. Templeton, *Philos. Mag.* **5**, 765 (1960), doi: [10.1080/14786436008241216](https://doi.org/10.1080/14786436008241216).
- [85] J. P. Moore and R. S. Graves, *J. Appl. Phys.* **44**, 1174 (1973), doi: [10.1063/1.1662324](https://doi.org/10.1063/1.1662324).
- [86] R. F. Moreland and R. R. Bourassa, *Phys. Rev. B* **12**, 3991 (1975).
- [87] A. Matthiessen and C. Vogt, *Annalen der Physik* **198**, 19 (1864), doi: [10.1002/andp.18641980504](https://doi.org/10.1002/andp.18641980504).
- [88] L. Nordheim and C. J. Gorter, *Physica* **2**, 383 (1935), doi: [10.1016/S0031-8914\(35\)90101-X](https://doi.org/10.1016/S0031-8914(35)90101-X).
- [89] J. Shi, E. Kita, S. S. P. Parkin, and M. B. Salamon, *J. Appl. Phys.* **75**, 6455 (1994), doi: [10.1063/1.356960](https://doi.org/10.1063/1.356960).

- [90] J. Shi, S. S. P. Parkin, L. Xing, and M. B. Salamon, *J. Magn. Magn. Mater.* **125**, L251 (1993), doi: [10.1016/0304-8853\(93\)90094-l](https://doi.org/10.1016/0304-8853(93)90094-l).
- [91] L. Piraux *et al.*, *J. Magn. Magn. Mater.* **110**, L247 (1992), doi: [10.1016/0304-8853\(92\)90207-5](https://doi.org/10.1016/0304-8853(92)90207-5).
- [92] E. Y. Tsymbal, D. G. Pettifor, J. Shi, and M. B. Salamon, *Phys. Rev. B* **59**, 8371 (1999), doi: [10.1103/PhysRevB.59.8371](https://doi.org/10.1103/PhysRevB.59.8371).
- [93] H. Sato *et al.*, *J. Magn. Magn. Mater.* **152**, 109 (1996), doi: [10.1016/0304-8853\(95\)00443-2](https://doi.org/10.1016/0304-8853(95)00443-2).
- [94] J. Shi, E. Kita, L. Xing, and M. B. Salamon, *Phys. Rev. B* **48**, 16119 (1993), doi: [10.1103/PhysRevB.48.16119](https://doi.org/10.1103/PhysRevB.48.16119).
- [95] H. Sato, *Mat Sci Eng B* **31**, 101 (1995), doi: [10.1016/0921-5107\(94\)08005-4](https://doi.org/10.1016/0921-5107(94)08005-4).
- [96] M. V. Costache, G. Bridoux, I. Neumann, and S. O. Valenzuela, *Nature Mater.* **11**, 199 (2012), doi: [10.1038/nmat3201](https://doi.org/10.1038/nmat3201).
- [97] W. Heisenberg, *Z. Phys. A-Hadron Nucl.* **49**, 619 (1928).
- [98] M. Lederman, R. O'Barr, and S. Schultz, *IEEE Trans. Magn.* **31**, 3793 (1995), doi: [10.1109/20.489774](https://doi.org/10.1109/20.489774).
- [99] V. Vega *et al.*, *Nanotechnology* **23**, 465709 (2012).
- [100] K. Nielsch *et al.*, *Appl. Phys. Lett.* **79**, 1360 (2001), doi: [10.1063/1.1399006](https://doi.org/10.1063/1.1399006).
- [101] B. E. Alaca, H. Sehitoglu, and T. Saif, *Appl. Phys. Lett.* **84**, 4669 (2004), doi: [10.1063/1.1759781](https://doi.org/10.1063/1.1759781).
- [102] R. S. Wagner and W. C. Ellis, *Appl. Phys. Lett.* **4**, 89 (1964), doi: [10.1063/1.1753975](https://doi.org/10.1063/1.1753975).
- [103] K. Nielsch, F. Müller, A.-P. Li, and U. Gösele, *Adv. Mater.* **12**, 582 (2000), doi: [10.1002/\(SICI\)1521-4095\(200004\)12:8<582::AID-ADMA582>3.0.CO;2-3](https://doi.org/10.1002/(SICI)1521-4095(200004)12:8<582::AID-ADMA582>3.0.CO;2-3).
- [104] W. Lee, R. Ji, U. Goesele, and K. Nielsch, *Nature Mater.* **5**, 741 (2006), doi: [10.1038/nmat1717](https://doi.org/10.1038/nmat1717).
- [105] A. P. Li *et al.*, *J. Appl. Phys.* **84**, 6023 (1998).
- [106] J. W. Diggle, T. C. Downie, and C. W. Goulding, *Chem. Rev.* **69**, 365 (1969), doi: [10.1021/cr60259a005](https://doi.org/10.1021/cr60259a005).
- [107] K. Nielsch *et al.*, *Nano Lett.* **2**, 677 (2002), doi: [10.1021/nl025537k](https://doi.org/10.1021/nl025537k).
- [108] H. Masuda and K. Fukuda, *Science* **268**, 1466 (1995), doi: [10.1126/science.268.5216.1466](https://doi.org/10.1126/science.268.5216.1466).
- [109] K. Nielsch, Ph.D. thesis, Halle (Saale), (2002).
- [110] Y. Li, M. Zheng, L. Ma, and W. Shen, *Nanotechnology* **17**, 5101 (2006).
- [111] Y. B. Li, M. J. Zheng, and L. Ma, *Appl. Phys. Lett.* **91**, 073109 (2007), doi: [10.1063/1.2772184](https://doi.org/10.1063/1.2772184).

- [112] J. M. Montero Moreno *et al.*, *Advanced Functional Materials* n/a (2013), doi: [10.1002/adfm.201303268](https://doi.org/10.1002/adfm.201303268).
- [113] R. Zierold *et al.*, *Adv. Funct. Mater.* **21**, 226 (2011), doi: [10.1002/adfm.201001395](https://doi.org/10.1002/adfm.201001395).
- [114] M. S. Sander *et al.*, *Adv. Mater.* **16**, 2052 (2004), doi: [10.1002/adma.200400446](https://doi.org/10.1002/adma.200400446).
- [115] V. Miikkulainen, M. Leskelä, M. Ritala, and R. L. Puurunen, *J. Appl. Phys.* **113**, (2013), doi: [10.1063/1.4757907](https://doi.org/10.1063/1.4757907).
- [116] R. L. Puurunen, *J. Appl. Phys.* **97**, (2005), doi: [10.1063/1.1940727](https://doi.org/10.1063/1.1940727).
- [117] J. Bachmann *et al.*, *Angew. Chem.-Int. Edit.* **47**, 6177 (2008), doi: [10.1002/anie.200800245](https://doi.org/10.1002/anie.200800245).
- [118] D. Navas *et al.*, *Appl. Phys. Lett.* **90**, 192501 (2007), doi: [10.1063/1.2737373](https://doi.org/10.1063/1.2737373).
- [119] G. Wilcox, *Milan Paunovic and Mordechai Schlesinger, Fundamentals of Electrochemical Deposition*. (Kluwer Academic Publishers, 1999), No. 9, pp. 1139–1140, doi: [10.1023/A:1003796312932](https://doi.org/10.1023/A:1003796312932).
- [120] A. J. Bard, R. Parsons, and J. Jordan, in *Standard Potentials in Aqueous Solutions*, edited by M. Dekker (IUPAC, 1985).
- [121] K. Oldham and J. Myland, *Fundamentals of Electrochemical Science* (Elsevier Science, 1993).
- [122] E. Gomez, J. Ramirez, and E. Valles, *J. Appl. Electrochem.* **28**, 71 (1998), doi: [10.1023/A:1003201919054](https://doi.org/10.1023/A:1003201919054).
- [123] C. Fan and D. L. Piron, *Electrochim. Acta* **41**, 1713 (1996), doi: [10.1016/0013-4686\(95\)00488-2](https://doi.org/10.1016/0013-4686(95)00488-2).
- [124] C. A. Ross, *Annu. Rev. Mater. Sci.* **24**, 159 (1994).
- [125] W. Schwarzacher *et al.*, *J. Magn. Magn. Mater.* **165**, 23 (1997), symposium E: Magnetic Ultrathin Films, Multilayers and Surfaces, doi: [10.1016/S0304-8853\(96\)00465-9](https://doi.org/10.1016/S0304-8853(96)00465-9).
- [126] K. Liu, K. Nagodawithana, P. C. Searson, and C. L. Chien, *Phys. Rev. B* **51**, 7381 (1995).
- [127] B. Voegeli, A. Blondel, B. Doudin, and J.-P. Ansermet, *J. Magn. Magn. Mater.* **151**, 388 (1995), doi: [10.1016/0304-8853\(95\)00511-0](https://doi.org/10.1016/0304-8853(95)00511-0).
- [128] I. Bakonyi and L. Peter, *Prog. Mater. Sci.* **55**, 107 (2010), doi: [10.1016/j.pmatsci.2009.07.001](https://doi.org/10.1016/j.pmatsci.2009.07.001).
- [129] B. Lie, Diploma, Universität Hamburg, (2010).
- [130] M. Alper, W. Schwarzacher, and S. J. Lane, *J. Electrochem. Soc.* **144**, 2346 (1997).
- [131] V. Weihnacht *et al.*, *J. Electrochem. Soc.* **150**, C507 (2003), doi: [10.1149/1.1583716](https://doi.org/10.1149/1.1583716).
- [132] M. Alper *et al.*, *J. Appl. Electrochem.* **34**, 841 (2004), doi: [10.1023/B:JACH.0000035608.49948.e8](https://doi.org/10.1023/B:JACH.0000035608.49948.e8).

- [133] M. Safak, M. Alper, and H. Kockar, *J. Nanosci. Nanotechnol.* **8**, 854 (2008), doi: [10.1166/jnn.2008.B242](https://doi.org/10.1166/jnn.2008.B242).
- [134] G. Nabiyouni, W. Schwarzacher, Z. Rolik, and I. Bakonyi, *J. Magn. Magn. Mater* **253**, 77 (2002).
- [135] B. G. Tóth *et al.*, *Electrochim. Acta* **91**, 122 (2013), doi: [10.1016/j.electacta.2012.12.033](https://doi.org/10.1016/j.electacta.2012.12.033).
- [136] S. K. J. Lenczowski, C. Schönenberger, M. A. M. Gijs, and W. J. M. de Jonge, *J. Magn. Magn. Mater.* **148**, 455 (1995), doi: [10.1016/0304-8853\(95\)00109-3](https://doi.org/10.1016/0304-8853(95)00109-3).
- [137] Q. X. Liu *et al.*, *J. Magn. Magn. Mater.* **280**, 60 (2004), doi: [10.1016/j.immm.2004.02.031](https://doi.org/10.1016/j.immm.2004.02.031).
- [138] W. Schwarzacher and D. S. Lashmore, *IEEE Trans. Magn.* **32**, 3133 (1996), doi: [10.1109/20.508379](https://doi.org/10.1109/20.508379).
- [139] Z. Wang *et al.*, *IEEE-NEMS 2013* 738 (2013), doi: [10.1109/NEMS.2013.6559834](https://doi.org/10.1109/NEMS.2013.6559834).
- [140] J. Gooth, Master's Thesis, Lund University, (2011).
- [141] A.-K. Michel, Master's Thesis, Universität Hamburg, (2012).
- [142] J. G. Gluschke, Bachelor's Thesis, Universität Hamburg, (2011).
- [143] N. Peranio *et al.*, *Adv. Funct. Mater.* **22**, 151 (2012), doi: [10.1002/adfm.201101273](https://doi.org/10.1002/adfm.201101273).
- [144] S. Bäßler *et al.*, *Nanotechnology* **24**, 495402 (2013).
- [145] S. Heiderich *et al.*, *Phys. Status Solidi RRL* **7**, 898 (2013), doi: [10.1002/pssr.201308004](https://doi.org/10.1002/pssr.201308004).
- [146] J. Gooth *et al.*, *Appl. Phys. Lett.* **102**, 073112 (2013), doi: [10.1063/1.4793529](https://doi.org/10.1063/1.4793529).
- [147] J. Gooth *et al.*, *Relaxation of the Trimeton Lattice in Magnetite*, (2014) (unpublished).
- [148] S. Zastrow *et al.*, *Semicond. Sci. Technol.* **28**, 035010 (2013), doi: [10.1088/0268-1242/28/3/035010](https://doi.org/10.1088/0268-1242/28/3/035010).
- [149] C. Bae *et al.*, *Semicond. Sci. Technol.* **29**, 064003 (2014).
- [150] A. Kobs *et al.*, *Phys. Rev. Lett.* **106**, 217207 (2011), doi: [10.1103/PhysRevLett.106.217207](https://doi.org/10.1103/PhysRevLett.106.217207).
- [151] A. Kobs, S. Heße, H. P. Oepen, and P. Weinberger, *Philos. Mag.* **92**, 2835 (2012), doi: [10.1080/14786435.2012.676213](https://doi.org/10.1080/14786435.2012.676213).
- [152] L. Lu, W. Yi, and D. L. Zhang, *Rev. Sci. Instrum.* **72**, 2996 (2001), doi: [10.1063/1.1378340](https://doi.org/10.1063/1.1378340).
- [153] J. Maxwell and W. Niven, *A Treatise on Electricity and Magnetism: pt. III. Magnetism. pt. IV. Electromagnetism, A Treatise on Electricity and Magnetism* (At the Clarendon Press, 1881).
- [154] A. v. Ettingshausen and W. Nernst, *Annalen der Physik* **265**, 343 (1886), doi: [10.1002/andp.18862651010](https://doi.org/10.1002/andp.18862651010).
- [155] R. Lueck and T. Ricker, *Phys. Status Solidi B* **7**, 817 (1964), doi: [10.1002/pssb.19640070310](https://doi.org/10.1002/pssb.19640070310).
- [156] A. D. Avery *et al.*, *Phys. Rev. B* **83**, 100401 (2011), doi: [10.1103/PhysRevB.83.100401](https://doi.org/10.1103/PhysRevB.83.100401).

- [157] A. Fert and I. A. Campbell, *J. Phys. F: Met. Phys.* **6**, 849 (1976).
- [158] R. Ferre *et al.*, *Phys. Rev. B* **56**, 14066 (1997), doi: [10.1103/PhysRevB.56.14066](https://doi.org/10.1103/PhysRevB.56.14066).
- [159] J.-E. Wegrowe *et al.*, *Phys. Rev. B* **73**, 134422 (2006), doi: [10.1103/PhysRevB.73.134422](https://doi.org/10.1103/PhysRevB.73.134422).
- [160] Y. Rheem, B.-Y. Yoo, W. P. Beyermann, and N. V. Myung, *Nanotechnology* **18**, 015202 (2007).
- [161] J. Barandiaran *et al.*, *Magnetics*, *IEEE Transactions on* **25**, 3330 (1989), doi: [10.1109/20.42293](https://doi.org/10.1109/20.42293).
- [162] J. De La Torre Medina, M. Darques, L. Piraux, and A. Encinas, *J. Appl. Phys.* **105**, (2009), doi: [10.1063/1.3067773](https://doi.org/10.1063/1.3067773).
- [163] J. Kimling *et al.*, *Phys. Rev. B* **84**, 174406 (2011), doi: [10.1103/PhysRevB.84.174406](https://doi.org/10.1103/PhysRevB.84.174406).
- [164] H. Forster *et al.*, *IEEE Trans. Magn.* **38**, 2580 (2002), doi: [10.1109/TMAG.2002.801958](https://doi.org/10.1109/TMAG.2002.801958).
- [165] T. Maeda and T. Somura, *J. Phys. Soc. Jpn.* **44**, 148 (1978), doi: [10.1143/JPSJ.44.148](https://doi.org/10.1143/JPSJ.44.148).
- [166] N. Data, *Functional Relationships in Science and Technology*, edited by KH Hellwege and JL Olsen, *Landolt-Börnstein, New Series, Group III, Vol. 15, Pt. b* (Springer, Berlin, 1985).
- [167] F. J. Blatt *et al.*, *Phys. Rev. Lett.* **18**, 395 (1967), doi: [10.1103/PhysRevLett.18.395](https://doi.org/10.1103/PhysRevLett.18.395).
- [168] B. L. Zink *et al.*, *Solid State Commun.* **150**, 514 (2010), doi: [10.1016/j.ssc.2009.11.003](https://doi.org/10.1016/j.ssc.2009.11.003).
- [169] L. Gravier, S. Serrano-Guisan, F. Reuse, and J.-P. Ansermet, *Phys. Rev. B* **73**, 52410 (2006).
- [170] S. Serrano-Guisan, L. Gravier, M. Abid, and J.-P. Ansermet, *J. Appl. Phys.* **99**, 08T108 (2006), doi: [10.1063/1.2176594](https://doi.org/10.1063/1.2176594).
- [171] L. Gravier *et al.*, *IEEE Trans. Magn.* **38**, 2700 (2002), doi: [10.1109/TMAG.2002.803151](https://doi.org/10.1109/TMAG.2002.803151).
- [172] L. Gravier, S. Serrano-Guisan, and J.-P. Ansermet, *J. Appl. Phys.* **97**, 10C501 (2005), doi: [10.1063/1.1846593](https://doi.org/10.1063/1.1846593).
- [173] L. Gravier, S. Serrano-Guisan, F. Reuse, and J.-P. Ansermet, *Phys. Rev. B* **73**, 024419 (2006), doi: [10.1103/PhysRevB.73.024419](https://doi.org/10.1103/PhysRevB.73.024419).
- [174] J. W. Bos *et al.*, *Phys. Rev. B* **75**, 195203 (2007), doi: [10.1103/PhysRevB.75.195203](https://doi.org/10.1103/PhysRevB.75.195203).
- [175] B. Hamdou *et al.*, *Adv. Mater.* **25**, 239 (2013), doi: [10.1002/adma.201202474](https://doi.org/10.1002/adma.201202474).
- [176] Y. Lan, A. J. Minnich, G. Chen, and Z. Ren, *Adv. Funct. Mater.* **20**, 357 (2010), doi: [10.1002/adfm.200901512](https://doi.org/10.1002/adfm.200901512).
- [177] V. D. Nguyen *et al.*, *Phys. Rev. Lett.* **107**, 136605 (2011), doi: [10.1103/PhysRevLett.107.136605](https://doi.org/10.1103/PhysRevLett.107.136605).
- [178] J. F. Gregg *et al.*, *Phys. Rev. Lett.* **77**, 1580 (1996), doi: [10.1103/PhysRevLett.77.1580](https://doi.org/10.1103/PhysRevLett.77.1580).
- [179] M. S. Salem *et al.*, *J. Mater. Chem.* **22**, 8549 (2012), doi: [10.1039/C2JM16339J](https://doi.org/10.1039/C2JM16339J).
- [180] S. D. Leith, S. Ramli, and D. T. Schwartz, *J. Electrochem. Soc.* **146**, 1431 (1999), doi: [10.1149/1.1391781](https://doi.org/10.1149/1.1391781).

- [181] X.-T. Tang, G.-C. Wang, and M. Shima, *Phys. Rev. B* **75**, 134404 (2007), doi: [10.1103/PhysRevB.75.134404](https://doi.org/10.1103/PhysRevB.75.134404).
- [182] K. Attenborough *et al.*, *MRS Proceedings* **384**, (1995), doi: [10.1557/PROC-384-3](https://doi.org/10.1557/PROC-384-3).
- [183] F. Nasirpouri *et al.*, *J. Magn. Magn. Mater.* **308**, 35 (2007), doi: [10.1016/j.jmmm.2006.04.035](https://doi.org/10.1016/j.jmmm.2006.04.035).
- [184] X. Huang, L. Tan, H. Cho, and B. J. H. Stadler, *J. Appl. Phys.* **105**, 07D128 (2009), doi: [10.1063/1.3075990](https://doi.org/10.1063/1.3075990).
- [185] L. Piraux *et al.*, *Appl. Phys. Lett.* **65**, 2484 (1994), doi: [10.1063/1.112672](https://doi.org/10.1063/1.112672).
- [186] A. Blondel, J. P. Meier, B. Doudin, and J.-P. Ansermet, *Appl. Phys. Lett.* **65**, 3019 (1994), doi: [10.1063/1.112495](https://doi.org/10.1063/1.112495).
- [187] A. Fert and L. Piraux, *J. Magn. Magn. Mater.* **200**, 338 (1999), doi: [10.1016/S0304-8853\(99\)00375-3](https://doi.org/10.1016/S0304-8853(99)00375-3).
- [188] K. Nishimura *et al.*, *J. Phys. Soc. Jpn.* **63**, 2685 (1994), doi: [10.1143/JPSJ.63.2685](https://doi.org/10.1143/JPSJ.63.2685).
- [189] I. Bakonyi *et al.*, *J. Electrochem. Soc.* **149**, C195 (2002), doi: [10.1149/1.1453409](https://doi.org/10.1149/1.1453409).
- [190] I. Bakonyi *et al.*, *Phys. Rev. B* **79**, 174421 (2009), doi: [10.1103/PhysRevB.79.174421](https://doi.org/10.1103/PhysRevB.79.174421).
- [191] B. Doudin, A. Blondel, and J.-P. Ansermet, *J. Appl. Phys.* **79**, 6090 (1996), doi: <http://dx.doi.org/10.1063/1.362100>.
- [192] Q.-X. Liu, L. Péter, J. Pádár, and I. Bakonyi, *J. Electrochem. Soc.* **152**, C316 (2005), doi: [10.1149/1.1882092](https://doi.org/10.1149/1.1882092).
- [193] S. A. Baily, M. B. Salamon, and W. Oepts, *J. Appl. Phys.* **87**, 4855 (2000), doi: [10.1063/1.373181](https://doi.org/10.1063/1.373181).
- [194] Y. Kobayashi *et al.*, *J. Phys. Soc. Jpn.* **65**, 1910 (1996), doi: [10.1143/JPSJ.65.1910](https://doi.org/10.1143/JPSJ.65.1910).
- [195] L. Gravier *et al.*, *Meas. Sci. Technol.* **15**, 420 (2004).
- [196] D. K. C. MacDonald, W. B. Pearson, and I. M. Templeton, *Proc. R. Soc. London A* **266**, 161 (1962), doi: [10.1098/rspa.1962.0054](https://doi.org/10.1098/rspa.1962.0054).
- [197] R. B. Roberts, *Philos. Mag.* **36**, 91 (1977), doi: [10.1080/00318087708244450](https://doi.org/10.1080/00318087708244450).
- [198] R. B. Roberts, F. Righini, and R. C. Compton, *Philos. Mag. B* **52**, 1147 (1985), doi: [10.1080/13642818508238957](https://doi.org/10.1080/13642818508238957).
- [199] T. Farrell and D. Greig, *J. Phys. C: Solid State Phys.* **3**, 138 (1970).
- [200] K. Pekala and M. Pekala, *Nanostruct. Mater.* **6**, 819 (1995), proceedings of the Second International Conference on Nanostructured Materials, doi: [10.1016/0965-9773\(95\)00185-9](https://doi.org/10.1016/0965-9773(95)00185-9).
- [201] H. W. Worner, *AuSRA* **4**, 62 (1951).
- [202] W. Haynes and D. Lide, *CRC Handbook of Chemistry and Physics: A Ready-reference Book of Chemical and Physical Data* (CRC Press, 2011).

- [203] G. W. Scovil, J. Appl. Phys. **27**, 1196 (1956), doi: [10.1063/1.1722230](https://doi.org/10.1063/1.1722230).
- [204] V. Popescu and P. Kratzer, Phys. Rev. B **88**, 104425 (2013), doi: [10.1103/PhysRevB.88.104425](https://doi.org/10.1103/PhysRevB.88.104425).
- [205] E. H. Sondheimer, Can. J. Phys. **34**, 1246 (1956), doi: [10.1139/p56-138](https://doi.org/10.1139/p56-138).
- [206] V. Vega, Ph.D. thesis, Universidad de Oviedo, (2012).

Eine Wissenschaftliche Arbeit ist selten ohne Hilfe denkbar, deshalb möchte ich mich bei allen bedanken ohne die diese Arbeit nicht entstanden wäre:

**Prof. Dr. Nielsch** für die Betreuung , die sehr guten Forschungsbedingungen und die Begutachtung.

**Prof. Dr. Oepen und Prof. Dr. Thomas** für die Begutachtung.

**Prof. Dr. Daniela Pfannkuche** für den Vorsitz des Prüfungsausschuss.

**Prof. Dr. Bachmann, Dr. Detlef Görlitz und Dr. Josep M. Montero Moreno** für die wissenschaftlichen Diskussionen und die Hilfe im Chemie Labor.

**Reinhold Meißner und den Mitglieder der E-Werkstatt** für die technische Unterstützung.

**Iris Klüver und Stephanie Baer** für die organisatorische Unterstützung.

**Robert, William, Ole, Stephan, und Judith** für die Zusammenarbeit zu Beginn meiner Arbeit.

**Johannes Gooth, Johannes Kimling, Bael, Philip, Sebastian, Andre, Axel und der Gruppe G.** für die Zusammenarbeit während der letzten Jahre.

**Martin, Vincent, Sonja, Christian, Sven, Hosun, Mathias, Heiko** und ganz besonders dem besten Tischnachbarn **Lewis**.

Besonders hervorheben möchte ich die an dieser Arbeit beteiligten Studenten:

**Bastian Lee, Jan Gluschke, Svenja, Ann-Kathrin und Anna.**

und Kollaborationspartner:

**Der Gruppe von Dr. László Péter und Prof. Imre Bakonyi** aus Budapest.

**Victor Vega und Victor Prida** aus Oviedo.

Meinen **Freunden** und meiner **Familie**.